THE UNIVERSITY OF CHICAGO

CONSTRUCTION AND IMPACT OF THE HIGH ENERGY LIGHT ISOTOPE
EXPERIMENT'S RING IMAGING CHERENKOV DETECTOR

A DISSERTATION SUBMITTED TO
THE FACULTY OF THE DIVISION OF THE PHYSICAL SCIENCES
IN CANDIDACY FOR THE DEGREE OF
DOCTOR OF PHILOSOPHY

DEPARTMENT OF PHYSICS

BY
LUCAS BEAUFORE

CHICAGO, ILLINOIS
AUGUST 2023

To the many people who listened to me talk incessantly about this project for the last six years. Here's a quick summary.

"We are stuck with technology when what we really want is just stuff that works."

- Douglas Adams

TABLE OF CONTENTS

LIST OF FIGURES

ACKNOWLEDGMENTS

I have had so much support over the course of this PhD, I hardly know if I can adequately express a fraction of my thanks. I'll attempt a first order approximation below:

I would first like to thank my advisor, Prof. Scott Wakely, for six years of support, insight, guidance, and good humor. I am incredibly grateful to have had the opportunity to learn from someone with an understanding of building scientific instrumentation that is both broad *and* detail oriented. Thank you to my Wakely-lab coworkers (past and present) Hyebin Jeon, Rostom Mbarek, Kenichi Sakai, Ian Wisher, and thank you as well as the many undergraduate researchers over the past six years who did much of the needed work to make HELIX a success. Thank you to all the engineers and technicians who brought so much skill and experience to making this payload. Thank you as well to all my collaborators on the HELIX experiment, for working long and hard to get this thing ready to fly. In particular, I'd like thank the collaborators we lost over the course of this project - Prof. Dietrich Müller, Brandon Kunkler, and Mike Lang. I would like to specially highlight Keith McBride, whose input and support were critical to making large parts of this thesis possible, and whose advice and good cheer were always helpful and appreciated.

Thank you to the people of UChicago physics and astronomy for their support, and the many people who have and continue to work hard to make their department communities accepting and supporting. Thank you as well to the OSU physics community for teaching me that I wanted to be a physicist and giving me the skills succeed in graduate school - I'm excited to be coming back! Thank you to Greg King and Troy Dramble, my high school robotics coaches, who taught me technical and problem solving skills I still use in my research to this day. Thank you to the Illinois Space Grant Consortium for their support and funding.

Thank you to the many, many, many friends whose kindness, companionship and support were invaluable over these last six years as it has been my entire life. I am intimidated by the task of listing them all here for fear of forgetting someone. I will say a broad thank you to my

UChicago 2017 physics cohort for a truly unbelievable number of social activities that kept me sane (Pub trivia, brunches, pub trivia, D&D, pub trivia, PSD happy hour, pub trivia, skating, etc...). Thank you in particular to Dan, Tracy, Louis, Liza, and Michael for D&D nights, and to Nina for Star Wars nights during the hardest weeks of this project. Thank you to my friends from childhood through undergrad through grad school who all formed one giant group chat embarrassingly named "squad" whose origins I no longer remember and who are some of the most intelligent, kind, and strange people I've had the great fortune to know. Special thanks to Garrett, Olivia, and Kevin, whose Monday game nights kept me connected to home.

Thank you to my entire family for their love and support. Thank you to my Mom and Dad for giving me unending support in so many facets of my life, and for being both "responsible parents" and "cool parents" simultaneously. I'm only a physicist because you spent my whole life encouraging my interests and making my many quirks into something positive, and for that I'm forever grateful. Thank you to my sister Jane for being the funniest person I know, and for being the cool sibling I can talk about at parties. Thank you Jen, Richard, Sean, Cara, and Marley for welcoming me into their wonderful family and including me from the get-go (and for Richard's hugely helpful feedback on my defense presentation)! Thank you to my cats, Westley and Leia: I'm not sure what they did to help, but they sure did it with a lot of personality.

Above all, thank you my wife Kaeli Hughes, who has more of my love and thanks than can fit into this thesis, let alone these acknowledgments. She is truly the most intelligent, clever, kind, and entertaining person I have ever met, and I cannot wait to see all the amazing physics she contributes to in her career. Her help, insight, love, and support were absolutely essential to my success in graduate school: she said she'd save the Dr. Beaufore title for me in her thesis acknowledgments, and here we are! Now that I'm done, hopefully we'll have more time to finish watching Star Trek.

ABSTRACT

Understanding the propagation processes of cosmic rays is critical to interpreting features in the cosmic-ray spectrum. HELIX (High Energy Light Isotope eXperiment) seeks to improve this understanding by measuring the chemical and isotopic abundances of light cosmic ray nuclei. HELIX is optimized to measure the abundances of the propagation clock isotope ^{10}Be and stable isotope ^{9}Be at energies between 0.2 and 3 GeV/n, an essential dataset for understanding the propagation history of cosmic rays. In addition, HELIX will measure the fluxes of all the light isotopes between protons (Z=1) and neon (Z=10). The HELIX instrument is a magnet spectrometer, designed to fly on a long duration balloon, and consists of a 1 Tesla superconducting magnet with a high-resolution drift-chamber tracker for measuring the particle rigidity, a time of flight detector for measuring charge and velocities at lower energies, and a ring-imaging Cherenkov detector (RICH) for measuring particle velocities at higher energies. Although containing contributions to many elements of HELIX's payload, the majority of this thesis project concerns the design, construction, and calibration of HELIX's RICH detector.

This thesis will first give a scientific background on the basics of cosmic ray physics. It will then present an analysis demonstrating how HELIX's scientific goals motivate the development of the RICH detector and how its proper design and calibration affect the final results. Next, this thesis will discuss the properties of silicon photomultipliers (SiPMs), which are used to create the RICH detector's focal plane, as well as the work done to characterize and calibrate those selected for use in HELIX. This thesis will also discuss the development, debugging, and integration of the front end electronics used in the RICH's focal plane. Finally, it will outline the construction, installation into the payload, and in-place calibration of the full RICH detector.

CHAPTER 1
COSMIC RAY BASICS

Earth exists in a constant rain of charged particles, approaching from all directions. These nuclei and elementary particles, called cosmic rays, come to us from sources both within and beyond our galaxy. Importantly, they are the only directly measurable matter to reach our planet from beyond our solar system. The observed energy range of cosmic rays arriving from outside our solar system extends from below 1 GeV to beyond 10^{11} GeV, and contains all stable nuclei and charged particles with a lifetime longer than 10^6 years. (Workman and Others [2022], Bird et al. [1995]). Upon reaching Earth this radiation collides with the top of our atmosphere, interacting with the gasses present there and creating new "secondary" cosmic rays comprised of elementary particles (note that later we will use the term "secondary cosmic rays" in a different, non-atmospheric context). These atmospheric secondary cosmic rays can travel down through the atmosphere - some reach Earth's surface and even penetrate underground.

1.1   All-Particle Cosmic Ray Spectrum

The energy spectrum of cosmic rays approximately follows a steeply falling power law with an index that takes on various values, depending on the energy regime. This can be seen, for example, in the all particle cosmic ray spectrum shown in Figure 1.1. Transitions between the power law indices can be seen as features in this all particle spectrum, labeled in Figure 1.1 as the *knee*, the *second knee*, and the *ankle*.

The *knee* is the steepening of the spectrum from an index of $\gamma \approx -2.7$ to $\gamma \approx -3.1$ ($dN/dE \propto E^{\gamma}$) which occurs between 10^{15} and 10^{16} eV. Theoretical models for the origin of the *knee* include limits in the ability of galactic accelerators to accelerate protons to higher energies and the effects of propagation and confinement of cosmic rays, both of which have a
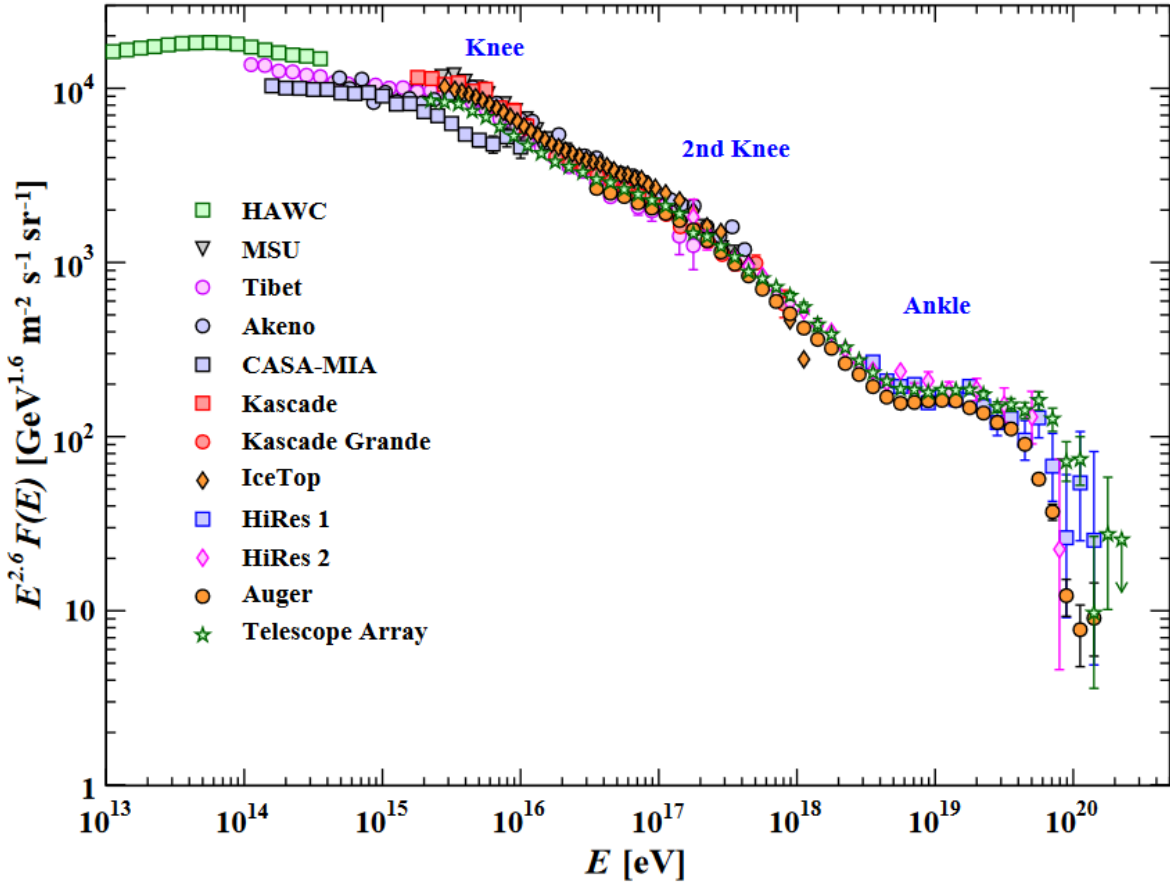
Figure 1.1: The all-particle spectrum of cosmic rays as a function of E (energy-per-nucleus), as detected from air shower measurements. Note that the spectrum has been multiplied by a factor of $E^{2.6}$ to better display features within the spectrum. Source: Workman and Others [2022]

linear dependence on the charge Z of the nucleus (Hörandel [2004], Ptuskin et al. [1993]). A second steepening of the spectrum occurs around 10^{17}, referred to as the *second knee*. The *second knee*'s origin could be similar to that of the first knee, now with iron and other heavy nuclei steepening rather than protons. This would be consistent with a rigidity dependent acceleration mechanism for galactic cosmic rays, in which the primary elements comprising the spectrum each steepen at the same rigidity, known as a *Peters cycle* (Workman and Others [2022], Peters [1961]). This is supported by measurements by the Kascade-Grande experiment, who report evidence of bending in the all particle spectrum in the region of the

2

second knee due to a decrease in flux of the heavy component, and by IceCube and IceTop, who report that the mean logarithmic mass of the cosmic ray spectra is increasing between the *knee* and *second knee* (Apel et al. [2013], Aartsen et al. [2019]).

As the energy of the spectrum increases above the *second knee*, the mean logarithmic mass decreases (Kampert and Unger [2012]) until the energy reaches about $10^{18.5}$ eV. At this energy is the final labeled feature in Figure 1.1, the *ankle*. The *ankle* is a flattening of the all particle spectrum occurring around $10^{18.5}$ eV, whose origin has no one accepted explanation. Possible origins include (but are not limited to) extragalactic flux beginning to dominate in this region (Bird et al. [1994]), ultra-high-energy proton interactions with the CMB (Berezinsky et al. [2006]), and photo-disintegration of ultrahigh energy nuclei in the region around the the accelerator(Unger et al. [2015]).

Above the region of the *ankle*, beginning around 5×10^{19} eV, the spectrum steeply declines. The GZK effect for extragalactic cosmic rays, where ultrahigh energy cosmic rays interact with the cosmic ray background, predicts a cutoff at this energy (Greisen [1966], Zatsepin and Kuz'min [1966]).

1.2   Cosmic Ray Acceleration

In 1949, Enrico Fermi proposed an acceleration mechanism for cosmic rays, in which they are primarily accelerated via collisions with moving magnetic fields in the interstellar space. (Fermi [1949]). The randomly moving magnetic structures produce "magnetic mirrors" which reflect the particles, with tail on collisions reducing the particle's energy and head on collisions adding to it (to use a rough analogy, like the head-on collision of hitting a baseball). Head on collisions are more likely, and so on average the particles gain energy $\Delta E / E \propto (V/c)^2$, where V is the velocity of the magnetic fields. This is known as the Fermi II mechanism, due to the energy gain being proportional to the *square* of the velocity. However, this mechanism is not enough for a complete understanding. One drawback is that
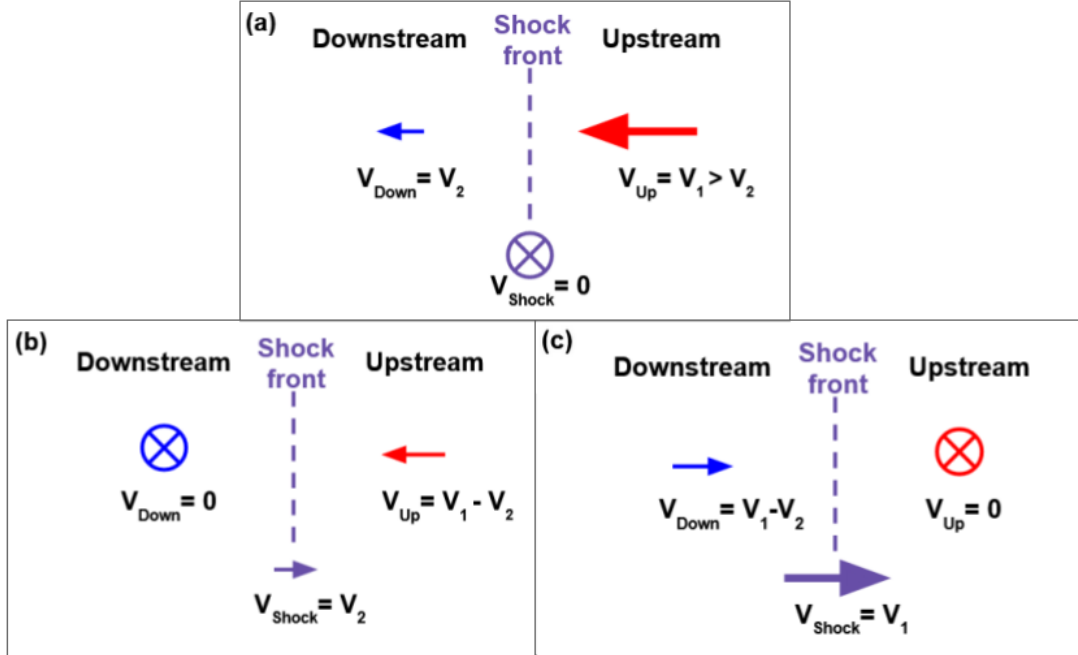
Figure 1.2: A simplified cartoon of Diffusive Shock Acceleration (DSA). (a) The velocities in the rest frame of the shock front. (b) The velocities in the rest frame of the downstream (post-shock) medium. (c) The velocities in the rest frame of the upstream (pre-shock) medium. Notice that in either of the medium's rest frames, a particle passing across the shock front to the other medium will meet the other medium's velocity head-on.

despite predicting a power law relationship to energy, it does not predict a uniform value for the index, as is observed. Instead, the value of the exponent is dependent on both the rate of energy gain and on the escape time of the particle from the acceleration region. Additionally, the low density of the magnetic fields, and a value of V such that $V << c$, result in a very slow energy gain (Bustamante et al. [2010]).

In the 1970s, a similar acceleration mechanism in the case of shocks was proposed (Bell [1978]). Shock waves occur when a disturbance in a medium propagates faster than the local speed of sound. This creates a traveling "shock front" over which physical conditions in the medium are (essentially) discontinuous. Of particular relevance here is the velocity discontinuity across the shock front, from which arises a scenario where a particle crossing the shock front in either direction sees its collision with the magnetic material on the other

4

side as "head on". As such, a crossing particle will always gain energy, regardless of the direction of crossing. This velocity discontinuity is illustrated in Figure 1.2. If both sides of the shock front contain strong, turbulent magnetic fields that confine the particle close to the shock, the particle will continue to gain energy as it travels back and forth over the shock front. The resulting energy gain is therefore larger than in Fermi II acceleration and will be linear with velocity, $\Delta E/E \propto (V/c)$. Additionally, the resulting spectrum now has a uniform power law index. This mechanism is called Diffusive Shock Acceleration (DSA), or Fermi I acceleration due to its linear nature. A helpful primer can be found in Bustamante et al. [2010], and a discussion of the requirements of the magnetic fields in the vicinity of the shock can be found in Amato [2014].
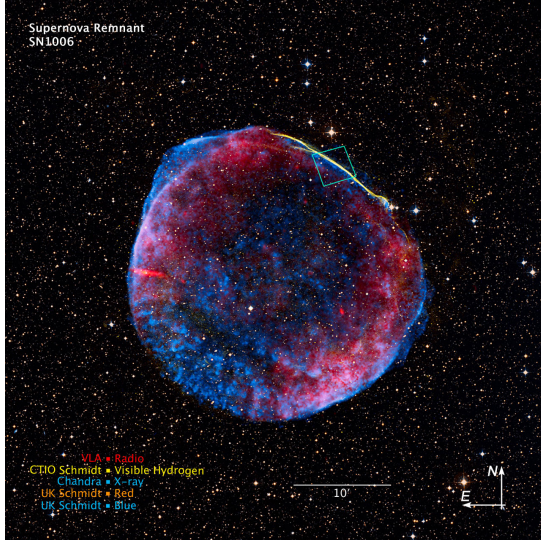
(a) Supernova SN 1006, composite radio, visible light, and x-ray data. The teal box on top right shows location of image (b).
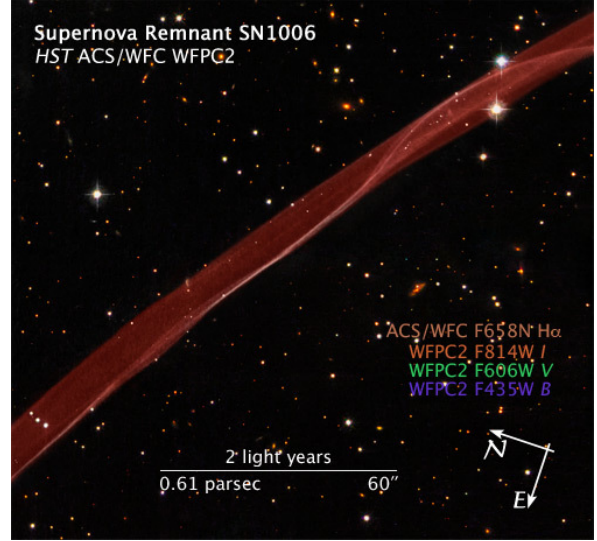
(b) The supernova remnant's blast wave, sweeping through surrounding gas. Image taken by the Hubble Space Telescope.

Figure 1.3: Supernova remnants are widely accepted as sources for galactic cosmic rays. Image credit for (a): NASA, ESA, and Z. Levay (STScI). Science Credit: Radio: NRAO/AUI/NSF GBT+VLA 1.4 GHz mosaic (Dyer, Maddalena and Cornwell, NRAO); X-ray: NASA/CXC/Rutgers/G. Cassam-Chenai and J. Hughes et al.; Optical: F.Winkler/Middlebury College and NOAO/AURA/NSF; and DSS. https://cdn.spacetelescope.org/archives/images/large/opo0822b.jpg Image credit for (b): NASA, ESA, and the Hubble Heritage Team (STScI/AURA); Acknowledgment: W. Blair (Johns Hopkins University). https://stsci-opo.org/STScI-01EVVDWRMH7PMBG8R8367Y4CA5.jpg

1.3 Cosmic Ray Sources

Two classes of cosmic ray sources were alluded to when discussing the all-particle cosmic ray spectrum: lower energy galactic cosmic rays originating from within the Milky Way and which populate the spectrum up to the *second knee*, and higher energy extragalactic cosmic rays that can be found in and beyond the *ankle*.

Sources of galactic cosmic rays below 10^{17} eV are thought to be particles accelerated in supernova remnants (SNRs) via diffusive shock acceleration. The resulting charged particles have a power-law momentum spectrum, compatible with cosmic ray observations (Bell [1978], Amato [2014]). Given the rate and energy of supernovae in the Milky Way, we can estimate

a conversion of $\sim$ 5-10% supernova energy could account for what is observed (Blasi [2013]).

Cosmic rays with energy above 10^{18} eV are believed to originate outside our galaxy. Beyond that, however, their sources are far less well agreed upon than galactic cosmic rays. Some reviews of possible Ultra High Energy Cosmic Ray (UHECR) sources can be found in Blandford et al. [2014], Kotera and Olinto [2011] and Letessier-Selvon and Stanev [2011]. Proposed extragalactic sources include, but are hardly limited to, Active Galactic Nuclei (AGN)(Berezhko [2008], γ-Ray Bursts (GRB)(Vietri [1995], Waxman [1995]), and newly born pulsars (Fang et al. [2012]).

1.4 Galactic Cosmic Ray Nuclei
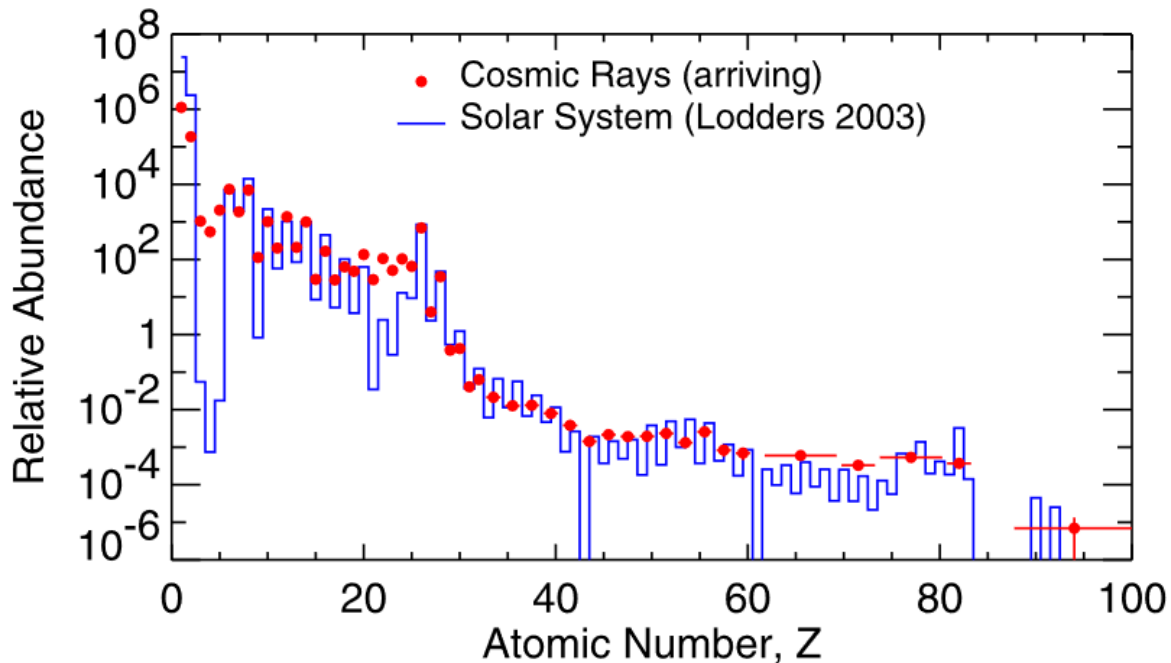
Figure 1.4: The relative elemental abundances of solar system material, compared to the relative abundances detected in $E \leq 1 GeV/nucleon$ arriving cosmic rays. Source: Wiedenbeck et al. [2007]

Protons account for the vast majority of the flux of cosmic rays, with only $\approx$ 10% comprised of helium nuclei and lesser amounts of nuclei of heavier elements, antimatter, electrons,

and positrons. The relative elemental abundances found in cosmic rays, in comparison to material in our solar system, are shown in Figure 1.4. Of note, both cosmic rays and solar system material contain peaks at elements with even atomic numbers. This is called the Oddo-Harkins rule (or odd-even effect) and states that even-Z elements are generally more abundant than their odd-Z neighbors (Oddo [1914], Harkins [1917]). Notable exceptions can be seen in the case of abundant $Z = 1$ Hydrogen and in the lack of $Z = 4$ Beryllium. The dearth of Beryllium could be attributed to its single stable isotope, in contrast to its neighbors who each have two stable isotopes.

Comparing the two populations reveals that cosmic rays contain a significant overabundance of Li, Be, and B ($Z = 3, 4, 5$). Similar overabundances also exist for F, Sc, Ti, V, Cr, and Mn ($Z = 9, 21 - 25$). These overabundances are evidence of two different categories of cosmic rays. The first category, primary cosmic rays, contains electrons, protons, He, C, and other elements created abundantly in stellar nucleosynthesis. Primary cosmic rays have abundances in agreement with what is found in the solar system. Secondary cosmic rays are then the elements generated either by the interactions between primary cosmic rays with the Interstellar Medium (ISM), or by the decay of unstable species during transit (Grenier et al. [2015]). Note that this definition is separate from "atmospheric secondaries", which are the particles produced by interactions between cosmic rays and the Earth's atmosphere. Data from the Alpha-Magnetic Spectrometer (AMS-02), located on board the ISS, suggests that a further distinction between secondaries and primaries can be seen in their spectral indices' rigidity dependence, as illustrated in Figure 1.5 (Battiston [2020]).
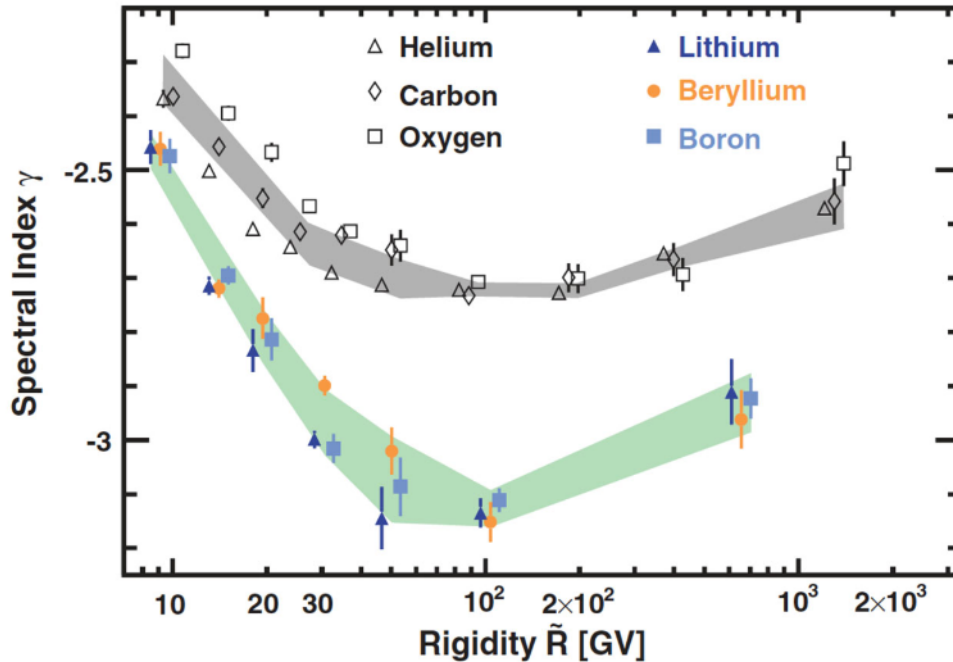
Figure 1.5: Comparison of the spectral indices of primaries He, C, and O and their rigidity dependence against the same for secondaries Li, Be, and B. Some points are displaced horizontally and shading has been added, both for visual clarity. Source: Battiston [2020].

1.5   Cosmic Ray Propagation

So far we have discussed what cosmic rays are and where they likely come from. Now, we turn our discussion to cosmic ray propagation - what happens as they traverse the vast reaches of space on their journey through their galaxies and beyond. Since cosmic rays are charged particles their paths deflect when passing through magnetic fields, which results in them not pointing back to their sources. The magnetic fields in the Milky Way are irregular and diffusive propagation within them creates a nearly isotropic flux of cosmic rays arriving at Earth that no longer point back to their sources. The GALPROP model of cosmic ray transport uses numerical methods to solve a set of differential equations for galactic cosmic ray density in a spacial grid of adjustable step size, given source distributions and boundary conditions. The cosmic ray transport equation, equation 1.1, includes convection, spatial diffusion, momentum diffusion-reacceleration, nuclear fragmentation, radioactive decay, and

9
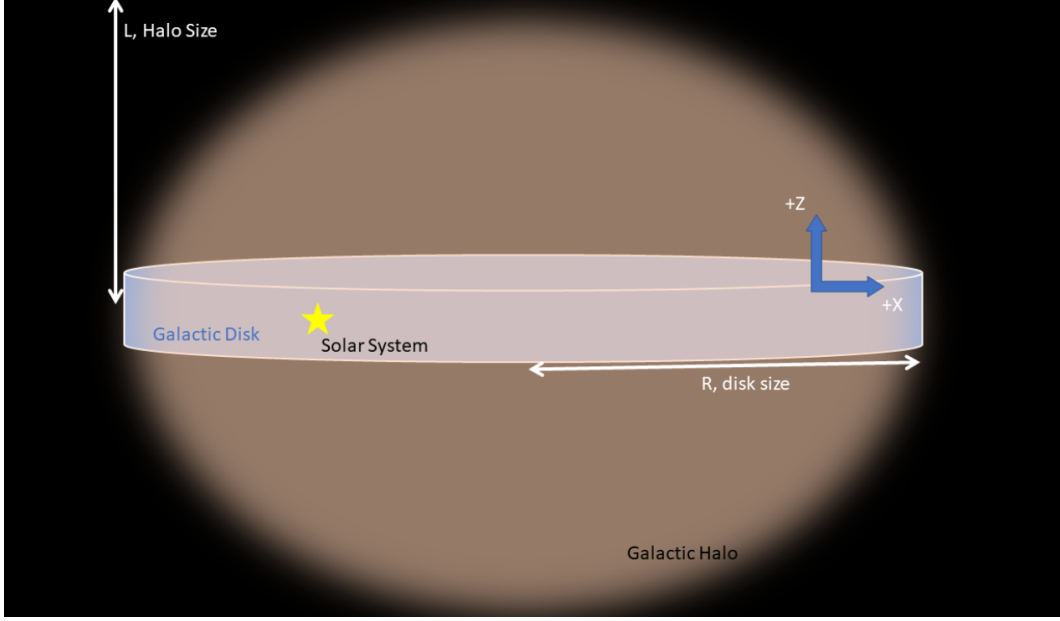
Figure 1.6: The geometry used in GALPROP's simulation of cosmic-ray transport. The Galactic Disk is in the x-y plane with boundary conditions at 20 kpc, and the Galactic Halo size L is the location of the boundary in z. Source: McBride [2021].

production of secondary particles and isotopes. $\psi(\vec{r}, p, t)$ is the cosmic-ray particle density per unit of total particle momentum, $q(\vec{r}, p)$ is the source term, $D_{xx} = \beta D_0 \rho^\delta$ is the spacial diffusion term (where ρ is the magnetic rigidity and δ is the rigidity power law index), D_{pp} is the momentum space diffusion term, $\vec{V}$ is the convection velocity term, and τ_f and τ_r are the timescales for fragmentation and radioactive decay [Trotta et al., 2011].

$$\frac{\partial \psi}{\partial t} = q(\vec{r}, p) + \nabla \cdot (D_{xx} \nabla \psi - \vec{V}\psi) + \frac{\partial}{\partial p} p^2 D_{pp} \frac{\partial}{\partial p} \frac{1}{p^2} \psi - \frac{\partial}{\partial p} [\dot{p}\psi - \frac{p}{3}(\nabla \cdot \vec{V})\psi] - \frac{1}{\tau_f}\psi - \frac{1}{\tau_r}\psi \quad (1.1)$$

This model is the one used by the HELIX collaboration to find the scientific impact of our expected measurements. A GALPROP simulation and analysis made by collaborator Dr. Keith McBride at the Ohio State University investigated the impact of expected HELIX resolution on the parameter space of the diffusion and halo-size parameters. The geometry used in this analysis is shown in Figure 1.6 [McBride, 2021].

10

CHAPTER 2

HELIX OVERVIEW

2.1 Scientific Motivation

The High Energy Light Isotope eXperiment (HELIX) is a balloon-borne magnet spectrometer. By measuring the charge, velocity, and rigidity of particles before they interact in Earth's atmosphere, HELIX will determine the elemental and isotopic abundances of key light isotopes in the cosmic ray flux. A program consisting of two flights will make these measurements of light cosmic rays from below ~ 1 GeV/n to above ~ 10 GeV/n. HELIX's unique design consists of a strong (1 Tesla) magnetic field produced by a superconducting magnet in combination with a proximity focused aerogel Ring Imaging Cherenkov (RICH) detector, resulting in high precision measurements of both particle rigidity and velocity.

2.1.1 Elemental Ratios

In the past, measurements of light cosmic rays at lower energies have offered valuable insights into the origin and behavior of cosmic rays. Ratios of light elements in the cosmic ray flux serve as probes of the amount of material that the particle passes through on its way from origin to detection, called the grammage. Grammage can in turn be related to the escape time of cosmic rays in our galaxy:

$$X(E) = \bar{n}\mu v \tau_{esc}(E) \tag{2.1}$$

Where $\bar{n}$ is the mean gas density in the Galaxy volume, μ is the mean mass of the gas, v is the speed of the particles, and $\tau_{esc}(E)$ is the energy-dependent escape time. The galactic halo size, L, and a diffusion coefficient D can then be introduced such that $\tau_{esc} \sim L^2/D$ (Blasi [2013]). The elemental ratios themselves are typically proportional to L/D.

Perhaps the most well known of these elemental abundance ratios is the Boron-to-Carbon ratio. Boron in the cosmic ray flux is largely produced from the spallation of Carbon, Nitrogen, and Oxygen nuclei, and so Boron's ratio with Carbon (being used as a representative primary) can probe the material pathlength through which the primaries pass (Mueller et al. [1991], Engelmann et al. [1990], Strong et al. [2007], Swordy et al. [1990]). Measurements of this ratio, such as those made by AMS-02 (Aguilar et al. [2016]), provide invaluable constraints on models of the cosmic ray environment. An example of these constraints can be seen in Figure 2.1.
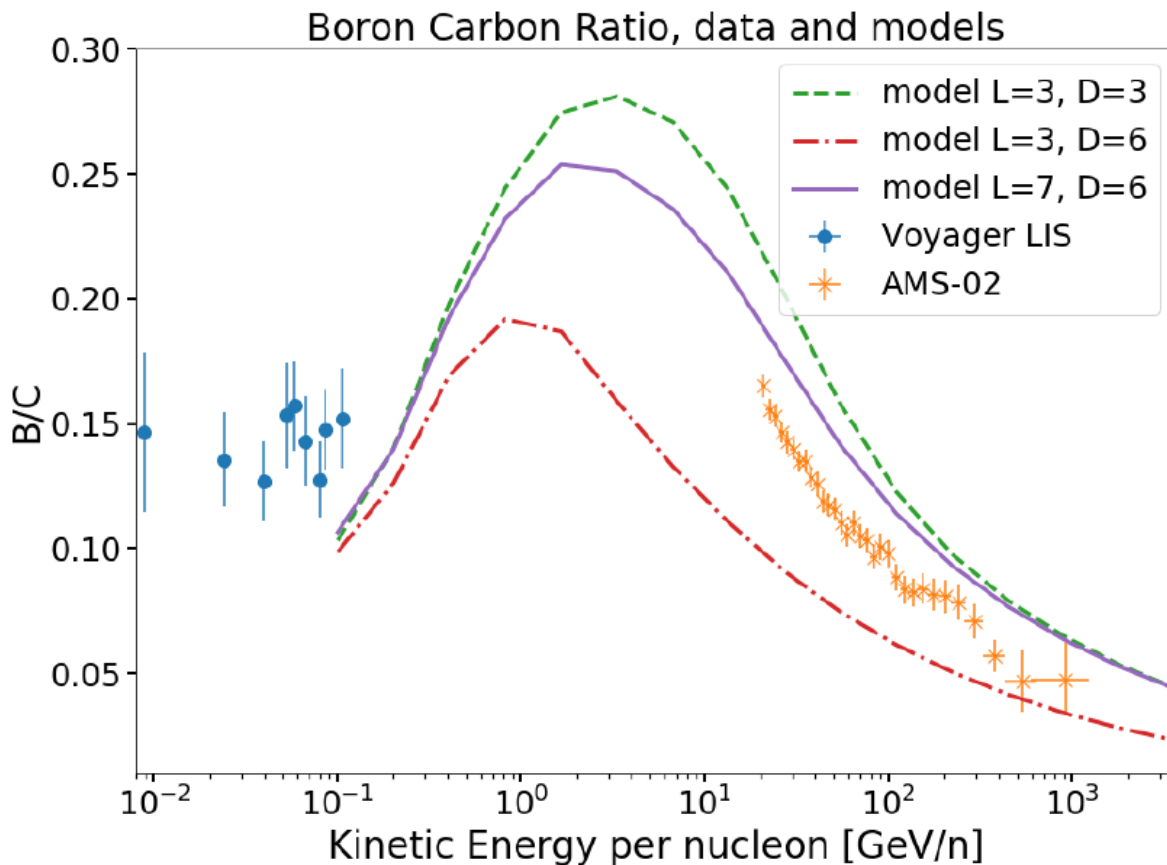
Figure 2.1: Observed B/C ratios vs kinetic energy per nucleon. Data from AMS-02 and Voyager are shown against three GALPROP models, each using a different combination of halo size and diffusion coefficient. Source: McBride [2021]

Measurements of stable isotope ratios are clearly critical to understanding the cosmic ray flux; however, they are insufficient to fully constrain models of cosmic ray propagation. As previously mentioned, in standard diffusion-convection models ratios of stable secondaries to primaries such as B/C are proportional to the ratio of halo size to the diffusion coefficient (L/D) and so may be used to constrain this ratio. With stable elemental ratios alone, a significant degeneracy continues to exist. To better constrain confinement time $\tau_{esc} \sim L^2/D$ along with material pathlength, additional measurements are needed.
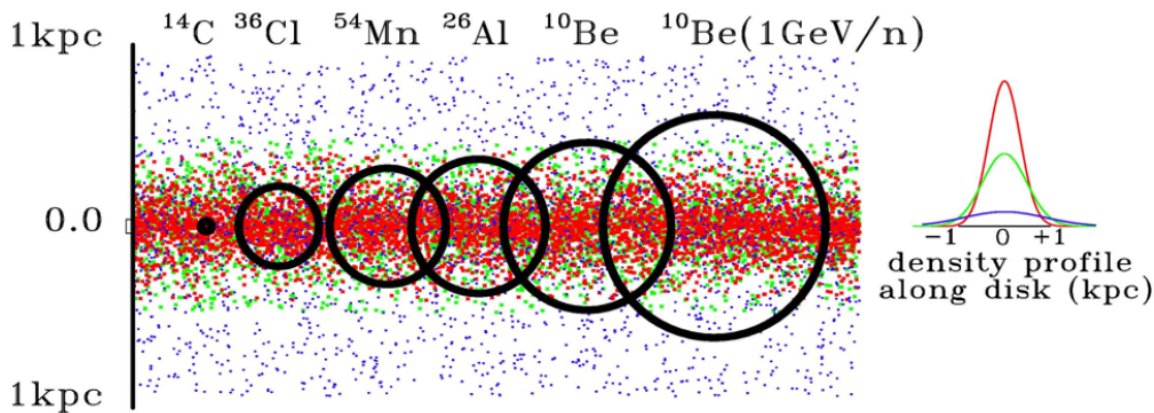
Figure 2.2: Schematic illustration demonstrating the regions sampled by several radioactive isotope clock nuclei at $\sim$0.3Gev/n. The furthest right circle demonstrates how at higher energies, the time-dilated clock allows for a greater volume to be sampled. A diffusion coefficient of $2\mathrm{x}10^{28}$ cm^{2}s^{-1} is assumed. Source: Mewaldt et al. [2001]

2.1.2 Radioactive Isotope Ratios

Radioactive isotope ratios are critical in measuring the confinement time of cosmic rays in our galaxy. Radioactive isotopes with a half life similar to the timescales of cosmic ray processes provide valuable insight into the nature of cosmic ray propagation, constraining models independently of stable secondary ratios(Mewaldt et al. [2001]). These radioactive isotopes are thus known as "clock" isotopes. In addition to measuring isotopes with a variety of half lives, the observed half-lives of these isotopes can be varied via time dilation by measuring over a range of kinetic energies, as shown in Figure 2.2. This means larger regions of the

galaxy can be explored with this method by measuring the ratios at higher energies.

Among the most valuable clock isotopes is ^{10}Be, an isotope with decays via β-decay to stable ^{10}B with a half life of ∼1.39 Myr (Chmeleff et al. [2010], Korschinek et al. [2010]). Be is produced by interactions of heavier cosmic rays with the ISM, not stellar nucleosynthesis, and so the ratio of radioactive ^{10}Be to stable ^{9}Be is solely determined by the mechanics of cosmic ray propagation. It has notably been used in the past to estimate the mean confinement lifetimes of cosmic rays within Leaky Box models to be ∼15 Myr. This estimate can then be used to in turn estimate the total power output required from the Galactic cosmic-ray sources (Simpson and Garcia-Munoz [1988], Wiedenbeck and Greiner [1980], Yanasak et al. [2001]). Using more realistic diffusion halo models, as described in the prior subsection, these measurements can be combined with stable isotope ratios to to constrain the diffusion coefficient D and galactic halo size L.
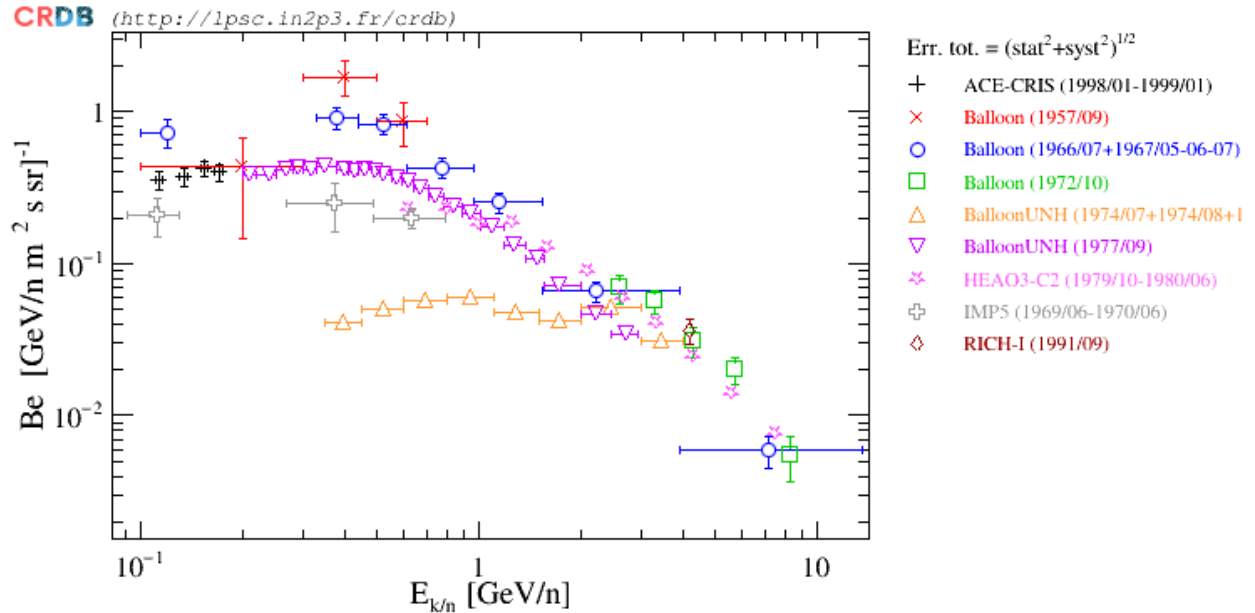
Figure 2.3: Cosmic ray flux of elemental Be, plot generated from Maurin et al. [2014] using data from von Rosenvinge et al. [1969], Lezniak and Webber [1978], Orth et al. [1978], Webber and Yushak [1979], Engelmann et al. [1990], Buckley et al. [1994].

The total number of Be events observed by HELIX is determined by three factors - the geometric acceptance, the experiment's livetime, and cuts lowering the experiment's
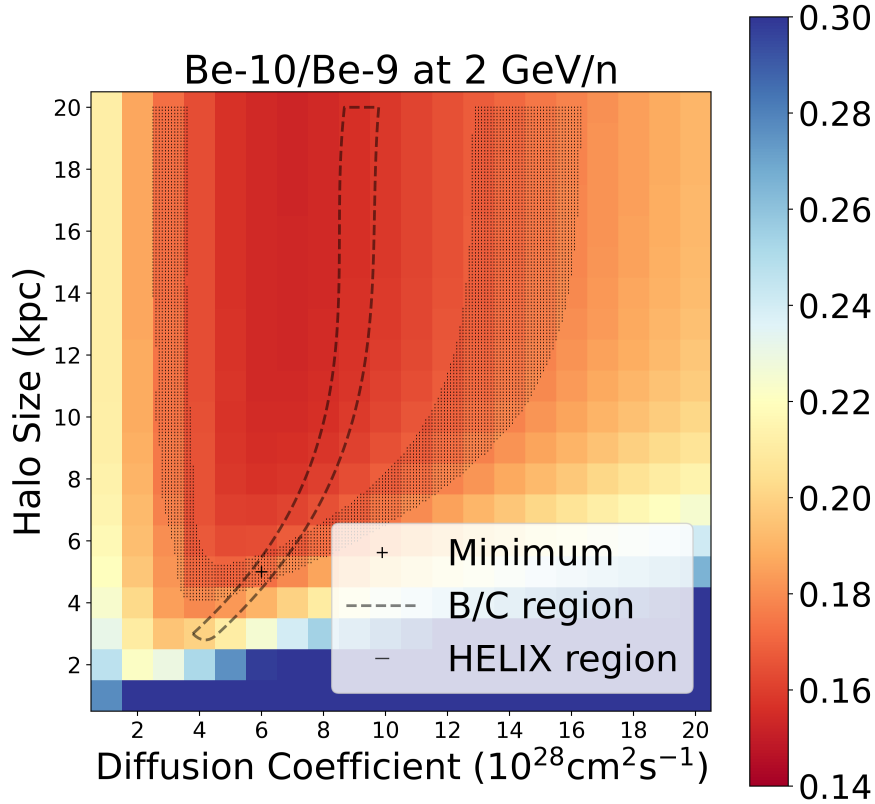
Figure 2.4: GALPROP predictions of the ^{10}Be/^{10}Be ratio, at a kinetic energy of 2 GeV/n, for a range of 20 values each of Halo Size L and diffusion coefficient D. A hypothetical measurement of 0.17 has been chosen for the beryllium ratio, for illustrative purposes. The two bands shown are a 95% confidence interval set based on AMS-02 measurements of B/C, and a 1σ band for a Be isotope ratio as described in the text. The addition of HELIX data reduces the allowed phase space by a factor of $\sim$10. Source: McBride [2021].

efficiency. HELIX's geometric acceptance of 0.09m^{2}sr, when combined with the flux of Be cosmic rays (see Figure 2.3), can be used to make an estimate of the raw number of Be events HELIX expects to see. For example, with 10 total days of flight time HELIX can expect to see more than $\sim$7000 Be nuclei over 2 GeV/n of kinetic energy, which could correspond more than $\sim$1000 individually resolved ^{10}Be nuclei. Around 2 GeV/n of kinetic energy, we could expect $\sim$ 200 ^{10}Be in a 0.3 GeV/n width bin. Using only this measurement, already

strong discrimination between models can be achieved, as is seen in Figure 2.4.

2.1.3   Cosmic Ray Measurements

Until recently, magnet spectrometers in balloons and in space have only been able to provide isotopic contribution data for the lightest elements, and only up to limited energy ranges. The space-based experiments AMS-01 and PAMELA have measured H and B up to 1 GeV/n [Aguilar et al., 2011, Menn et al., 2013, 2018]. The balloon-borne experiment IMAX has measured ^{3}He/^{4}He up to 4 GeV/n [Reimer et al., 1998]. ISOMAX, another balloon, has measured the Li, Be, and B isotopes up to 1-2 GeV/n, albeit with limited statistics [Hams et al., 2004a].

HELIX's primary design goal is to make several world-leading measurements of isotopic abundances. This will complement existing cosmic-ray experiments by providing the means to interpret their data via these isotopic abundance measurements. These complementary missions include AMS-02, PAMELA, DAMPE [Chang et al., 2017], ISS-CREAM [Seo, 2012], and CALET[Yoshida et al., 2012].

The primary scientific goals of HELIX are the first mass-resolved measurements of ^{10}Be/^{9}Be above 2 GeV/n and of ^{7}Li/^{6}Li and ^{10}B/^{11}Be above about 1 GeV/n, the first measurement of ^{22}Ne/^{20}Ne above 1 GeV/n, and a high statistics measurment of ^{3}He/^{4}He from ~0.3 to ~12 GeV/n. HELIX will also be able to measure numerous other isotopic and abundance ratios in cosmic rays in addition to its primary goals, such as the first measurements of ^{15}N/^{14}N, ^{18}O/^{16}O, ^{13}C/^{12}C above 1 GeV/n [HELIX Collaboration, 2021].

The most desired measurements of those HELIX is designed to make are of the ^{10}Be/^{9}Be ratio from ~0.3 to ~10 GeV/n. Achieving a Be isotope ratio measurement of this quality necessitates the ability to resolve isotopes of Be at an individual level. Lower precision measurements of the mass would increase systematic uncertainty in the isotopic ratios in each energy bin. HELIX will serve as an excellent complement to the AMS-02 experiment
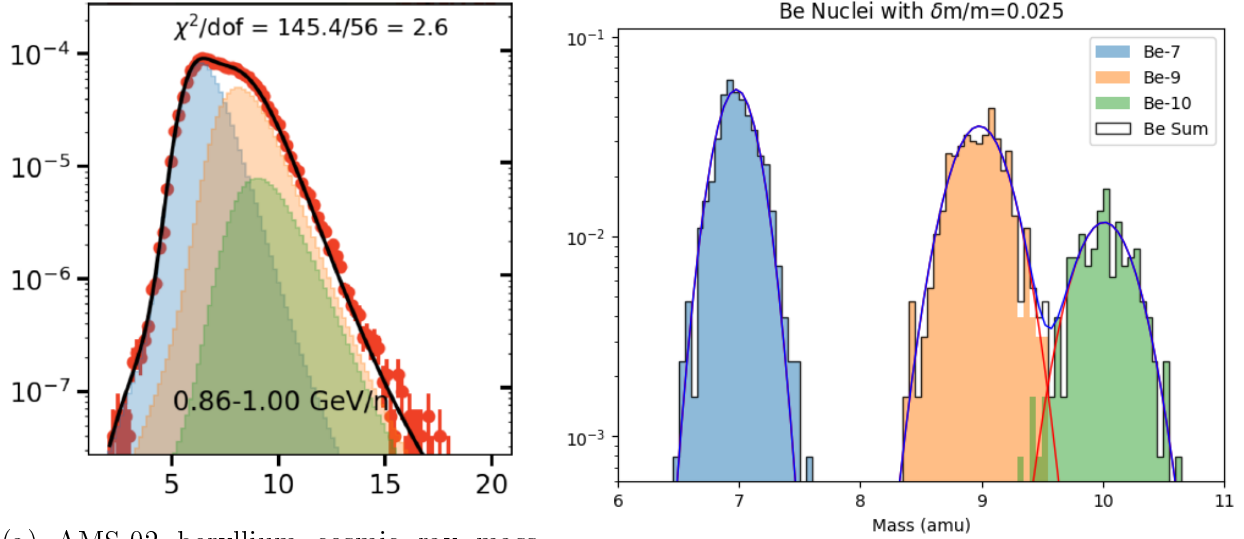
(a) AMS-02 beryllium cosmic ray mass histogram, as shown at the 2021 ICRC [Derome, 2021]. The colored sections are the surmised isotope contributions.

(b) Simulated distribution of measured Be isotope masses around 2 GeV/nuc (with a 0.3 GeV/n bin), using a resolution of $\sigma m/m=0.025$, HELIX's target resolution.

Figure 2.5: Comparison of AMS-02 and expected HELIX mass resolution

by providing the first mass-resolved measurements of beryllium isotopes at energies up to $\sim$10 GeV/n. HELIX achieves this higher resolution by employing a magnetic field that a factor of $\sim$7 stronger than AMS-02's, as well as by a significant reduction of the multiple scattering term in the rigidity resolution through the use of a tracker with a lower mass density. AMS-02's permanent magnet has a smaller magnetic field than the originally planned superconducting magnet, resulting in a lower isotopic resolution. HELIX's field is produced via a superconducting magnet, which trades a longer hold time for a much stronger field. A comparison of AMS-02's reported mass resolution with HELIX's target resolution is shown in Figure 2.5.

The science impact of HELIX's design considerations is an important part of this project, and will be discussed in further detail in section 3.1.

2.2   Payload Overview

HELIX's payload is a magnet spectrometer built around a 1 Tesla superconducting magnet. It contains a gas drift-chamber tracker to measure particle rigidity, a Ring Imaging Cherenkov detector (RICH) providing velocity measurements at higher targeted energies, a hodoscope for improved particle tracking prior to the RICH's radiator, a time-of-flight system for measuring particle charge, velocity at lower targeted energies, and providing an instrument trigger. HELIX's payload with the detectors labeled is shown in Figure 2.6. The instrument will have a geometric acceptance of 0.09 m^2sr, large enough to support high-statistics measurements of isotope ratios in the targeted energy range.
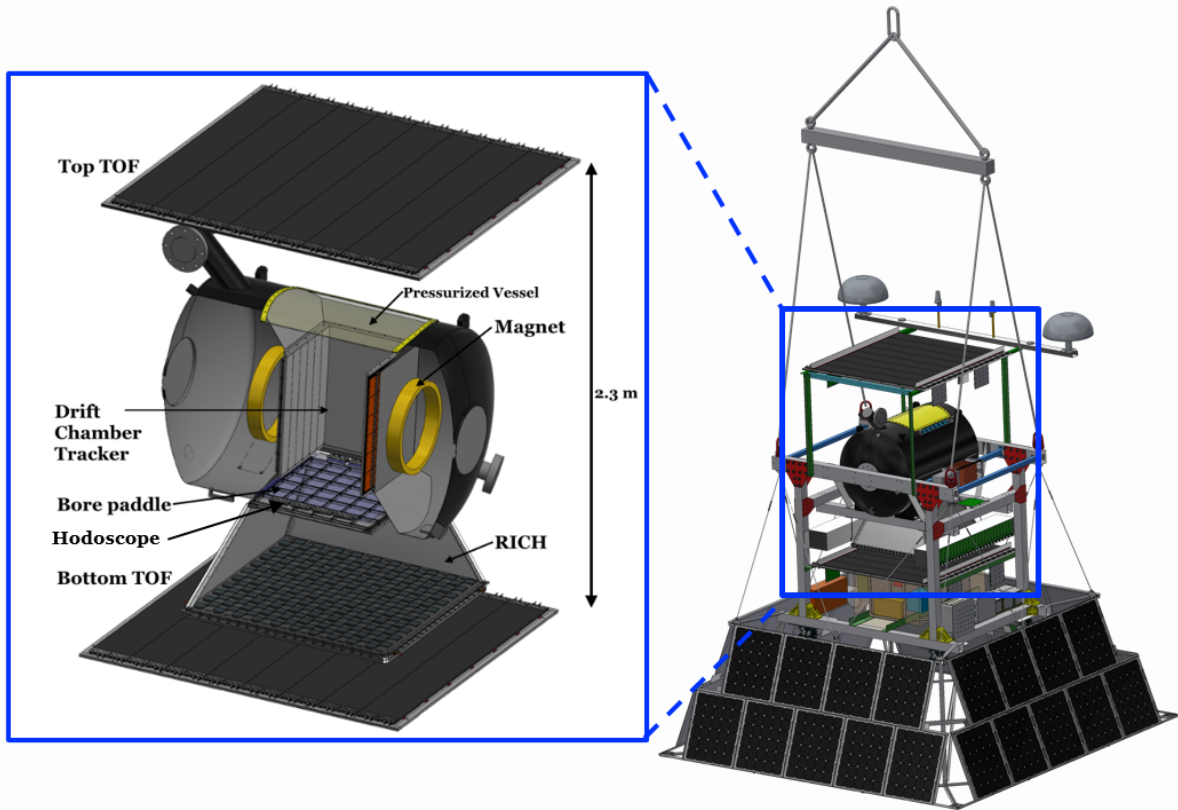
Figure 2.6: The HELIX balloon payload, with a detailed view of the detectors. The inset is rotated around the vertical for a better view. Adapted from Allison et al. [2019]

HELIX's payload has a mass of ~1960kg, and is planned to fly at an altitude of 37 km

using a "34 Heavy" long duration balloon, provide by NASA's Columbia Scientific Balloon Facility (CSBF). HELIX is designed for long duration flights, and has the flexibility to support either a northern hemisphere flight from Kiruna in Sweden westward to Canada, or a southern hemisphere flight around Antarctica launched from McMurdo Station. Examples of each of these flights are shown in Figures 2.7 and 2.8. The superconducting magnet's expected hold time is ~5 days, which would be supported by either flight path. Any time in flight beyond this hold time is still of high value, as particles passing through the instrument when no magnetic field is present, called "straight throughs", still provide valuable information used calibrate the instrument response.
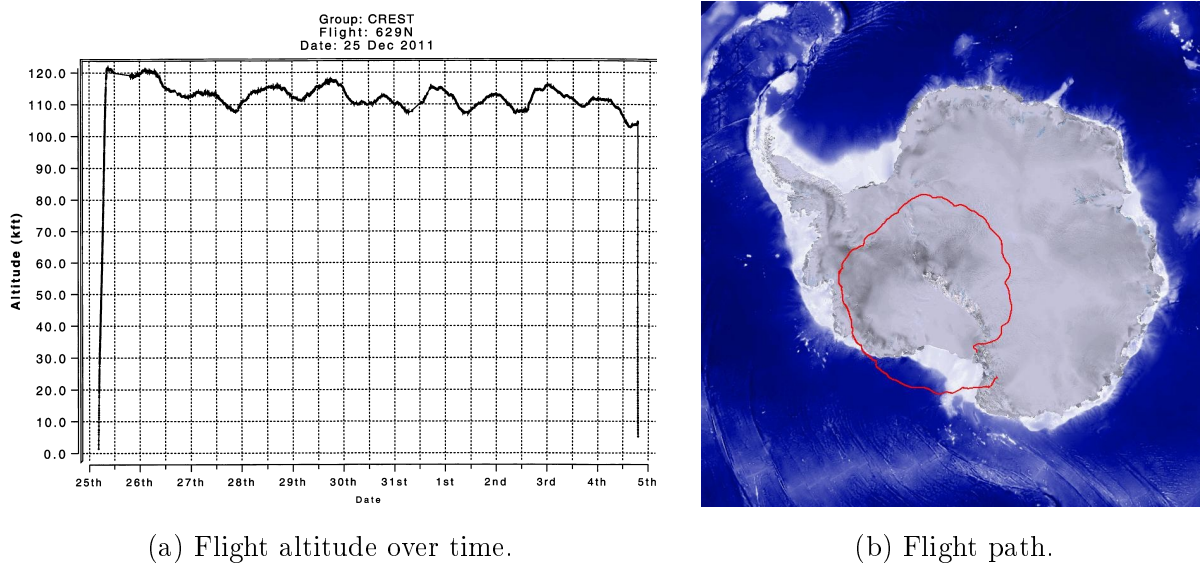
(a) Flight altitude over time.

(b) Flight path.

Figure 2.7: CREST, a 34 Heavy balloon payload flying an Antarctic path. Retrieved from `https://www.csbf.nasa.gov/balloons.html` and `https://stratocat.com.ar/fichas-e/2011/MCM-20111225.htm` respectively.

In ballooning, a gondola is the payload suspended beneath the balloon itself. A CAD rendering of the gondola with important non-detector elements labeled is shown in Figure 2.9. Due to the strong magnetic field produced by the superconducting magnet, all gondola components must be non-magnetic. Additional design requirements include safe and easy access to the magnet's "stack" for filling cryogen, maximum thermal separation between
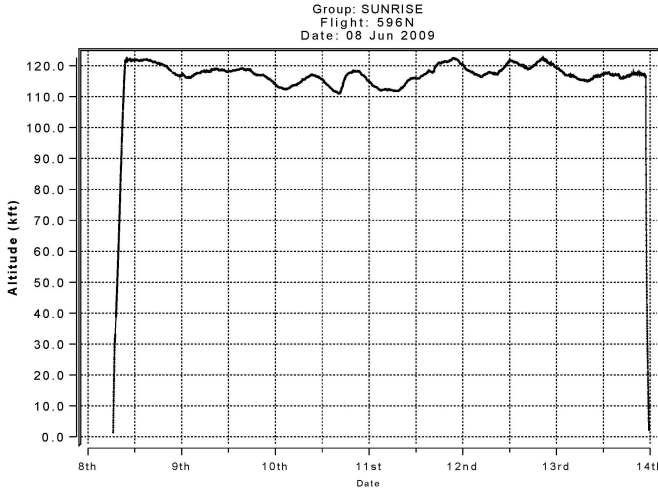
(a) Flight altitude over time.
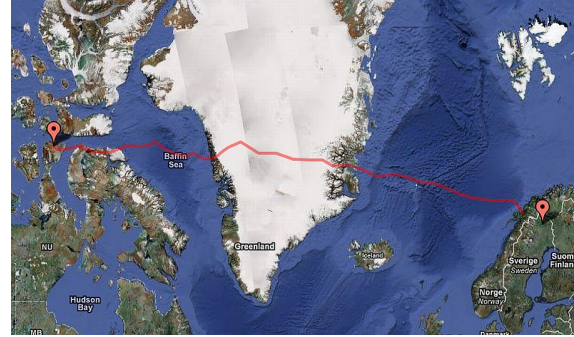
(b) Flight path.

Figure 2.8: SUNRISE, a 34 Heavy balloon payload flying a Sweden-to-Canada path. Retrieved from `https://www.csbf.nasa.gov/balloons.html` and `https://stratocat.com.ar/fichas-e/2009/KRN-20090608.htm` respectively.

heat producing systems and the cryogenic magnet, and minimal additional weight.

HELIX's payload is supported by a structural frame of bolted rectangular tubes and angle sections made of aluminum, bolted together. None of the structural frame is welded, making for relatively easy construction. The magnet is the heaviest individual component of the payload, weighing in at slightly over 1,000 lbs. The magnet's three feet are bolted to the gondola, and is additionally attached to the gondola at two by two flanges at either end of the magnet, in line with the axis of the magnet coils. The RICH is attached at the focal plane by four metal supports, hanging from the crossbeams under the magnet's feet. The time-of-flight (ToF) scintillators are supported on aluminum honeycomb paddles, with the bottom ToF resting on two aluminum angles and the top ToF supported by four aluminum angle bars, tensioned with adjustable aluminium rods. The Support Instrument Package (SIP) provided by CSBF will sit on a honeycomb deck attached to the bottom members of the frame. Although while in flight the payload will be supported at the four swivel hoist rings on the four corners of the chassis, while being constructed the solar panels are removed and the chassis rests on the floor, supported by by four removable swiveling caster wheels

20

(Stillwell [2018]).
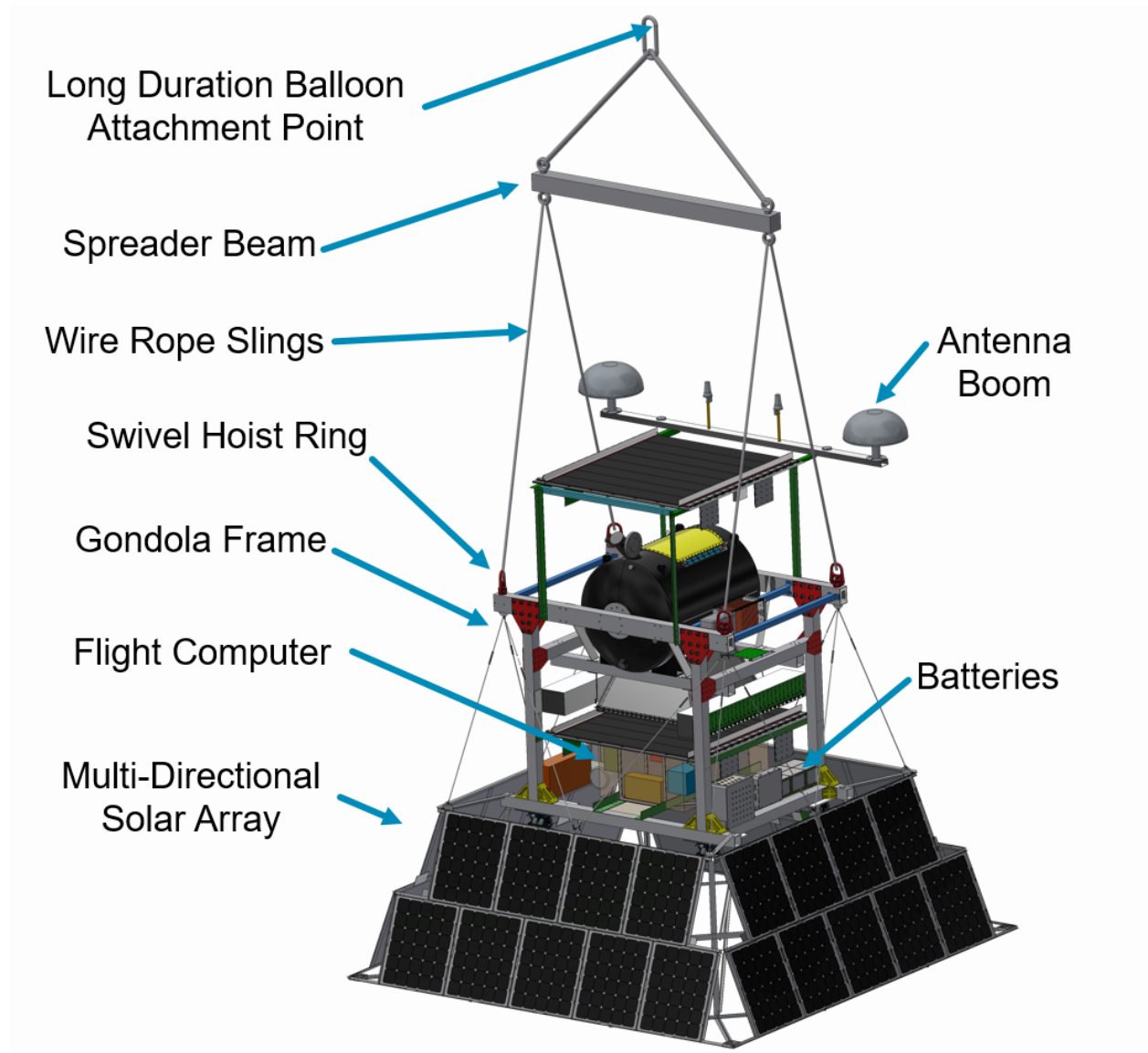
Figure 2.9: The HELIX balloon payload, with important non-detector elements labeled. Adapted from Allison et al. [2019]

2.3   Time of Flight and Instrument Trigger

HELIX's time-of-flight system, constructed by HELIX's Penn State University collaborators, is designed to provide a timing resolution better than 50 ps for elements of charge Z=3

(lithium) or greater, and has a spacing of 2.3 m between the upper and lower paddles. This design allows the ToF system to meet HELIX's requirements of velocity resolution of $\gamma \frac{\delta \beta}{\beta} \leq 2.5\%$ up to $\sim$1 GeV/n. At energies higher than $\sim$1 GeV/n the RICH is the used for velocity measurements. Critically, the ToF provides a charge measurement of each particle. The ToF achieves a charge resolution better than 0.1e, with good linearity up to Z=11.

2.3.1 Upper and Lower Paddles

The ToF consists of two layers 2.3 m apart vertically, one raised above the rest of the instrument, and one below the other detectors (see Figure 2.6). Each layer is made of eight 1.0 cm thick Eljen Technologies EJ-200 fast plastic scintillator paddles. Each paddle has a dimension of 20 cm $\times$ 160 cm, arranged to cover a square area of approximately 160 cm $\times$ 160 cm. When a charged particle passes through the scintillator it deposits energy, some of which is then radiated as optical light by the scintillator. This light emitted by the scintillator is a function of the energy deposited, which is described by the Bethe-Bloch equation. In addition to a velocity dependence, the Bethe-Bloch equation describes a charge squared dependence and so by measuring the light emitted in the scintillator the charge may be reconstructed.

Each paddle is wrapped in white Teflon to contain and reflect the scintillation light, maximizing the signal transmitted to the ends of the paddles. After the readout electronics are attached, the entire structure is wrapped in black Tedlar, a material that has been found to be ideal for its conformable light-tighting. The light tighting was tested by shining a bright flashlight along the paddle and checking for a spike in signals.

Each short end of a ToF paddle is instrumented with two Front-End Electronics assemblies (FEEs) to read out the scintillation light, for a total of four per paddle. An example can be seen in Figure 2.14 These front-end assemblies each contain four Hamamatsu S13360-6050VE SiPMs (Hamamatsu [2016]). Each ToF SiPM has an effective photosensitive area of
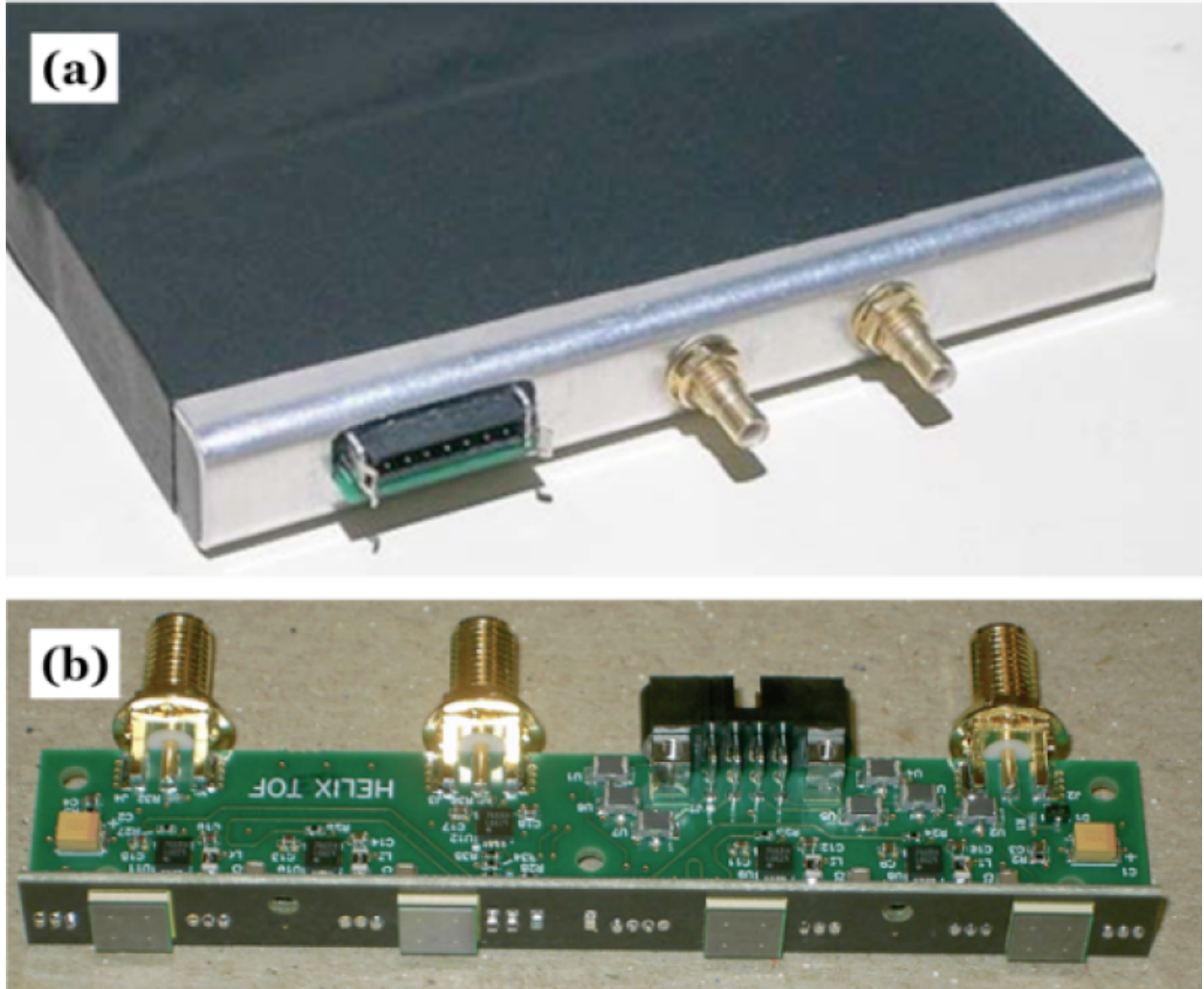
Figure 2.10: (a) A prototype ToF FEE board mounted to a paddle. (b) A ToF FEE board, with the four SiPMs visible. The 3 SMA connectors are for the high gain, low gain, and an internal LED trigger. Source: Yu [2022]

6m × 6mm is operated at a bias voltage of ∼57 V, with small corrections on each channel to achieve uniform gain across each channel. The bias is additionally modified in response to changes in temperature detected within each FEE, to correct for temperature dependence in the SiPMs. The four SiPMs in each FEE have their outputs passively summed. Two outputs are formed from this signal, a low gain (slow) output used to measure the charge of the particle, and a high gain (fast) output used to more precisely measure the time of the event. The fast output is sent to a leading-edge discriminator whose logic pulse is then sent

to a custom time-to-amplitude converter. The slow output is passed through a shaper. Both outputs are then digitized with a 40 MSPS 14-bit ADC.
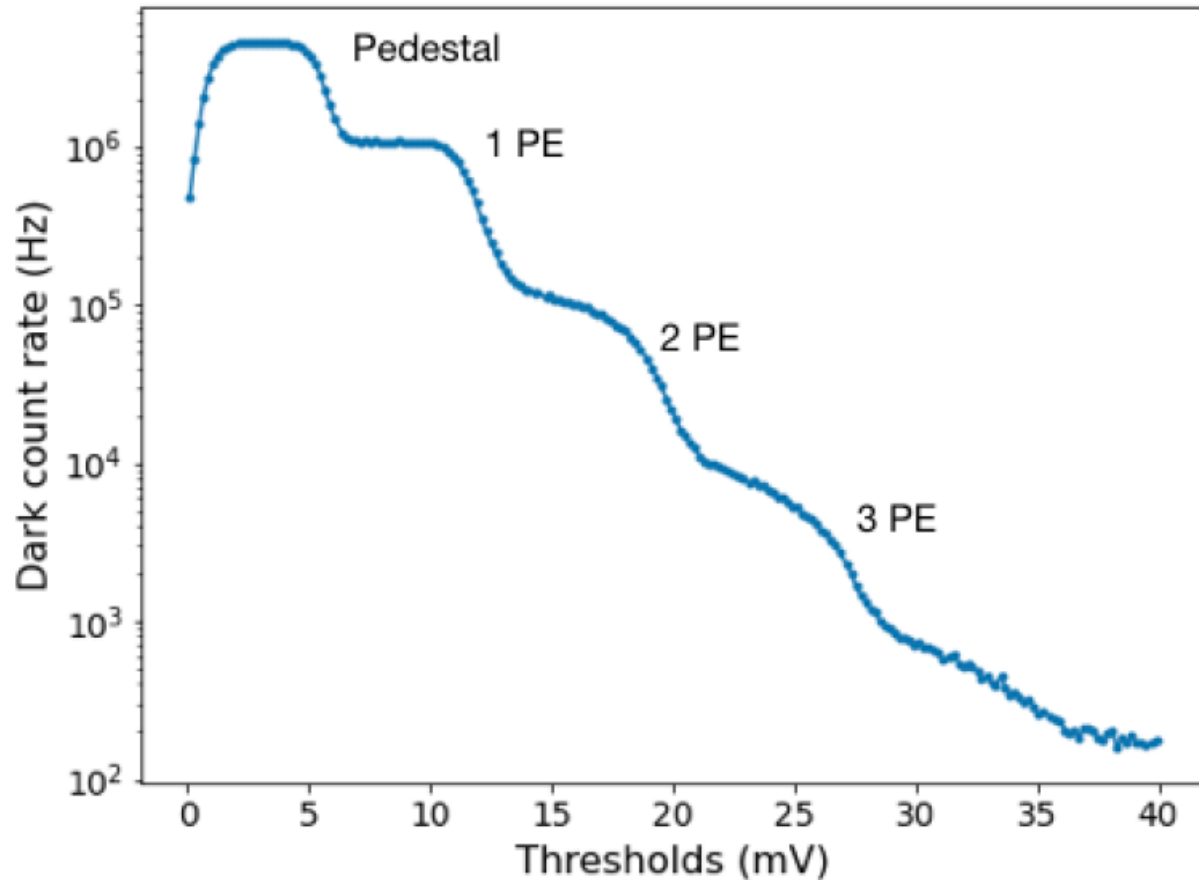
Figure 2.11: An example of the dark count rate vs threshold of a ToF SiPM, with the PE corresponding to the plateau transition labeled. Source: Yu [2022]

The SiPMs used in the ToF FEEs were gain matched using a different procedure than was used for the SiPMs used in the RICH focal plane (discussed later). The ToF's gain matching process was performed by measuring threshold scans of each channel's dark count rate. As thermal excitations (dark events) are the dominant noise in SiPMs, a threshold scan with a discriminator should produce plateaus in frequency in between each PE signal height (post-gain). This effect is shown in Figure 2.11. By fitting the edges of these plateaus, the width in threshold voltage between each PE can be found. These widths characterize the
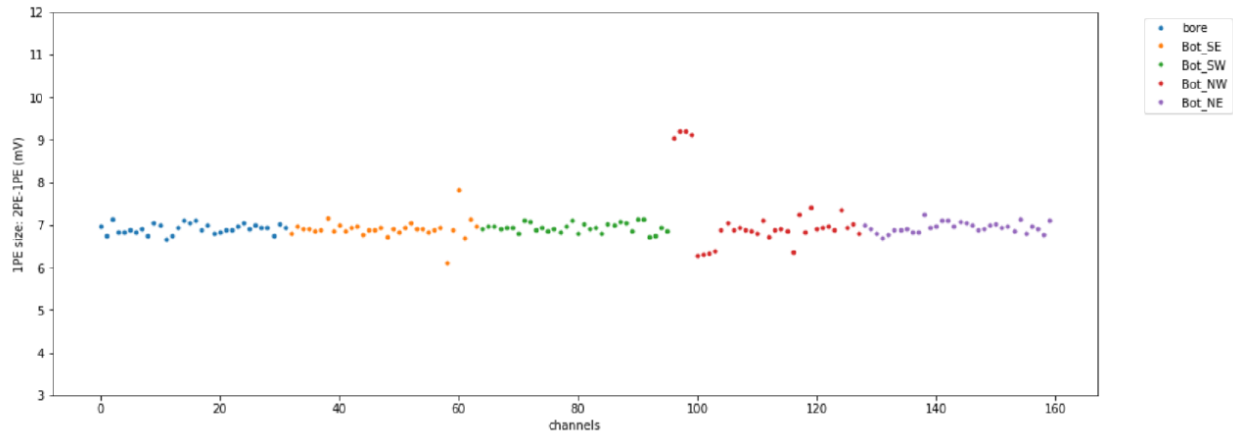
Figure 2.12: The gains of the SiPMs on the bore and bottom paddles, after gain matching. Source: Yu [2022]

gain of the channel, and modifying the gain either via the front-end amplification or, as is used in this case, by modifying the bias voltage applied to the SiPM allows all channel gains to be made the same (Yu [2022]).

The velocity of the particle is calculated by the time difference between the light's arrival in the upper and lower paddles. Positioning information can be derived within the two layers by looking at which of the paddles in each layer received light, as well as the time difference between when the signal is recorded on each instrumented end of the paddle.

Testing and calibration of the ToF electronics was performed at Penn State. To determine the timing resolution of the ToF, fast signals were injected into the readout boards. These signals were then digitized by the readout board's ADC and fit to a combination of a pedestal value for the channel, a linear term for the voltage ramp, and a polynomial term fit to the nonlinear region. By subtracting this fit from the data ΔN_{ADC}, the standard deviation of the residuals in units of ADC values, was be found. The approximately linear relationship between the ADC value and the time spent ramping was then used to transform the per-channel ADC residual standard deviation to a per channel timing resolution, as shown below (McBride [2021]).
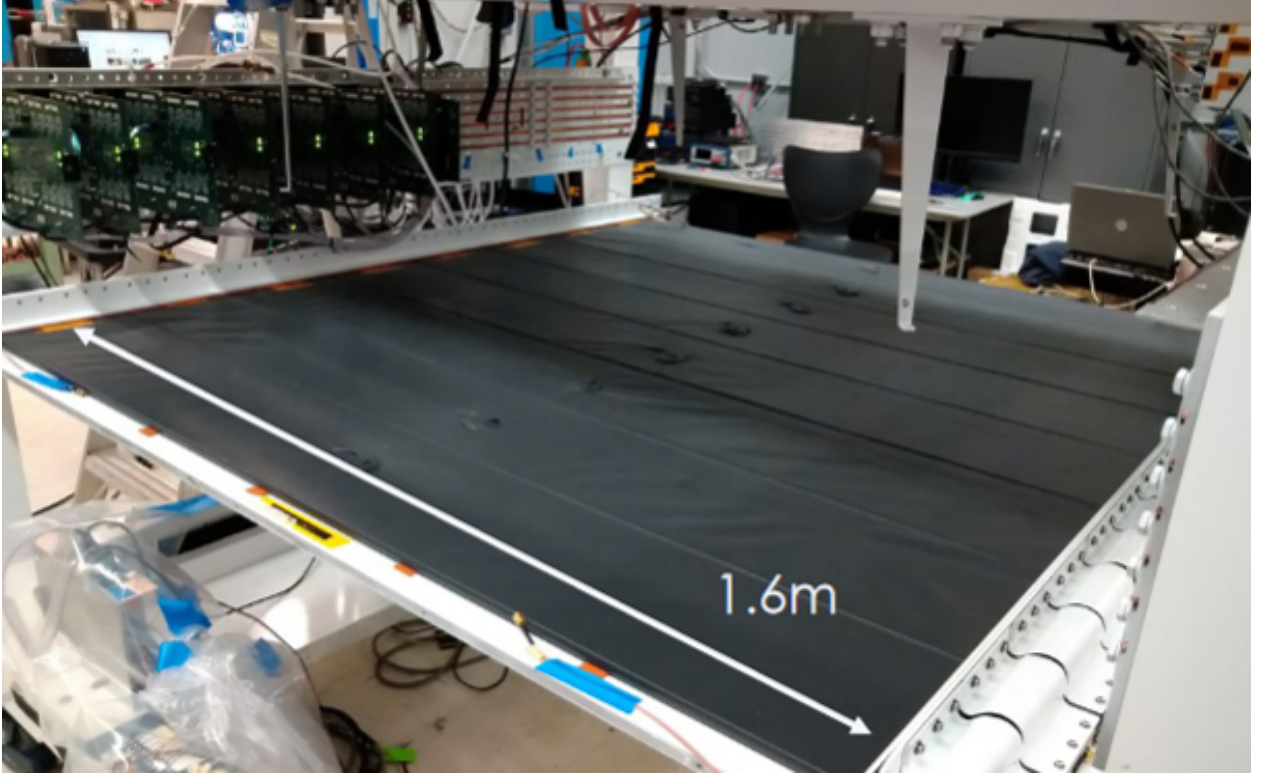
Figure 2.13: The lower Time-of-Flight, installed in the payload. The RICH cone, normally sitting above the lower ToF, is not present.

$$N_{ADC} = m_{ADC} * t \rightarrow \Delta t = \frac{\Delta N_{ADC}}{X * f_{ADC}} \qquad (2.2)$$

X in the above equation is the slope of the linear fit of ADC values to samples. The timing resolutions found via the above method were $\mathcal{O}(20\ ps)$. This timing resolution, in turn, contributes to the uncertainty in the velocity measurement of the particles. The relationship for this uncertainty (again, from McBride [2021]) is:

$$\beta = \frac{L}{c\Delta t} \rightarrow \frac{\delta\beta}{\beta} = \frac{c}{L}\delta t \qquad (2.3)$$

In addition to a time-of-arrival measurement for the particle passing through the paddle, the timing resolution characterized above can be used to find the position resolution achievable by measuring the time difference between the signal arriving at either end of the

paddle. With the $\mathcal{O}(20\ ps)$ time resolution measured, a position resolution of $\mathcal{O}(10\ mm)$ is expected along the long axis of the paddles.

2.3.2   Bore Paddle

Figure 2.14: The bore paddle, outside of the payload.

Included in the ToF system is a third layer of scintillator, placed within the bore of the magnet directly beneath the drift chamber. This layer is referred to as the "bore paddle", and serves as the HELIX instrument's trigger. Figure 2.14 shows the bore paddle removed from the payload. It is composed of the same 1.0 cm thick EJ-200 scintillator as the top and bottom ToF, with a smaller 54 cm × 60 cm cross section. It is composed of 4 (rather than 8) paddles, with the same FEEs as the rest of the ToF system attached to either end of each

27

paddle. The trigger for the instrument is generated by two stages of lookup tables (LUTs) in the "master trigger" board. The first LUT uses the top and bottom ToF layer's signals as input, and feeds the output to the second LUT. The second LUT then checks a delayed bore paddle signal in against the output of the first LUT to decide whether all three layers reported a signal within a 10 ns coincidence. If so, a trigger is issued. The signal thresholds at which a trigger is issued is adjustable, to allow for two kinds of above-threshold triggers to be defined, high-Z and low-Z.

2.4   Drift Chamber Tracker

2.4.1   Magnet

Figure 2.15: Delivery of HELIX's magnet after it's 2017 refurbishment, next to University of Michigan collaborator Noah Green. The stack is visible on the top, right hand side of the magnet.

HELIX's measurement of particle rigidity will be obtained by tracking the path of the

cosmic ray through a known magnetic field produced by a superconducting magnet. HELIX's magnet is a two-coil superconducting magnet which previously flew aboard the High-Energy Antimatter Telescope [Barwick et al., 1997]. It was designed by collaborators at the University of Michigan, and built by Cryomagnetics Inc. Its two superconducting coils are made of Niobium-Titanium alloy wire and are contained in a cryostat that is filled with liquid helium (LHe) during operation. Cooled to about 4.2 K by the LHe bath, the superconducting coils produce a 1 T magnetic field with 91.7 A of current flowing. The magnetic field is approximately uniform within the 51 cm $\times$ 51 cm $\times$ 61 cm bore of the magnet. The cryostat uses a vapor-cooled radiation shield and superinsulation instead of a liquid nitrogen jacket in order to reduce the overall mass to 420 kg. The dewar holds approximately 260 L of LHe, with an expected hold-time of $\sim$5 days. The magnet was refurbished by Cryomagnetics Inc. in August of 2017, which included painting the exterior black for better thermal efficiency, cleaning and replacing of connectors and fittings, and improved metrology of the bore. Figure 2.15 shows HELIX's magnet immediately post-refurbishment.

Once the payload is in flight, the magnet can no longer be refilled. This means that the magnet is cooled down, filled, and charged to full field strength once prior to flight, with the possibility of a LHe top-off if performed prior to the magnet being de-energized. The magnet's status is monitored through a dedicated magnet housekeeping system, consisting of LHe level sensors, temperature sensors, a pressure transducer, and flowmeters. RTDs (Resistance Temperature Diodes) are used within the dewar to measure temperature at the 4 K scale. Strips of superconducting wires are placed along the interior walls of the dewar to measure the LHe levels. By measuring the total resistance of the strips, the fraction of the strip covered by the LHe can be deduced.
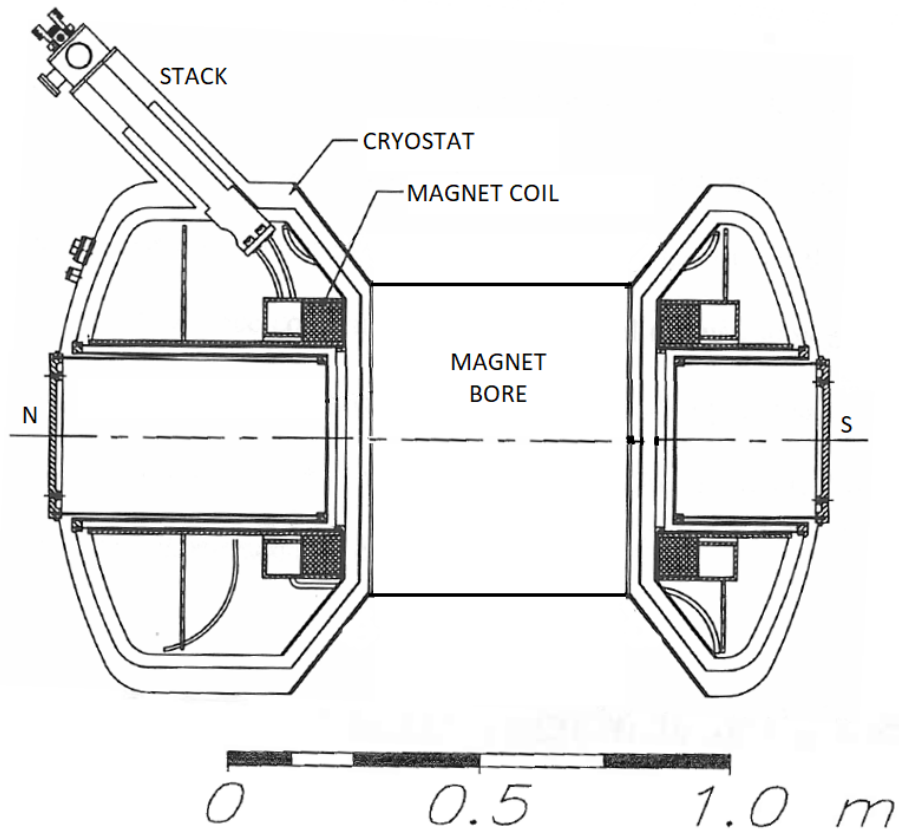
Figure 2.16: Cross section of the HEAT magnet (prior to HELIX refurbishment). The basic magnet structure remains the same in HELIX. Adapted from [Koehn, 1995].

Magnet Operation and Tests

The magnet is filled via the stack, a neck-like tube protruding from the north side of the magnet (see Figure 2.16). It contains the current leads used for charging the magnet and two fill ports for LHe, one each for the near and far end of the magnet cryostat. The procedure for filling the magnet, in short, is to first fill the dewar with liquid nitrogen (LN2) to pre-cool the interior of the magnet. This prevents the wasteful loss of LHe that would occur when filling from room temperature. Once the pre-cool is complete, the magnet is purged of LN2 by pressurizing the dewar with gaseous N2 and forcing out any remaining LN2. Once complete, the magnet is sealed and monitored for any indication of remaining

LN2 boiling off. If none is observed, the cryostat is then filled with LHe. Once filled, the magnet is charged via the stack's current leads. This is done by activating the "persistent switch heater" which heats the section of wire in the coil between the two current lead taps, causing it to become resistive. A power source provided by Cryomagnetics applies voltage across the taps until the desired current limit is reached. Once done, the persistent switch is turned off and the superconducting circuit is completed. The current limit on the supply is lowered back to zero, and with the circuit completed the magnet remains charged [Cry]. For the magnet to be safely de-energized, one of two methods is used. The first, only viable on the ground, is to hook the magnet leads to the power supply, engage the persistent switch heater, and slowly sink current into the power supply, lowering the total current slowly to zero. The flight method uses high-current, high-power diodes attached to the current leads and thermally attached to the gondola to sink the current into when the persistence switch is set to open.
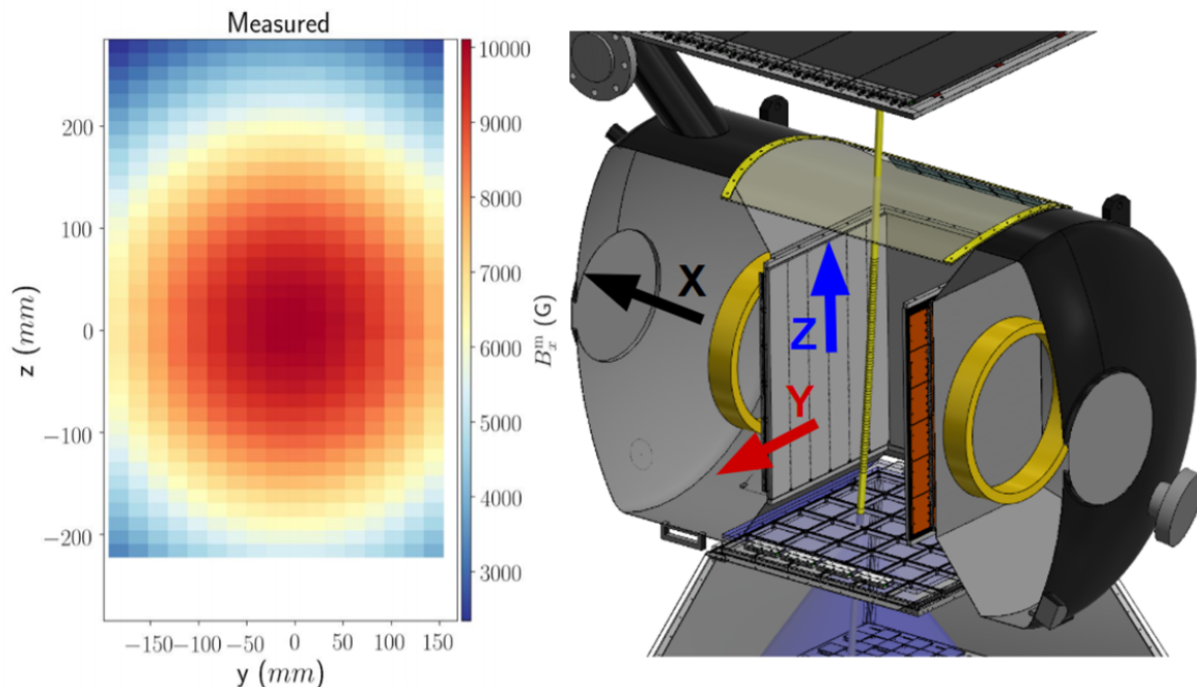
Figure 2.17: A slice in the YZ plane of the measured magnetic field strength in the X direction. Sources: McBride [2021], Mbarek [2022].

31

(a) Me, manning the dewar of LHe.

(b) LHe fill viewed from above.

Figure 2.18: Myself and Noah Green filling the magnet cryostat with liquid helium at NASA's Armstrong Test Facility in preparation for the 2022 thermal vacuum test.

The HELIX magnet has undergone a number of tests post-refurbishment, including both cooldown and charging under various conditions. These tests were: a test in 2017 at the University of Michigan, a 2019 test in vacuum at the University of Michigan's Large Vacuum Test Facility during which a 3D map of the magnet's magnetic field was created, tests in 2020 and 2021 at the University of Chicago, and in 2022 a thermal vacuum test at NASA's Armstrong Test Facility (ATF) in Ohio. An example of the magnetic field mapping is shown in Figure 2.17. Of these tests, I staffed the 2019, 2021, and 2022 tests as part of this project. During these tests I contributed to assembling and disassembling the payload, writing software for the sensors, and filling and charging the magnet (Figure 2.18), amongst the numerous other jobs that arose.

2.4.2 Tracker

$$R = \frac{pc}{Ze} = \rho B \qquad (2.4)$$

Figure 2.19: The inside of the DCT. The DCT is propped on its side, when installed this view would be top-down.

HELIX measures the rigidity of cosmic-ray particles by tracking how much they deflect in the magnetic field of the superconducting magnet. In a uniform magnetic field of magnitude B, a particle will bend in a circular path with gyroradius ρ, as defined in equation 2.4. HELIX measures this deflection with a gas Drift Chamber Tracker (DCT), designed and built at Indiana University, placed in the bore of the magnet. The tracker has an instrumented volume of $450 \times 415 \times 600$ mm (~ 0.1 m^2), and is surrounded by a hermetically sealed vessel shaped to the magnet's bore which holds the gas pressure in the tracker at 1 atm.

The DCT contains a gas mixture of 80% CO_2 and 20% Ar; as the cosmic-ray particles pass through the gas mixture they ionize some of the gas particles, leaving a path of charged particles. The DCT is instrumented with three sense-wire planes and four cathode planes. The sense-wires are interspersed with potential wires held at a nominal voltage of -3 kV while the cathode planes are held at -10 kV which, assisted by field-shaping electrodes surrounding the drift region, create a uniform drift field of 1.3 kV/cm between them. A view inside the DCT is shown in Figure 2.19. The charged particles left behind by the cosmic-ray particle induce a current in the wires as they are drawn to them. The sense wires read out this induced current at both ends - the length of the induced pulse can be used to determine

33
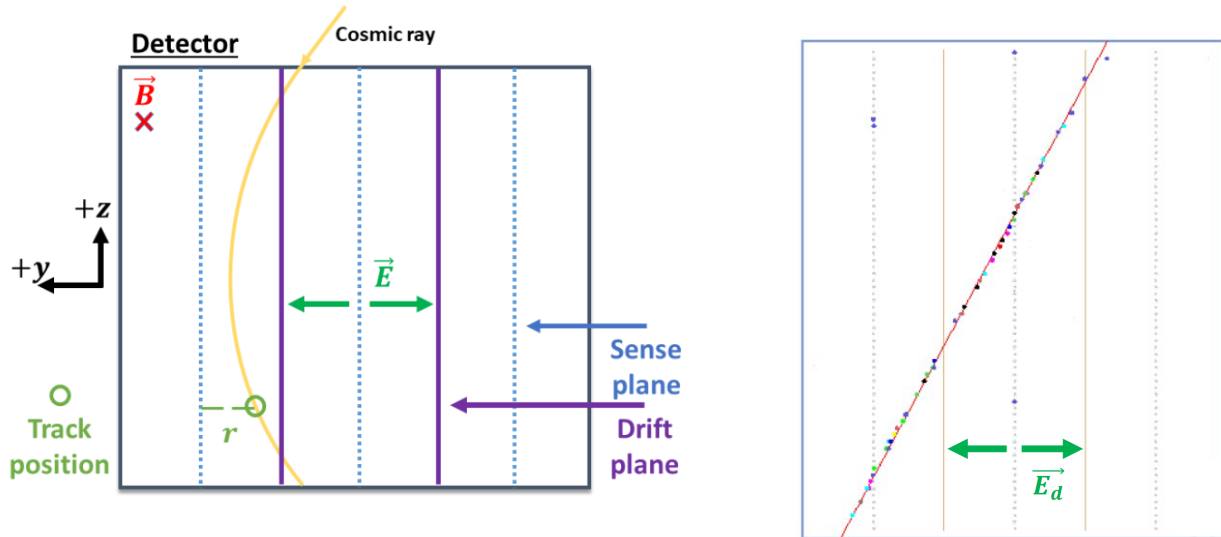
(a) A diagram showing how a track is reconstructed by the DCT. The impact parameter, r, is determined by the length of the induced pulse on the sense wire. Source: McBride [2021]

(b) A muon track reconstructed in the DCT. There is no deflection as the magnet was not on [McBride, 2022].

Figure 2.20: HELIX's Drift Chamber Tracker.

distance of the ionization from the wire. The current is integrated on each end of the sense wires to find the charge - since the resistivity of the wire and the impedance of the front-end electronics are known these two charge measurements can be used to determine where along the length of the wire the pulse originated [HELIX Collaboration, 2021, McBride, 2021]. A diagram of the DCT and an example of a reconstructed muon track are shown in Figure 2.20.

2.5   RICH

The Ring Imaging Cherenkov (RICH) detector is responsible for measuring the velocity of cosmic-ray particles at energies higher than what can be achieved with the ToF. It is the primary focus of my thesis project and so will be described in detail in chapter 3. Simply described, when a charged particle passes through a medium faster than the speed of light in that medium, the spherical wavefronts of electromagnetic radiation produced by the particle

Figure 2.21: The RICH during assembly [HELIX Collaboration, 2021].

constructively interfere at an angle θ relative to the path of the particle, as defined in equation 2.5. The RICH uses a measurement of this angle to determine particle velocity.

$$cos(\theta) = \frac{1}{n\beta} \tag{2.5}$$

Aerogel Radiator

HEILX's RICH contains two main components: a 600 × 600 mm radiator in which the Cherenkov light is produced, and a 1000 × 1000 mm focal plane where the Cherenkov light is detected. As shown in equation 2.5, the index of refraction n of the radiator must be known to find the velocity from a measurement of the Cherenkov angle. HELIX's radiator is made of 32 100 × 100 × 10 mm water-cut silica aerogel tiles produced at Chiba University with an index of refraction of $\sim$ 1.15 at 400 nm and 4 NaF tiles with an index of refraction of $\sim$ 1.33 at 400 nm [Tabata et al., 2020]. Upon delivery, collaborators at McGill University
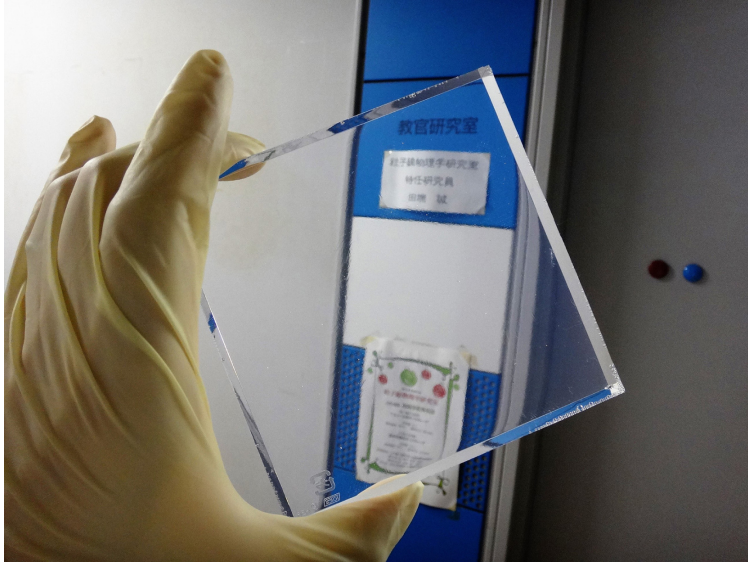
Figure 2.22: A HELIX aerogel tile, from Tabata et al. [2020].

led extensive studies into their properties, most notably measuring variations in thickness and index of refraction as a function of the position on each tile. One such method used to measure the refractive index of the tiles was to place the tiles in a 35 MeV electron beamline. The location of Cherenkov light produced in the tiles by the electrons was measured by linear charge-coupled devices (CCDs) placed in a circle centered on the axis of the beamline. The index was measured in a grid in steps of 5 mm in x and y by moving the tile's position in the beamline with a two-axis stepper motor controlled mount. This experimental setup is shown in Figure 2.23.
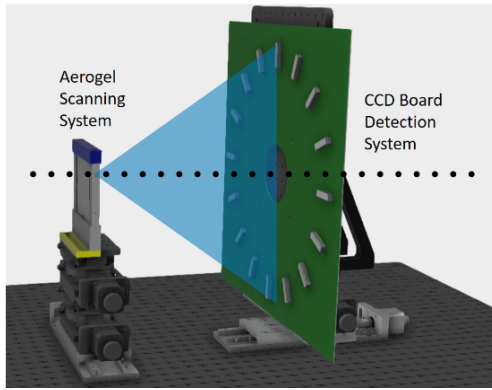
(a) A CAD file of the aerogel scanning system used at the Ionizing Radiation Standards department of the National Research Council in Ottawa [O'Brien, 2021].
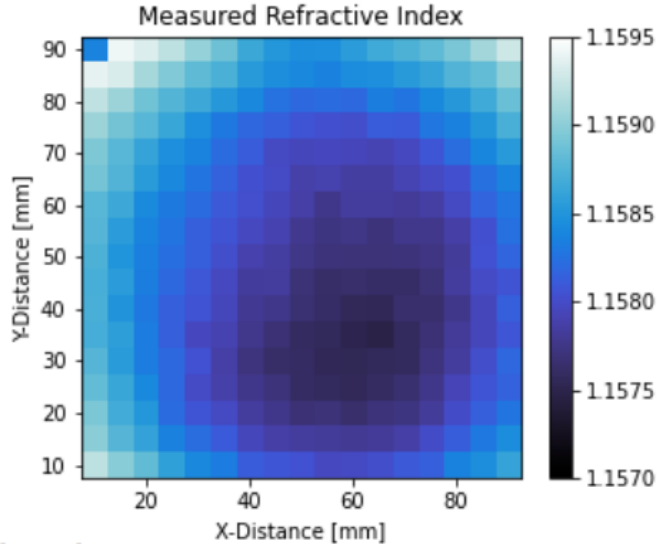
(b) Measurements of the index of refraction for one tile using an electron beam [O'Brien, 2021].

Figure 2.23: Method and results for measuring the aerogel index of refraction.

2.6 Hodoscope

During simulations of the full instrument, it was discovered that the DCT's position resolution in the plane parallel to the magnetic field, the "non-bending plane" of the instrument, was insufficient to reconstruct the particle's path through the aerogel precisely enough to reconstruct the Cherenkov cone with the resolution required. HELIX's hodoscope was designed to remedy this issue by providing an additional position measurement in the particle's non-bending plane immediately before entering the radiator. The hodoscope uses four glued scintillating fiber ribbons, each consisting of 150 1mm wide square fibers glued into a 600 mm long ribbon. These fibers then fan out from the ribbon and terminate in a delrin "cookie" which mates to the face of a Hamamatsu SiPM array. A top-down view of the hodoscope is shown in Figure 2.24. By detecting which fibers produce light via scintillation as the particle passes through, its position in one axis can be measured.

A more in depth discussion of my contributions to the development of the hodoscope is presented in section 3.4.

Figure 2.24: HELIX's hodoscope, removed from the payload [Jeon, 2022].

CHAPTER 3

THIS WORK

In this chapter, I will summarize the work I completed over the last six years in the course of this Ph.D. project. My work was on building, calibrating, integrating, and testing the RICH detector and related electronics, as well as developing simulation code capable of determining the science impact of the RICH.

3.1 Detector Simulation, Resolution Study, and Science Impact

Here I discuss the science that motivates the RICH detector, the simulation studies I conducted to ensure that the RICH detector is prepared to achieve the required isotope ratio resolution, and the resulting science impact of the RICH and RICH upgrades.

3.1.1 Velocity Resolution Studies

The primary focus of my graduate work has been to develop and construct a RICH detector capable of achieving HELIX's mass resolution goals. HELIX seeks a mass resolution of at least $\sim$0.25 amu to clearly resolve the ^{9}Be and ^{10}Be isotopes with a 4σ separation. This goal necessitates a $\frac{\delta m}{m} \sim 2.5\%$, shown in Figure 2.5b.

HELIX directly measures three properties of cosmic rays: their charge Z, their rigidity R, and their velocity β. Since rigidity is related to momentum by $R = \frac{p}{Ze}$, and momentum is related to mass by $m = \frac{p}{\beta\gamma}$, we can combine these three measurements to find the mass of the particle.

The mass resolution "budget" is split between two measurements: the measurement of the particle rigidity and the measurement of the particle velocity (charge is quantized and so does not contribute). The velocity resolution is particularly challenging as its contribution to the mass resolution is scaled by γ^4, where γ is the Lorentz factor of the particle, as shown

in Equation 3.1.

$$\left(\frac{\delta m}{m}\right)^2 = \left(\frac{\delta R}{R}\right)^2 + \gamma^4 \left(\frac{\delta \beta}{\beta}\right)^2 \tag{3.1}$$

HELIX is designed as a two stage experiment: stage 1 targets energies up to 3 GeV/n, and stage 2 will upgrade the existing detector infrastructure to reach up to 10 GeV/n/. HELIX's Time of Flight system provides a velocity measurement up to $\sim$ 1 GeV/n, above which its resolution is insufficient. For energies above 1 GeV/n, a different detector is needed. The detector chosen to make this measurement not only needs to be able to reach its resolution goal up to energies of 3 GeV/n for HELIX's stage one flights, but also critically needs to support upgrades to extend this energy range to 10 GeV/n for HELIX stage 2 flights. Since flight durations are limited and particle flux decreases at higher energies, limits on the instrument's acceptance should be minimized as well.

It was determined that a RICH detector would be best suited to meet HELIX's velocity resolution needs at higher energies. However, it is important to contextualize this choice of detector against the weaknesses of similar, simpler, but ultimately lacking alternatives. Here I will the impact of the RICH detector on the scientific goals of HELIX against its most likely alternative, an integrating Cherenkov counter. I developed the following models in Python, largely from first principles of Cherenkov detectors as described in Ypsilantis and Séguinot [1994].

Integrating Cherenkov Counter

The first detector design considered for these high energy β measurements was an integrating Cherenkov counter, sometimes referred to as a "threshold Cherenkov" detector. These counters use the quantity of Chernkov light produced in a radiator by a particle . The amount of light produced by the particle is related to the velocity by the Frank-Tamm formula [Frank and Tamm, 1937, Čerenkov, 1937]. The number of photons emitted per unit length in a

radiator is given by equation 3.2 [Ypsilantis and Séguinot, 1994].

$$\frac{\mathrm{d}N_{ph}}{\mathrm{d}E} = (\frac{\alpha}{\hbar c})Z^2 L \left[1 - \left(\frac{1}{n\beta} \right)^2 \right] \tag{3.2}$$

With some simple assumptions about the spectral range of detected photons, this can be solved for β to find equation 3.3, where L is the path-length the particle travels through the detector.

$$\beta \approx \frac{1}{n} \sqrt{\frac{1}{1 - \frac{N_{ph}}{370 L Z^2}}} \tag{3.3}$$
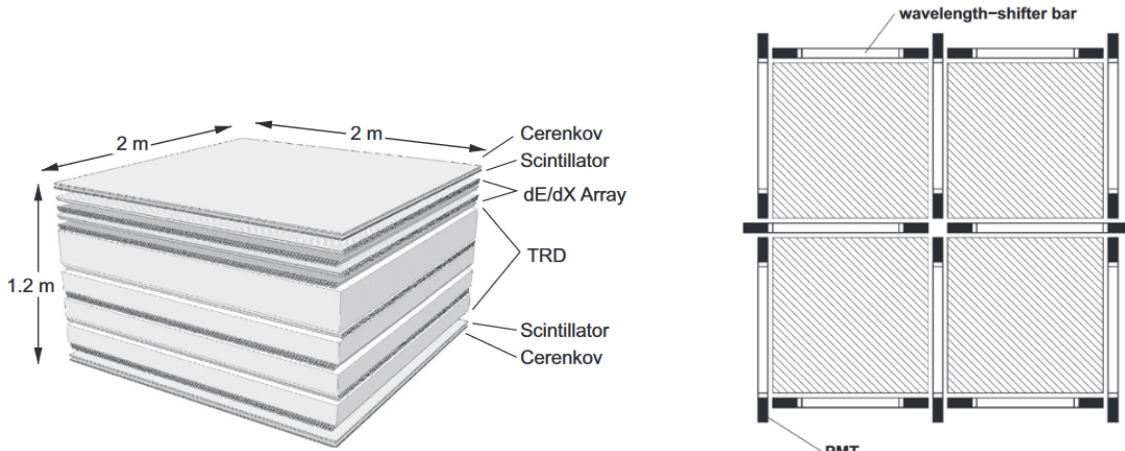
(a) A schematic of the TRACER instrument.

(b) A schematic of TRACER's Cherenkov counters with Polycast Acrylic radiators. Cherenkov light is read out by PMTs attached to wavelength-shifting bars.

Figure 3.1: TRACER schematics from Ave et al. [2011].

TRACER is an example of a balloon experiment which successfully implemented an integrating Cherenkov detector in a ballooning environment, and in fact has an overlap in personnel with HELIX. [Ave et al., 2011]. A schematic of the TRACER instrument is shown in Figure 3.1a, and a schematic of its Cherenkov counters is shown in Figure 3.1b. Unlike HELIX, however, TRACER did not attempt to measure isotopic composition of the cosmic

ray flux, and so did not require the same β resolution as HELIX.
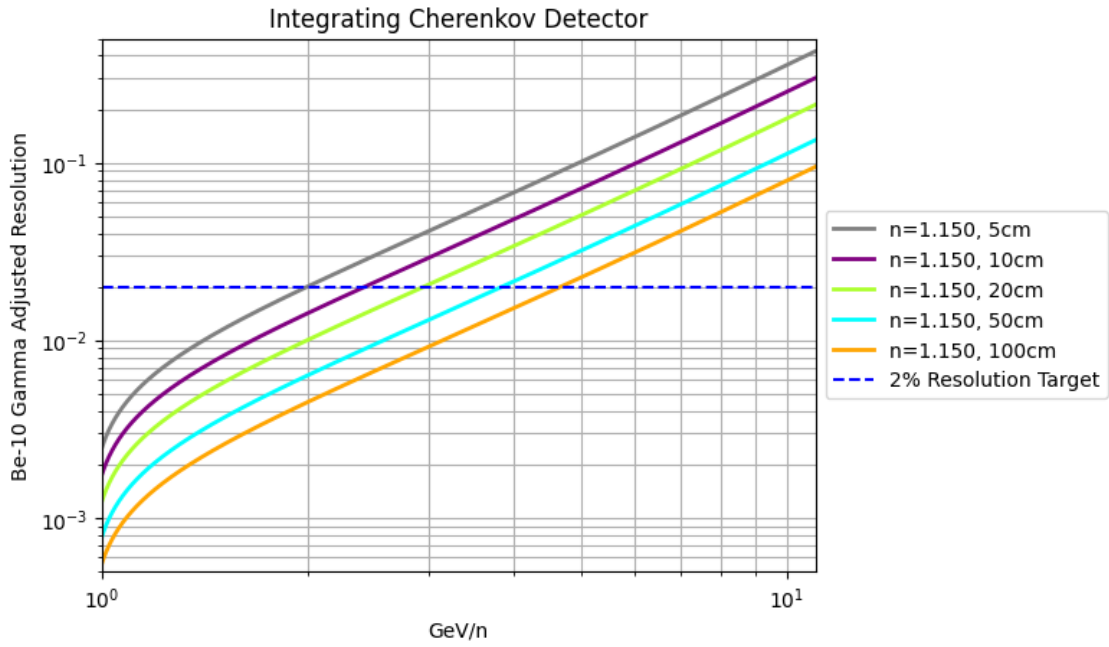
Figure 3.2: Mass resolution contribution of integrating counters of different thicknesses.
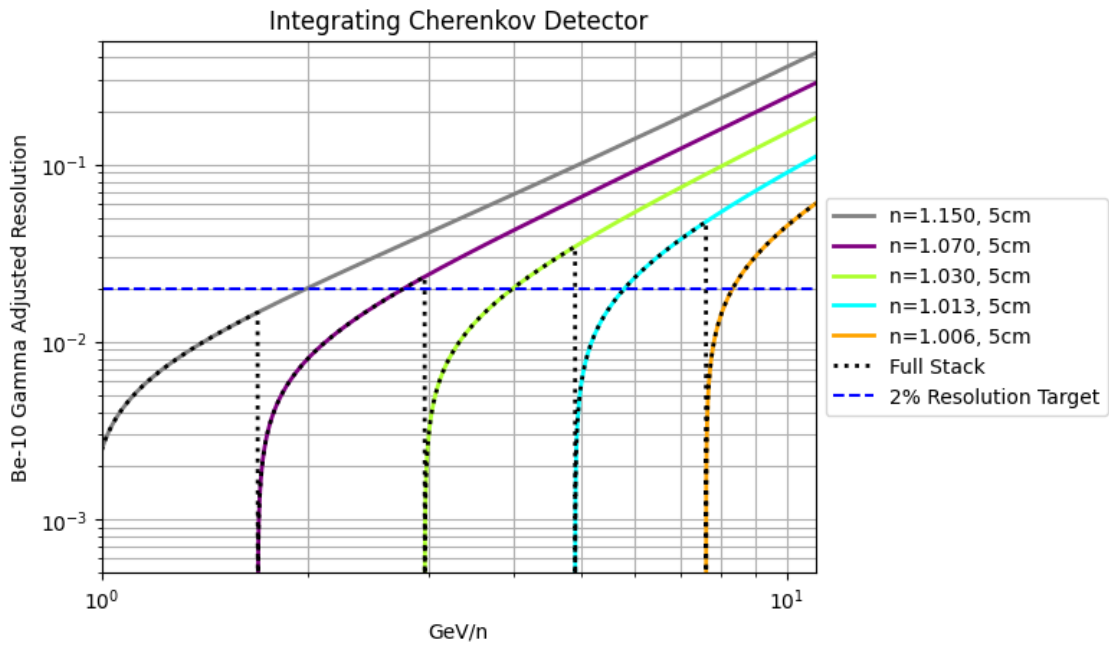
Figure 3.3: Mass resolution contribution of integrating counters of different indicies of refraction. The dotted line shows the combined resolution achievable if these detectors were stacked.
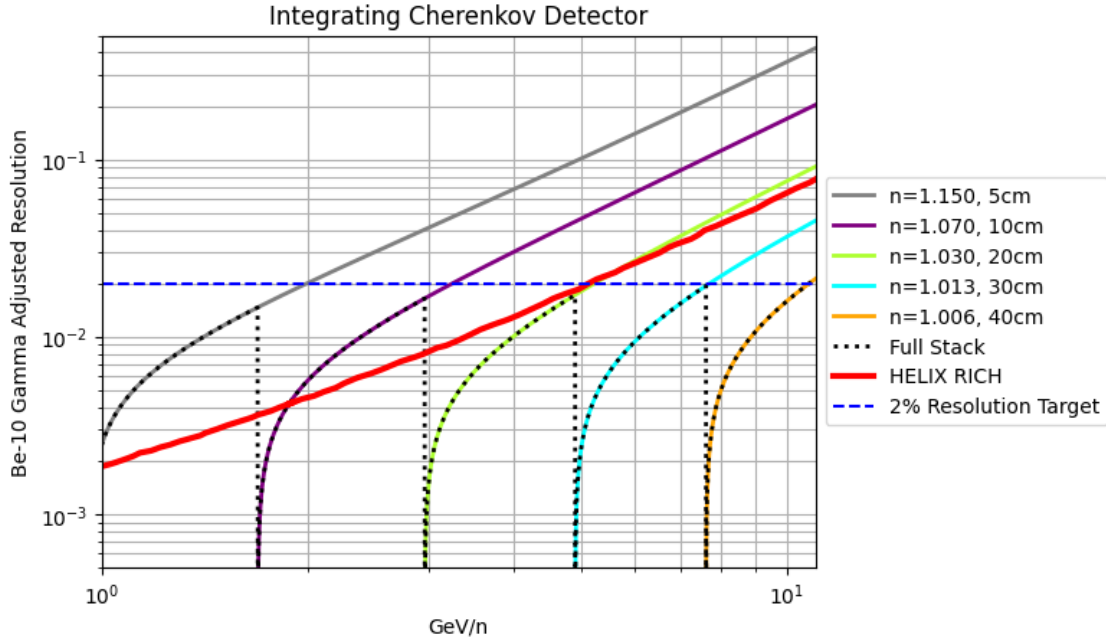
Figure 3.4: Simulation results showing integrating Cherenkov detectors' mass resolution contributions. The dotted line shows the combined resolution achievable if these integrating detectors were stacked. Plotted in red is a simulation of HELIX's stage 1 RICH mass resolution contribution.

To illustrate why a different instrument is needed, I calculated the resolution achieved by an integrating Cherenkov detector designed to meet the required specifications of HELIX in the targeted energy range of 1-10 GeV/n. A particle begins emitting light once it has kinetic energy such that it is above the Cherenkov velocity threshold; this is the turn-on energy of the detector. However, the mass resolution contribution of the detector quickly degrades as the kinetic energy of the particle increases. One method of combating this resolution degradation is to increase the thickness of the detector, which in turn improves the light yield and therefore resolution. I built a model of these effects in Python, the results of which are shown in Figure 3.2. A second method is to stack detectors of different indicies of refraction such that when the energy is high enough that one section no longer meets the resolution requirements, a new section with a lower index of refraction begins operating. This second method was similarly modeled and the results are shown in Figure 3.3.

One can attempt to minimize the complexity and size of the detector by combining these two methods. I modeled one such configuration with the results shown in Figure 3.4. Although only the first two layers would be needed for the stage 1 instrument, upgrading the detector for stage 2 would require all five layers. This detector configuration would be bulky, requiring a total instrumented thickness of 1.05 m and well over 0.36 m^3 of aerogel, and complex, with five separate instrumented layers. It would also restrict the total acceptance of the instrument, reducing the statistics achievable in an already light flux.
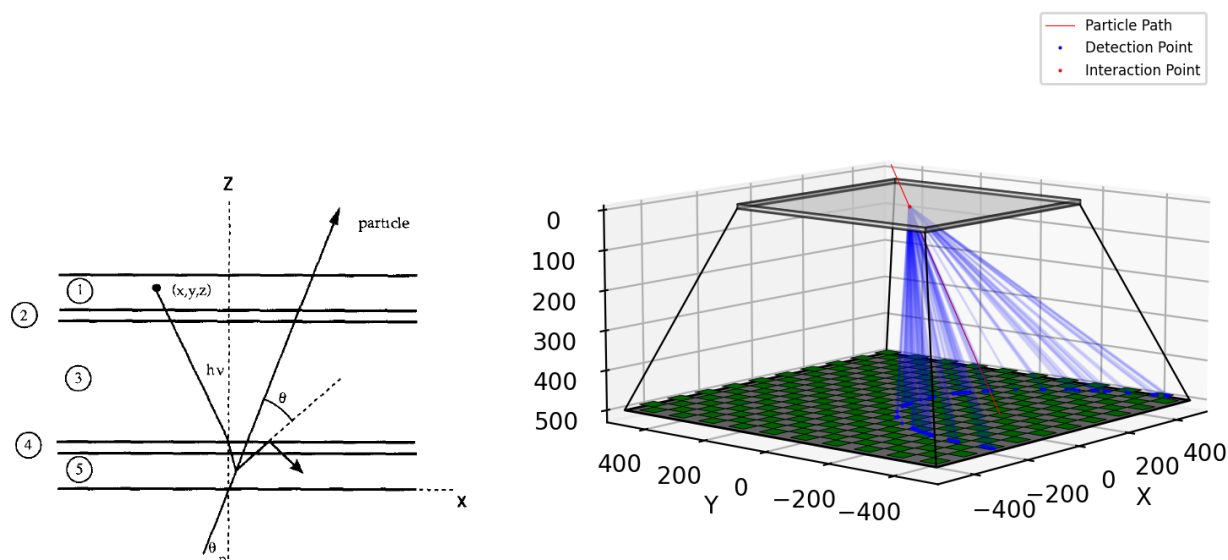
(a) Geometry of a proximity focused RICH from [Ypsilantis and Séguinot, 1994]. (1) is the detector medium, (2) and (4) are the window media if present, (3) is the lever-arm medium, and (5) is the radiator medium.

(b) A rendering from my simulation of HELIX's RICH in operation, for a ^{9}Be nucleus at 3 GeV/n. With a proximity focused RICH, the light forms a deformed conic section on the focal plane.

Figure 3.5: Proximity focused RICH.

Ring Imaging Cherenkov Detector

With integrating Cherenkov detectors appearing insufficient for HELIX's needs, the next logical detector to consider is a Ring Imaging Cherenkov Detector, or RICH. RICH detectors
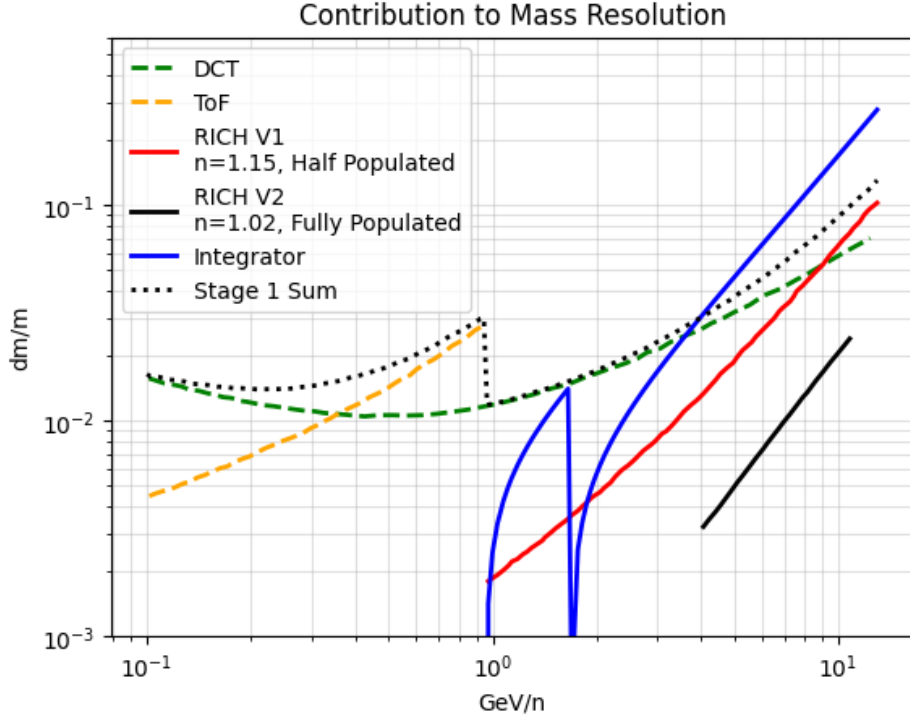
Figure 3.6: Contributions of various subsystems to HELIX's total mass resolution. The ToF is shown in yellow, and the DCT is shown green. In blue is a two layer Cherenkov integrator, chosen to cover HELIX's stage 1 range of up to 3 GeV/n. In red is HELIX's stage 1 RICH, and in black is the same RICH, upgraded for stage 2 with a lower index of refraction radiator and fully populated focal plane. The total mass resolution for HELIX stage 1 is also shown.

use the angle of Cherenkov light emission, rather than the quantity of light, to measure a particle's velocity. This emission angle is given by the relation in equation 2.5.

There are multiple ways to make a RICH detector, often employing spherical mirrors and spherical detector planes to focus the Cherenkov light emitted from the particles into one easy to measure ring. Since HELIX does not have the benefit of fitting its detector into a stationary, controlled environment such as those available to accelerator based experiments, we have opted instead for a proximity focused RICH detector. A proximity focused radiator is much simpler to construct as it requires no optical focusing elements. Instead, it requires a thin radiator producing a cone of finite width and a long spatial lever arm to allow the cone to expand. Because the particles are not guaranteed to enter the detector perpendicular to

the focal plane and radiator, the Chernekov light will form a conic section on the detector rather than a symmetric ring. In fact, the conic section will be deformed through refraction effects as the light passes between media [Ypsilantis and Séguinot, 1994]. The geometry of a proximity focused RICH detector is shown in Figure 3.5a, and a rendering of HELIX's RICH in use with the Cherenkov light from 3 Gev/n kinetic energy ^{9}Be particle is shown in Figure 3.5b.

The benefit of a building a RICH detector is demonstrated in Figure 3.6. HELIX's stage 1 flight will have its mass resolution dominated by the DCT performance to about 5 GeV/n, so the stage 1 RICH design is optimized for the 1-5 GeV/n energy range, using only a half populated focal plane to save costs. In HELIX's stage 2, upgrades to HELIX's rigidity measurement subsystem to support energy ranges up to 10 GeV/n will necessitate similar upgrades to the velocity measurement subsystem to extend its required performance to these energies as well. For an integrating Cherenkov detector, this would require significantly more instrumented volume, in addition to greatly increased complexity with the addition of more layers. However, as show by my simulation results in Figure 3.6, simply changing the radiator's index of refraction and fully populating the focal plane allows the RICH to reach up to 10 GeV/n and beyond. Although not examined in this analysis, it is very much a possibility to stack two layers of RICH radiators with different indicies of refraction to cover both the higher energies optimized for in the second RICH design and the energies below its cutoff accessible to the first design.

Effect of Velocity Resolution on Final Science Results

It's important to put the value of improving the velocity resolution into the proper context. Here, I will demonstrate the effect of developing a high quality detector on HELIX's premier measurement, the ^{10}Be/^{9}Be isotope ratio. I calculated the attainable uncertainty of each HELIX configuration with a toy Monte Carlo, generating distributions of beryllium mass
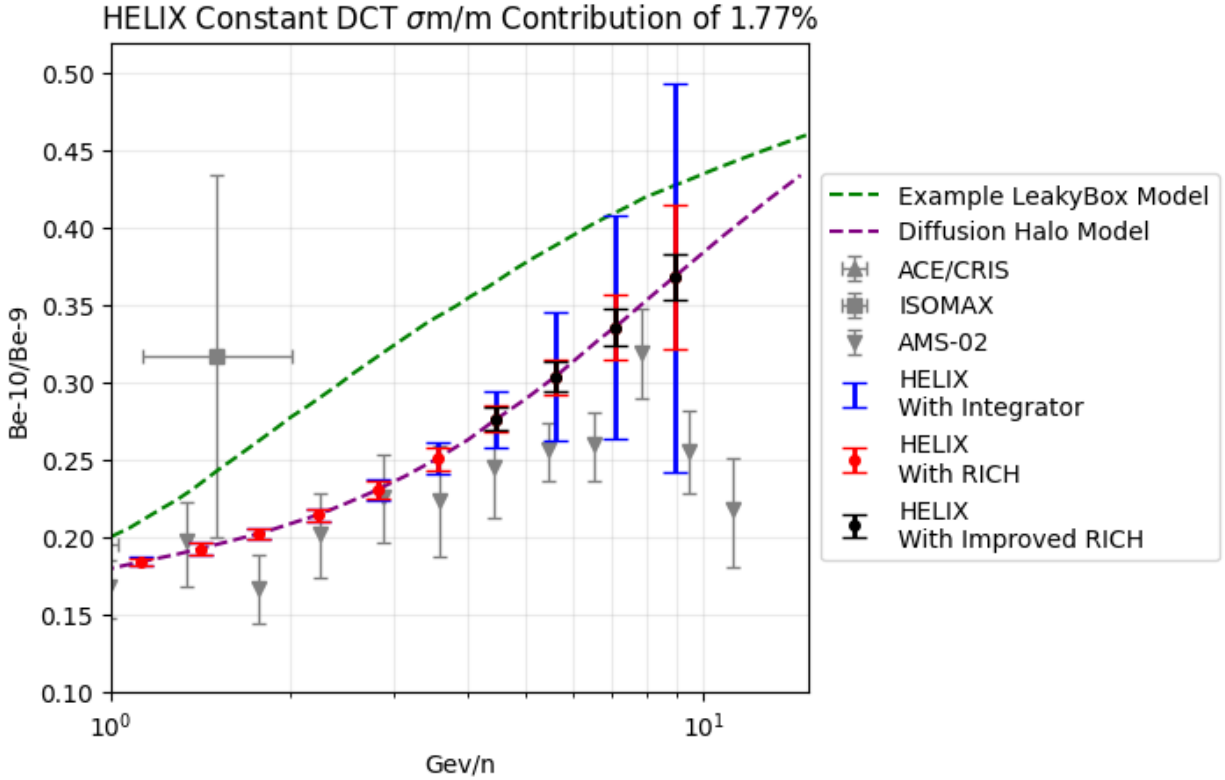
Figure 3.7: Beryllium isotope ratios measurements from 1 to 10 GeV/n. Shown in grey are the reported measurements of other experiments [Derome, 2021, Hams et al., 2004a]. In green and purple are the predicted ratios from two (of many) possible models of cosmic ray propagation [Raisbeck and Yiou, 1971, Webber et al., 1990]. HELIX's simulated uncertainty is plotted along the path of the example diffusion halo model. In blue is the resolution with a two layer Cherenkov counter. In red is the resolution with HELIX's current (stage 1) RICH configuration. In black is the same RICH, with minor upgrades for stage 2. In all cases, the rigidity component of mass resolution of HELIX was assumed to be a constant 1.77% to more clearly demonstrate the differences between different velocity subsystems.

measurements considering both the number of expected events in the energy bin for a flight with ten days of livetime and the resolution of the velocity measurement at that energy. The resulting data are then fit, allowing the relative heights of the two isotopes and the detector resolution to vary. The distribution of resulting ratios from fits of these trials are used to estimate the uncertainty in the isotope fraction measurement. In Figure 3.7, the effect my simulations of the resolution of three possible velocity subsystem have on the beryllium isotope ratio are demonstrated. The ability of a RICH detector to scale to higher energies
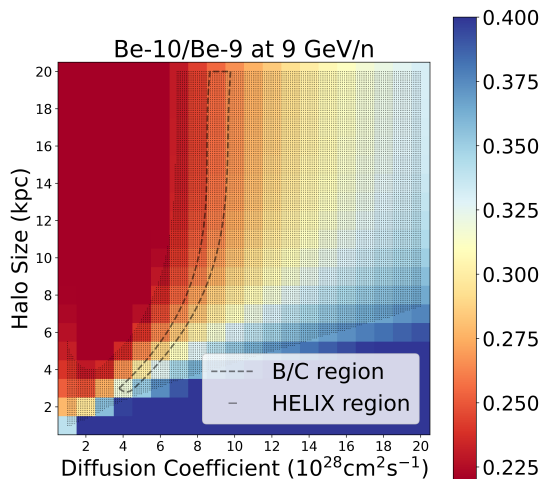
Figure 3.8: GALPROP predictions of the ^{10}Be/^{9}Be ratio, at a kinetic energy of 2 GeV/n, for a range of 20 values each of halo size L and diffusion coefficient D. A hypothetical measurement of 0.30 has been chosen for the beryllium ratio, for illustrative purposes. The two bands shown are a 95% confidence interval set based on AMS-02 measurements of B/C, and a 1σ band for a Be isotope ratio as measured by HELIX, using an integrating Cherenkov detector and a DCT with hypothetical mass resolution contribution of 1.77%. GALPROP models and some plotting code courtesy of Dr. Keith McBride (McBride [2021]).

makes it the ideal detector for HELIX to implement.

To further examine the value of a well designed RICH, plots of GALPROP predictions for the beryllium isotope ratio and the ability of HELIX to reject models in this phase space, similar to that shown in section 2.1 are shown in Figures 3.8, 3.9a, 3.9b. Notice that while the stage 1 integrator design does not reduce the parameter space, the stage 1 RICH reduces it by a factor of $\sim$5 and the stage 2 RICH reduces it by a factor of $\sim$20.

3.1.2 HELIX RICH Simulation

My simulations of HELIX's RICH were developed from the principles outlined in Ypsilantis and Séguinot [1994]. The input parameters were the incoming particle energy, angle of incidence, location of impact, and the noise distribution of the SiPM channels. An example
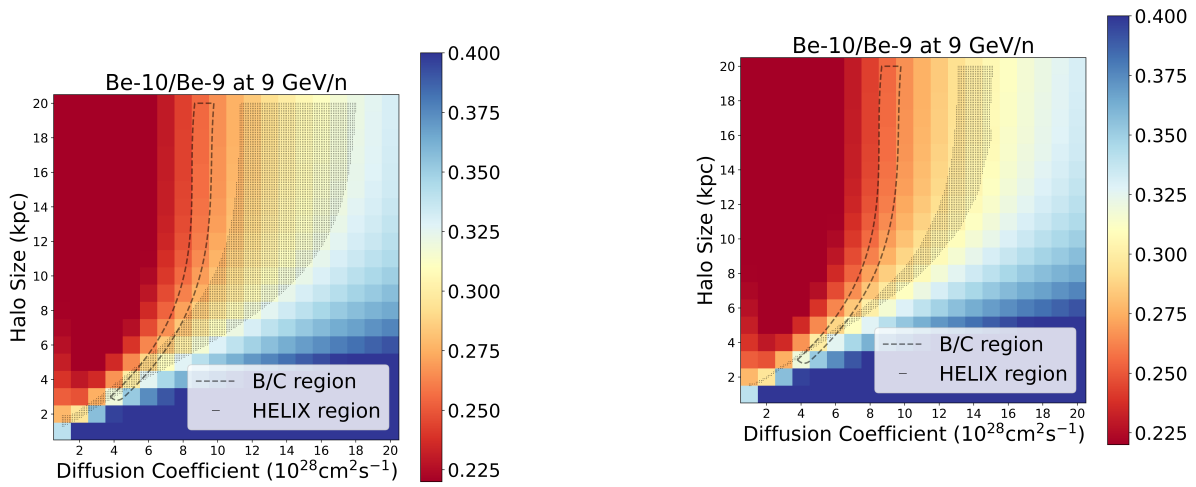
(a) Same as Figure 3.8,but now with a stage 1 HELIX RICH design using a half populated focal plane and a radiator with n=1.15 instead of an integrating Cherenkov Detector.

(b) Same as Figure 3.8, but now with a stage 2 HELIX RICH design using a fully populated focal plane and a radiator with n=1.02 instead of an integrating Cherenkov Detector.

Figure 3.9: Halo size and diffusion coefficient parameter space restriction using RICH detectors.

of the noise distribution is shown in Figure 3.10. Once the event is simulated a map of the focal plane's readings is produced, shown in Figure 3.11. From there, knowledge of the particles path provided by other detectors (in HELIX's case, the DCT) can be used with the location of hits on the focal plane to calculate the particles velocity. A histogram of per-detected photon β values can then be produced from the event data. If the signal is of significant magnitude a spike at the correct β value should rise above the otherwise randomly distributed noise. This is shown in Figure 3.12.
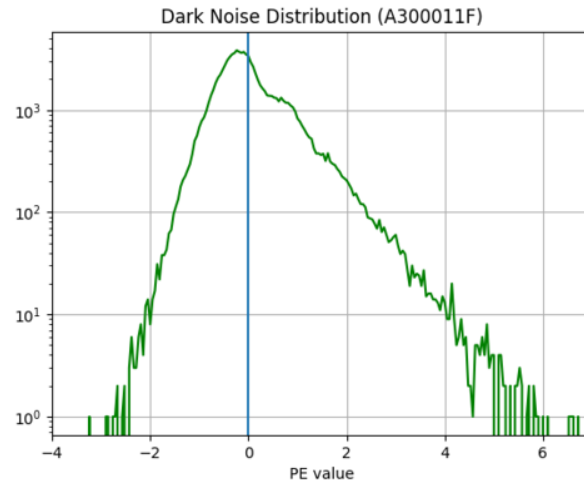
Figure 3.10: Dark noise PDF for a SiPM at lab temperatures.
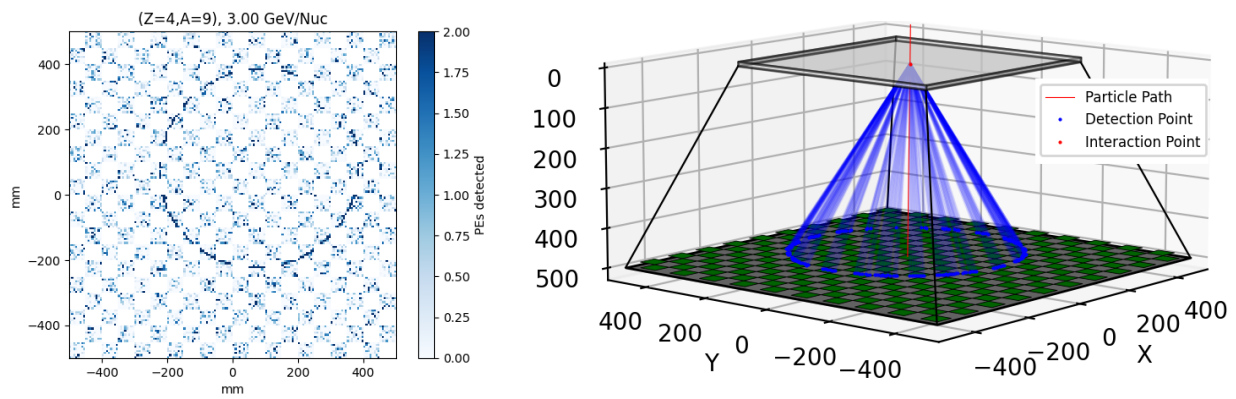
Figure 3.11: A single 3 GeV/n ^{9}Be event.
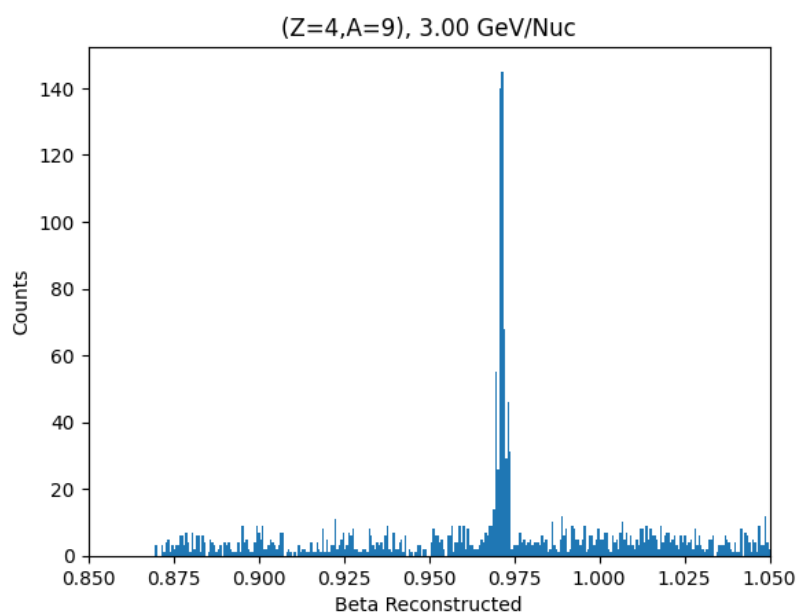
Figure 3.12: The histogram of per-PE signal calculated β values. The data in this histogram is from the same simulated event shown in Figure 3.11.

3.2 Silicon Photomultipliers (SiPMs) - A Background

The core of this thesis project is the development of HELIX's focal plane, which is instrumented with Silicon Photomultipliers (SiPMs). SiPMs, sometimes referred to as solid state photomultipliers or Multi-Pixel Photon Counters (MPPCs), were first proposed in the 1980s, with the first prototypes appearing for use in the early 2000s. In the years since SiPMs development has flourished, leading to their use in a variety of applications. Their advantages over traditional photomultiplier tubes (PMTs) include but are not limited to their small size, insensitivity to magnetic fields, operating voltages below 100V, and mechanical ruggedness (Otte [2016]).

3.2.1 SiPM Building Blocks

In a simplified view, the most basic building blocks of SiPMs are junctions between two doped regions of semiconductor material called PN junctions. Silicon PN junctions are formed by doping one section of crystalline silicon with an electron donor and an adjacent portion of the silicon with an electron acceptor. This creates an N region where electrons are the majority charge carrier and a P region where holes are the majority charge carrier. A diffusion of charge carriers from each side then occurs, allowing the electrons and holes to recombine in the area around the junction, forming a "depletion layer". The loss of these carriers from each of the doped regions results in a charge excess - positive on the N side where electrons have been lost to recombination, and negative on the P side. This charge difference causes an electric field to form across the junction, pointing from the N side to the P side. The process of diffusion continues until the electric field's strength has grown enough to halt it and equilibrium is reached (Ghassemi et al. [2017]). A simplified diagram of this final state is shown in Figure 3.13.

If enough energy is provided to an electron in the depletion region of the junction, it can make the transition from the valence band that to the conduction band resulting electron-hole
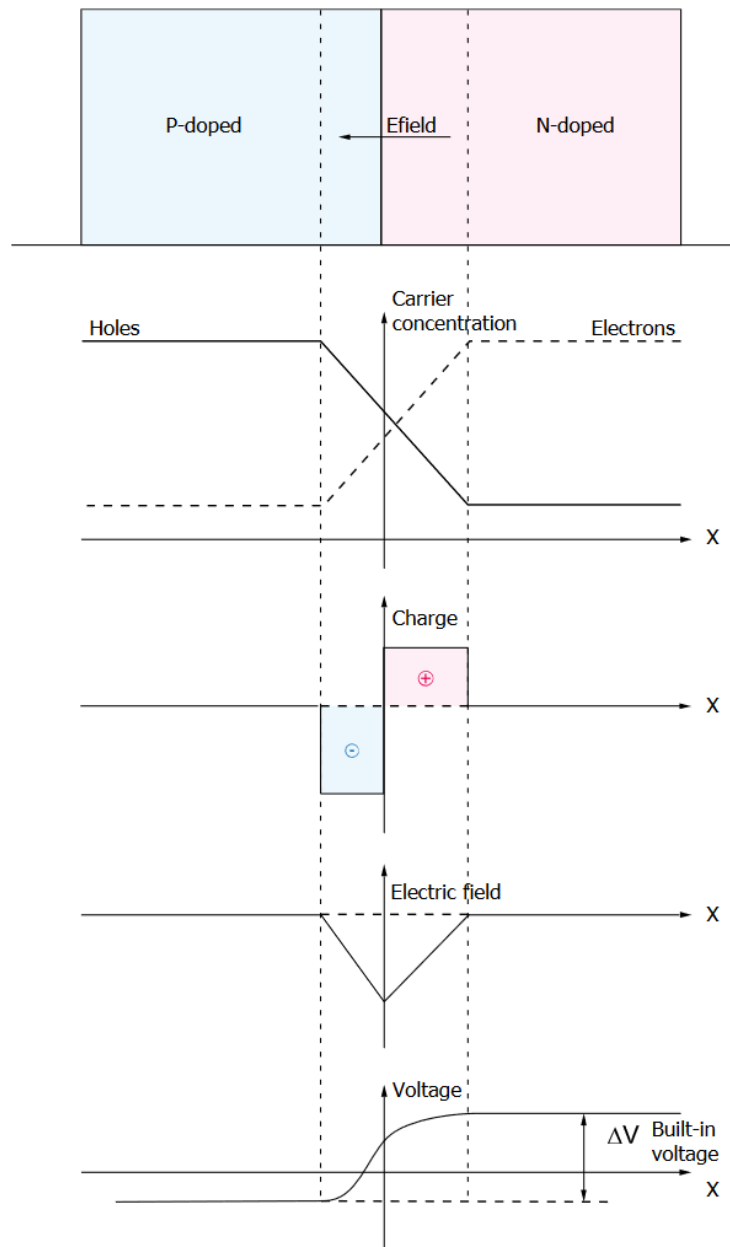
Figure 3.13: A PN junction in equilibrium. Source: Ghassemi et al. [2017].

pair. The energy to excite the electron may be from thermal excitations or from photoelectric effect. These two excess charge carriers are then accelerated by the electric field present in the depletion region. The depletion layer's depth can be increased by applying a reverse bias across the junction, where the anode (P side) is held at a lower voltage than the cathode

(N side). A diagram of this avalanche region forming in the depletion region of an APD is shown in 3.14
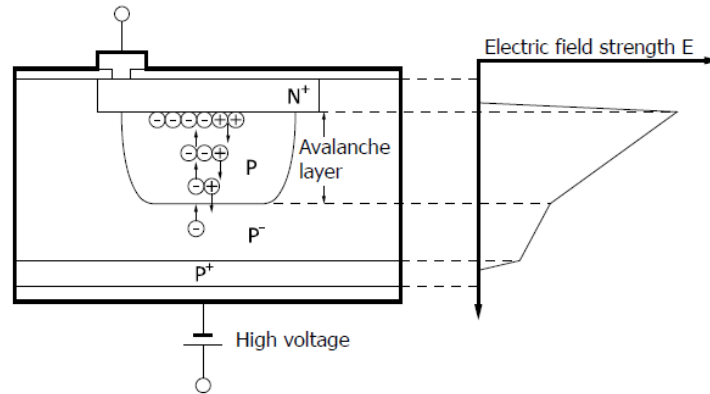
Figure 3.14: An avalanche region formed in the depletion region of an APD. Source: Ghassemi et al. [2017].

If the reverse voltage across the junction is large enough, the larger resulting electric field can cause electron-hole pairs traveling across the junction to impart enough energy in scattering collisions with atoms in the crystals lattice to liberate additional electron-hole pairs. The cascade of carriers that results is called an avalanche which gives rise to the name of this device, and Avalanche Photodiode (APD). Rather than the gain of 1 that would occur without an avalanche, APDs have the ability to magnify the original signal prior to readout. However, the gain of APDs operated in this mode fluctuates due to randomness in the collision process in addition to having dependencies on temperature, incident light wavelength (due to penetration depth in the detector), and bias voltage.

If the reverse bias is increased to the point where charge carriers are created in the depletion region at a rate exceeding the rate at which they leave the region. The voltage at which this first occurs is referred to as the breakdown voltage, or V_{bd}. An APD operating above breakdown is said to be operating in Geiger-mode, and may be referred to as a Geiger-mode APD (GAPD). The gain for a GAPD is shown in Equation 3.4, where C_j is the junction capacitance.

54

$$G = \frac{C_j \times (V_{bias} - V_{bd})}{e} \qquad (3.4)$$

During a GAPD avalanche, the current grows until the total voltage across the avalanching region matches the breakdown voltage, at which point without some form of quenching the current would continue indefinitely. A quenching resistor is placed after the GAPD to limit how long this current persists. An equivalent circuit for a GAPD with a quenching resistor is shown in Figure 3.15. When the first electron-hole pair is produced in the depletion region, the switch is closed and C_d begins to discharge across the the series resistance of the GAPD R_s in the left-hand loop. As C_d discharges, a current from V_bias flowing through the right-hand loop begins recharging it. If the quenching resistor R_q is selected such that the recharging current is unable to keep up with the discharging current, voltage across C_d will drop close enough to a device where breakdown voltage V_{bd} that the current from the capacitor discharge across the switch will cease, stopping the avalanche and opening the conceptual switch. Once again open, the capacitor recharges back to V_{bias} and the system had returned to its initial state. (Ghassemi et al. [2017]).

3.2.2   SiPM Basics

The GAPD is ideal for detecting single photons, but its digital rather than linear response to light and the existence of a recovery time while the capacitance recharges limit its uses. However, both these concerns can be addressed by combining many GAPDs (including their quenching resistors) in parallel, sharing a common cathode and anode and reading out as one channel. This configuration, shown in Figure 3.16, is a SiPM. Since each APD operates independently, the output of each SiPM is essentially the linear sum of the APD signals. If the photon flux is small enough that the odds of hitting any individual APD with more than on photon during an event is low, the output will directly correspond to the number of photoelectrons produced in the much larger SiPM.
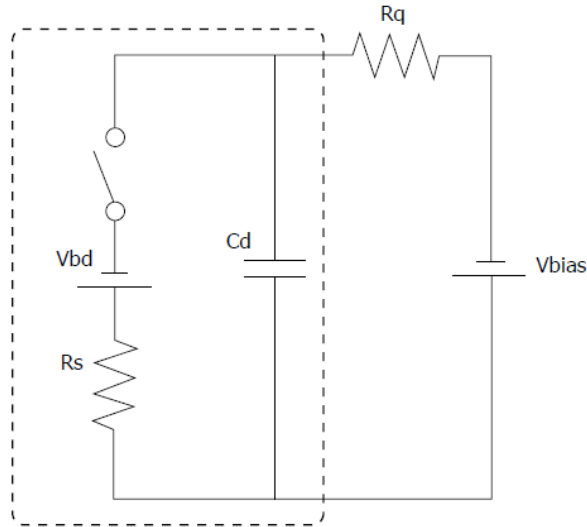
Figure 3.15: An equivalent circuit for a GAPD. The switch is conceptual; it is closed when the first election-hole pair is formed and opened. The dotted region shows the bounds of the GAPD. Source: Ghassemi et al. [2017].
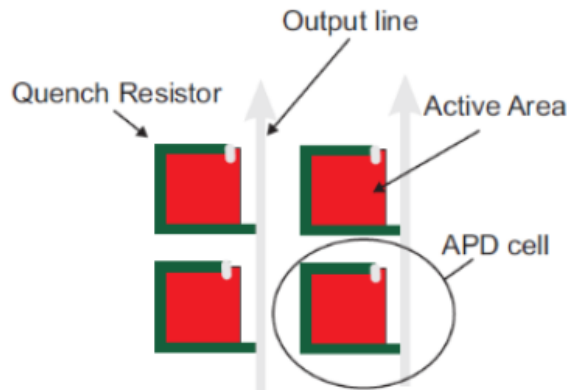
Figure 3.16: A sketch of APD cells connected in parallel in a SiPM. Source: Otte [2016].

There are many parameters used to characterize the performance of SiPMs, including photodetection efficiency, optical crosstalk between APDs, dark count rate, gain, and after-pulsing. These parameters may exhibit dependence on the operating conditions of the SiPM. Two of the most notable operating conditions are the voltage the SiPM is biased above its breakdown voltage called *overvoltage*, and the temperature of the SiPM. These factors will

56

be discussed in the "SiPM Initial Characterization" subsection,but are defined briefly below.

Photodetection Efficiency (PDE)

The probability with which an incident photon results in a signal. It has a frequency dependence.

Gain

The proportion of output charge in response to one photoelectron.

Dark Count Rate

The frequency at which signals are produced without any incident light.

Optical Crosstalk

The crosstalk between APDs within a SiPM due to IR photons created during an avalanche triggering a nearby APD.

Afterpulses

When carriers, trapped in impurities in the APD, are later released and cause a delayed signal after the initial pulse.
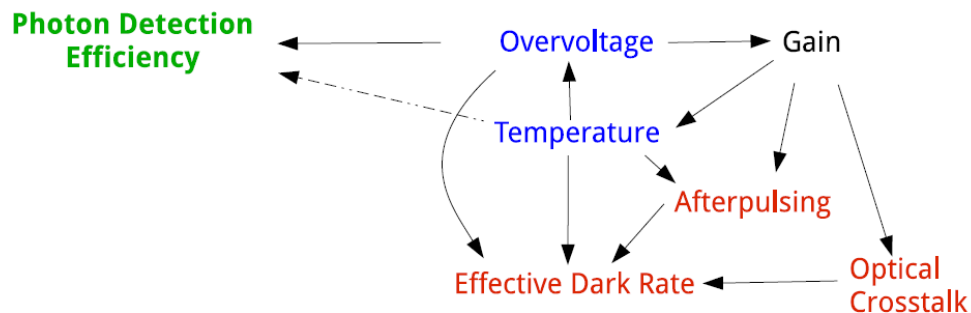
Figure 3.17: Inter-dependencies of SiPM parameters and operating conditions. In blue are the directly controllable conditions, in green are positive parameters, in red the nuisance parameters, and in black are situationally dependent parameters. Source: Otte [2016].

The first controllable parameter, overvoltage, plays a role in determining nearly all of the parameters of SiPM performance. In theory, as the voltage is increased further above

breakdown the gain of the SiPM increases linearly. There are also positive correlations between overvoltage and dark count rate, PDE, afterpulsing, and optical crosstalk. The second controllable parameter, temperature, plays a direct role in some of these parameters and in indirect role in all. The SiPMs PDE is a function of its quantum efficiency, the fraction of photons incident onto the photosensitive area which produce a photoelectron. As the temperature increases, the quantum efficiency increases due to an increase in phonon vibrations that may assist an electron-hole pair in forming. However, the avalanche probability from these electron-hole pairs decreases with temperature, leading to a PDE with nonlinear temperature dependence (Ghassemi et al. [2017]). Afterpulsing has also been demonstrated to have a temperature dependence, although not necessarily a straightforward one (Piatek [2017]).

The indirect dependence on temperature that many SiPM parameters experience is due to the temperature dependence of the breakdown voltage. As temperature increases the breakdown voltage rises, which for a constant bias shrinks the overvoltage value. This in turn changes the parameters that depend on overvoltage, as described above. It is worth noting here that although temperature is technically a controllable parameter, in practice many experiments exist in environments where temperatures cannot be kept absolutely stable. This is particularly true in the case of balloon experiments like HELIX, leading to a significant need to both understand the effect of temperature and adjust bias voltages to keep overvoltage constant in the presence of temperature shifts.

3.2.3   Hamamatsu S14498 SiPM Arrays

HELIX's focal plane is instrumented with Hamamatsu S14498 SiPM arrays, shown in Figure 3.18. These arrays have 64 SiPMs set in an 8x8 grid. Each channel has a photosensitive area of 6.0×6.0 mm, with a pitch of 6.2×6.2 mm. Each SiPM contains 6336 APDs with an individual pitch of 75 µm. All the channels within each array share a cathode connection
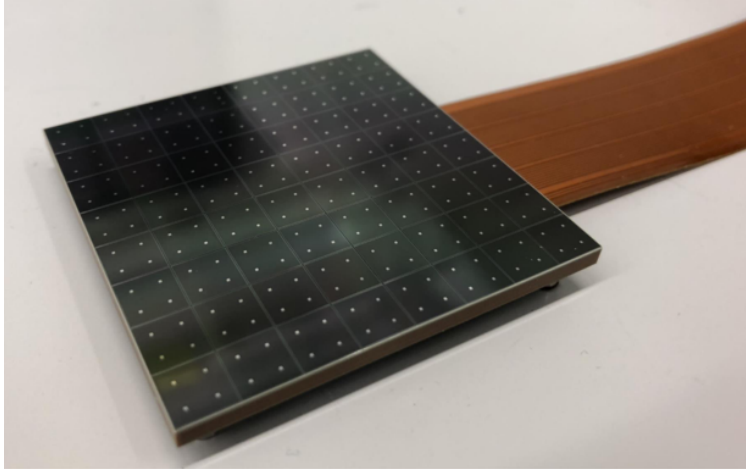
Figure 3.18: An 8x8 array of SiPMs, as used in HELIX's focal plane.

and are read out individually from their anodes. A schematic of HELIX's SiPM arrays is shown in Figure 3.19, and plots of their performance parameters as reported by Hamamatsu's S14498 datasheet are shown in Figures 3.21 and 3.22.
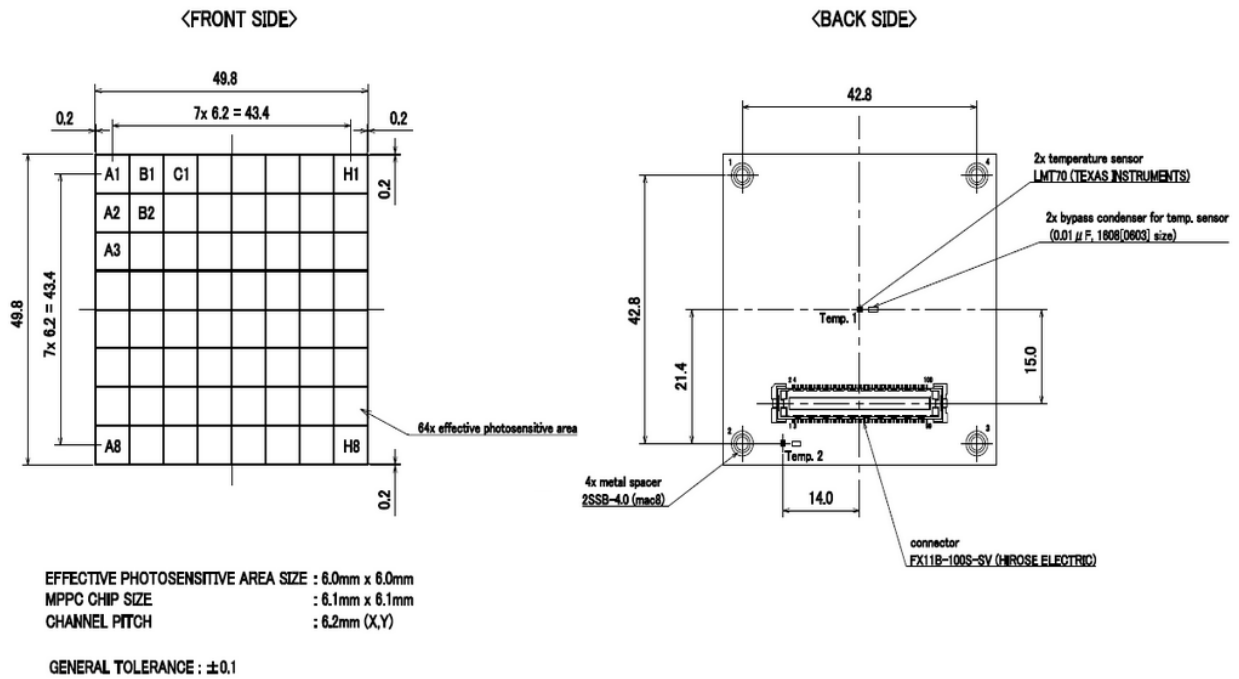
Figure 3.19: Schematic of Hamamatsu's 8x8 S14498 SiPM Array. From Ham [2018].

As seen in Figure 3.19, the back side of each array has a FX11B-100S-SV connector with
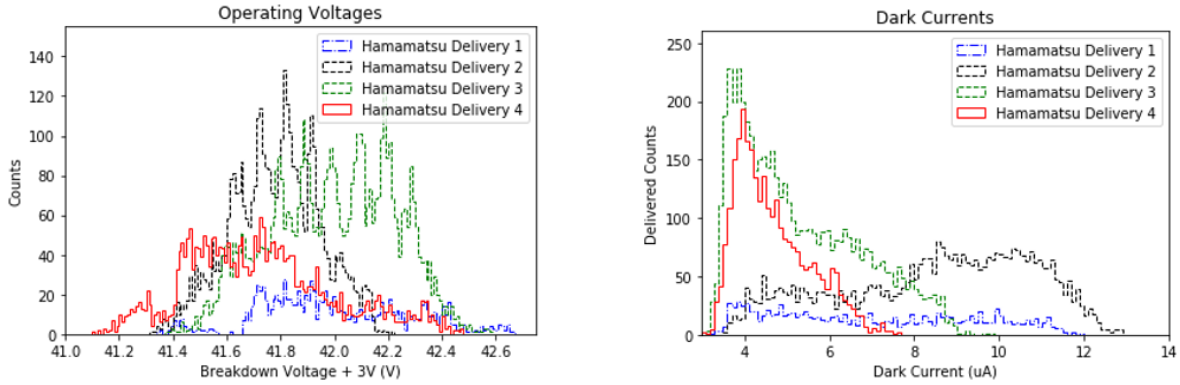
(a) The operating voltages of each SiPM. Operating voltage is 3V above the breakdown voltage.

(b) The dark current of each SiPM when at operating voltage.

Figure 3.20: Hamamatsu reported SiPM properties.

100 pins, four 4 mm standoffs with tapped holes for mounting, and two Texas Instruments LMT70 temperature sensor for monitoring thermal changes in the arrays. The connectors service 64 connections for the SiPM anodes, 32 connections for the shared cathode connection, and 4 lines for the temperature sensors.

Hamamatsu reported the operating voltages and dark currents for each channel on all the delivered arrays. These data are show in in Figure 3.20.

Figure 3.21: Photon Detection Efficiency vs Wavelength of the S14498's. HELIX uses the resin-type SiPM. From Ham [2018].
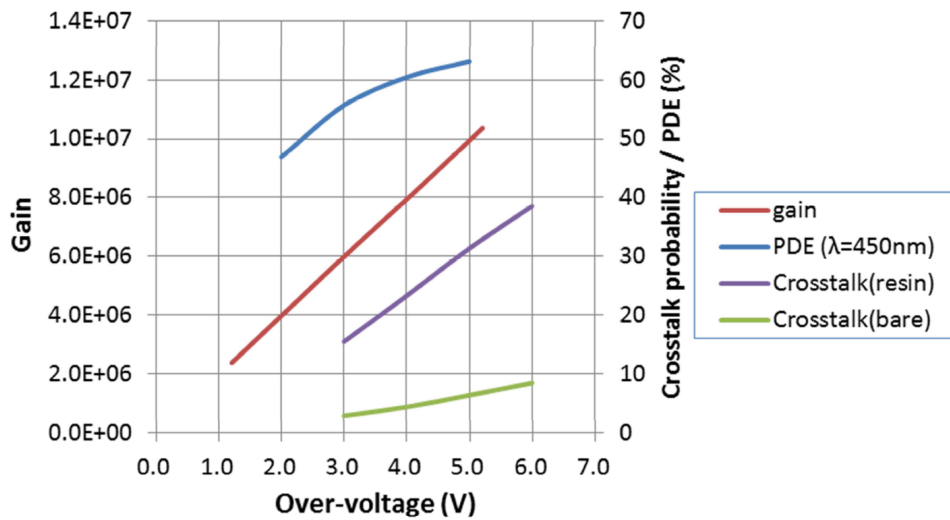
Figure 3.22: The effect of overvoltage on various performance parameters. HELIX uses the resin-type SiPM. Although the breakdown voltages vary channel to channel, they center around ∼38V. From Ham [2018].

61

3.3   SiPM Initial Characterization

3.3.1   Characterization Test Stand
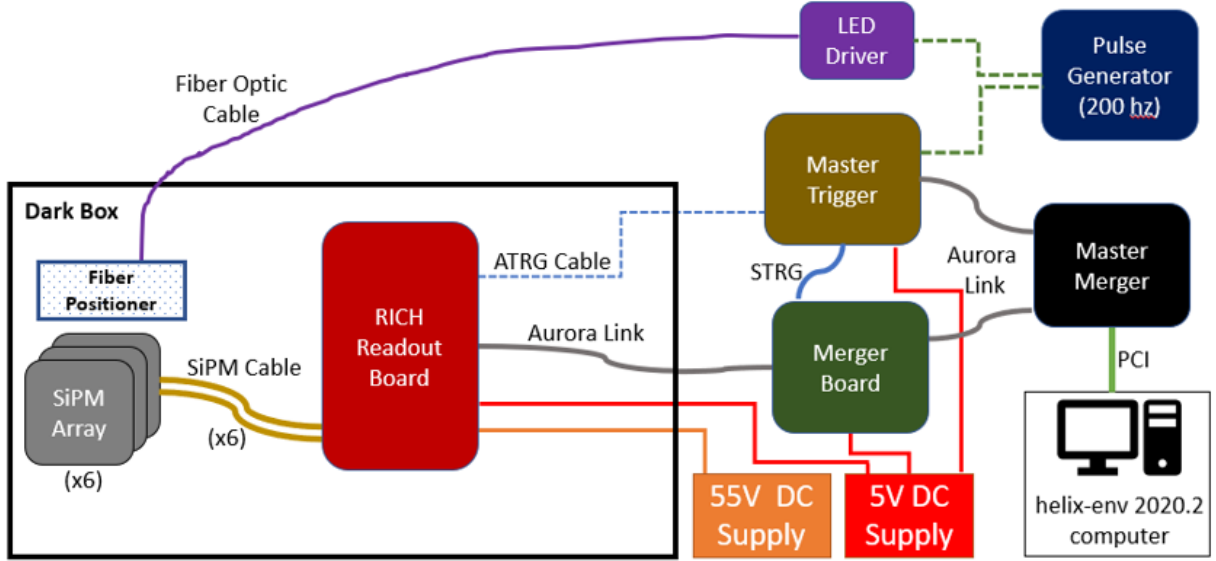
Figure 3.23: Schematic of the darkbox-based test stand used for early tests of the SiPM arrays and front end electronics.

I constructed a variety of test stands for this project for the purpose of testing and characterizing the SiPM arrays. However, prior to assembly of the focal plane I performed a majority of the SiPM and front end electronics testing with the use of HELIX's full sized darkbox. I did so by constructing a test stand inside the darkbox that could be easily adapted to whatever was needed. An outline of this darkbox's initial configuration is shown in Figure 3.23, and photos of the inside are shown in Figure 3.24. As can be seen in Figure 3.24a, the inside of the darkbox contains a 2D translation stage and custom SiPM array mount, a RICH front-end readout board, and a vortex cooler. The fiber positioner is shown in more detail in Figure 3.24b. The fiber's feed-through plate is moved horizontally with two lead screws powered by stepper motors, and vertically by a belt and stepper motor. The light from the fiber is collimated with a 3D printed cap such that the total illuminated area

62

is much smaller than a single 6mm × 6mm SiPM channel.

The 2D fiber positioner was controlled by an arduino with a stepper motor driving shield. I developed a control program for the arduino that used a serial connection to communicate with the 2D stage, and a Python library to manage the stage's position.
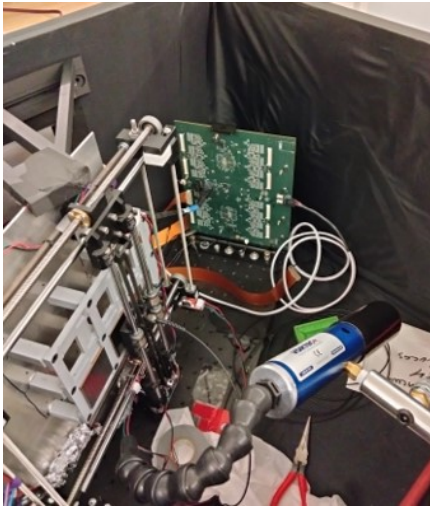
(a) A view inside the darkbox.
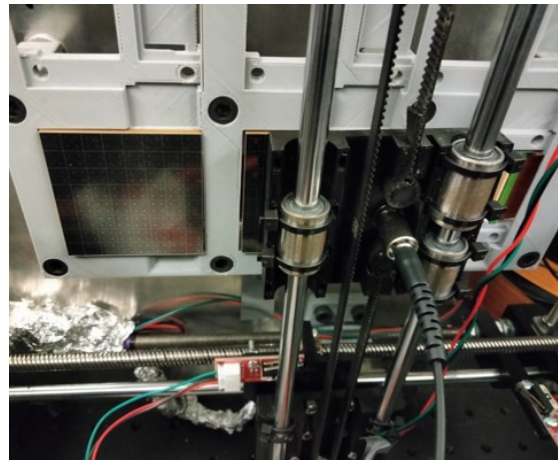
(b) The 2D fiber positioner and custom designed and 3D printed SiPM array mount.

Figure 3.24: The HELIX Darkbox

3.3.2   I-V Curves

I measured each SiPM channel's current response to a range of bias voltages (in an array of 64). The purpose of this study was to verify the functionality of every SiPM upon delivery, as well as independently measure the breakdown voltage of each SiPM. These tests were performed before I had access to any of the final front-end readout electronics.

The SiPMs were attached to a multiplexing board which connected one anode at a time to the bias supply's return path. The multiplexer was controlled by an Arduino taking commands from a control computer over a serial connection. The bias voltage and current measurements were made with a "Keithley 2450 SourceMeter" Source Measure Unit (SMU), also connected to the control computer via a serial connection. The board and SiPM array were housed within a light-proof project box under additional light blocking fabric, with

Figure 3.25: The minature darkbox used for early quality control checks of the SiPM arrays. The relays and PCB seen on the bottom allow for the 64 SiPM channels to be multiplexed to feedthroughs on the front of the box.

feedthroughs connecting the board inside to the Arduino and SMU. This minature darkbox is shown in Figure 3.25.

The SiPMs were biased one at a time, varying voltages in a randomly selected order. Each change in voltage was followed by a minimum 0.6 second pause to allow the current to come to equilibrium before 15 measurements of current were taken in rapid succession. The mean and variance of these measurements was recorded as the result at each voltage. The window of voltages is centered on the Hamamatsu reported breakdown voltage (the reported V_{op} - 3V), and has a higher density of voltages taken near this value.

The I-V curve data was used to verify the breakdown voltages reported by Hamamatsu and to detect abnormalities present in the SiPMs. Measurements with a charge to digital converter (QDC) and a discriminator/scaler were used to examine the behavior of SiPMs with abnormal I-V curves when biased at operating voltage. 45 channels exhibited anomalies, a 0.34% anomaly rate across all delivered SiPMs. Only 3 channels (0.02% of total) were fully

unresponsive.
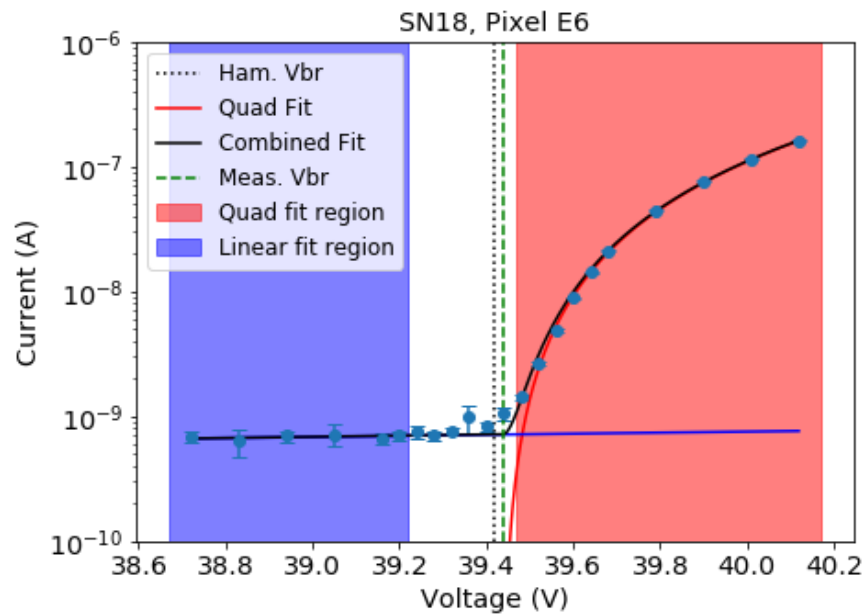
Figure 3.26: An example of a single SiPM's IV curve, with the two fitting regions highlighted. The breakdown voltage is determined by the vertex of the quadratic fit.
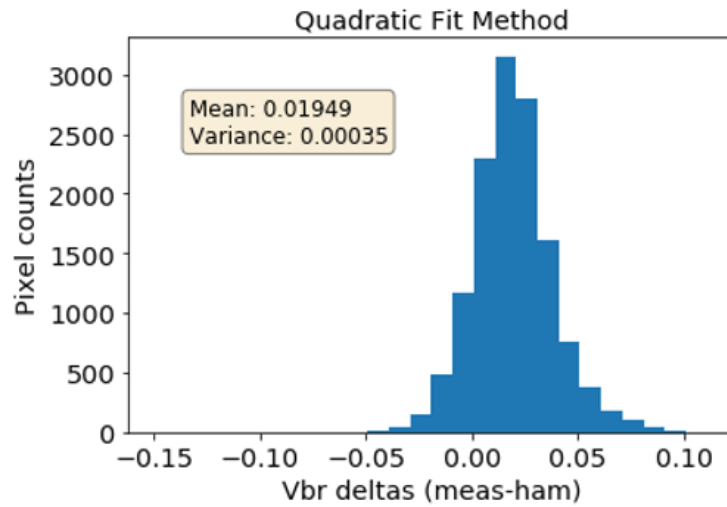
Figure 3.27: The difference in breakdown voltage between what was measured via the IV curve test, and what was reported by Hamamatsu.

The breakdown voltages were extracted from the I-V curves by fitting the above-breakdown data with a quadratic and using the vertex of the quadratic fit as the breakdown voltage, a

method outlined in Piemonte et al. [2007]. This method proved to be the more reliable than fitting a linear and exponential region, as could be naively assumed. An example of this fit can be seen in Figure 3.26. With anomalies and outliers due to fitting failures removed (about 0.05% of all pixels), a histogram of the differences between reported and observed values was produced and can be seen in Figure 3.27.

3.3.3   Dark Count Rate
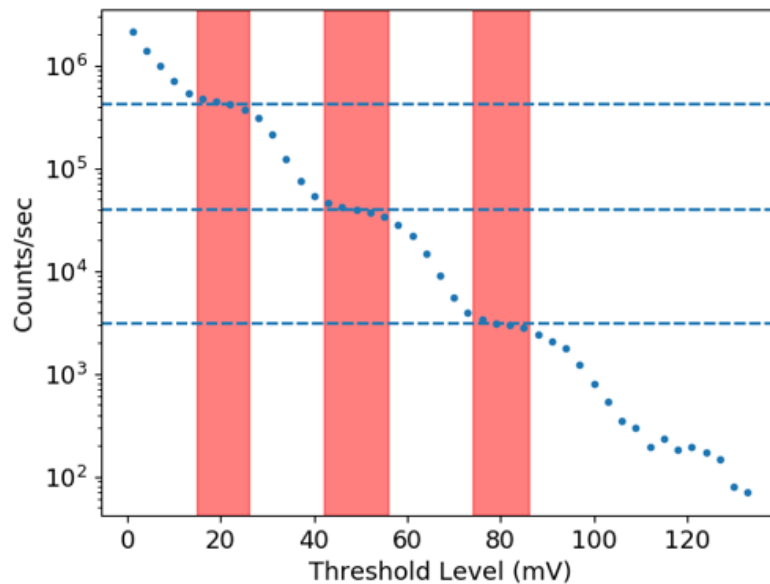
Figure 3.28: A frequency to threshold scan of one SiPM channel. The first three plateau regions are highlighted in red, and the heights of each of the plateaus averaged within the region and displayed by the dotted lines.

When all I-V curves were finished, I took measurements of the charge spectrum and dark count rate (DCR) from a small sample of SiPM arrays. This is done by removing the small multiplexing darkbox and connecting the SiPM to a simple breakout board and 50 ohm readout resistor. The Hamamatsu reported operating voltage is applied with a "BK Precision 9174B" DC power supply and two low pass filters. The output of the SiPM was amplified by two ~24.8 dB amplifiers and sent to a VME crate containing the charge integration counter

66
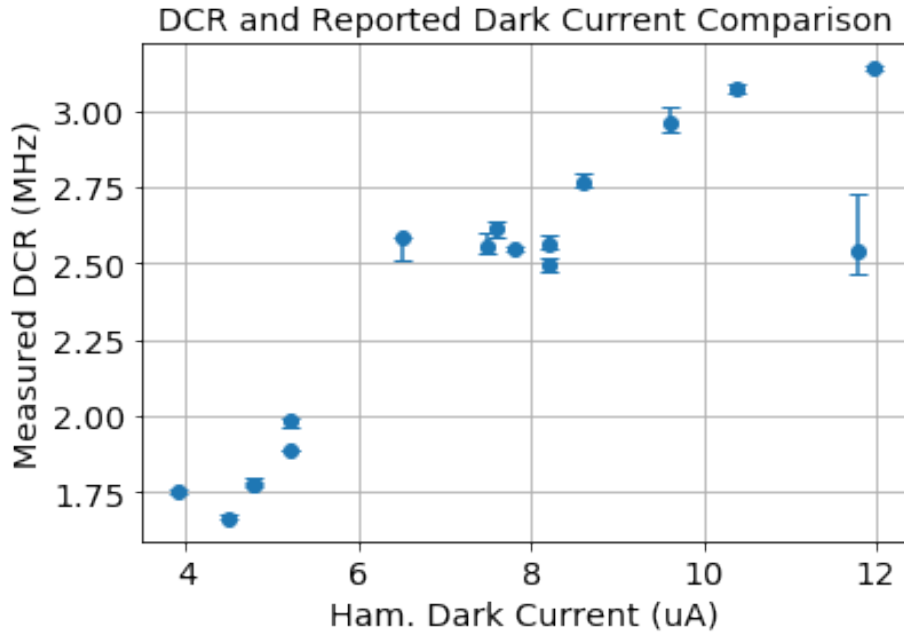
Figure 3.29: A scatter plot showing 16 of the channels on a SiPM Array. Each channel's dark current is what was reported by the manufacturer, and each DCR measurement is the fit to the first plateau, as shown in Figure 3.28. Dark current uncertainty was not reported.

(QDC) as well as the variable discriminator and scaler. This switch was done due to high capacitance in the multiplexing board distorting the SiPM's fast signals.

To measure the DCR, the discriminator's threshold was raised in steps and the signal frequency measured at each step. In an ideal SiPM, this should produce a "stairstep" effect, where the signal frequency plateaus in threshold regions between the quantized signals. When passing over the Gaussian distributed signal per-avalanche, the frequency drops. The DCR can them be determined by measuring the height of the first plateau under dark conditions. An example of the measurement of the DCR is shown in Figure 3.28. This relationship can be fit to a linear function for use in order-of-magnitude noise calculations.

3.3.4   Same-Channel Crosstalk

The same-channel crosstalk can be measured using the same technique outlined for measuring DCR. This is because the likelihood of two thermal excitations causing avalanches (the

primary contribution to dark noise) happening simultaneously in a SiPM is low. Instead, signals higher than the level of one avalanche are most likely due to crosstalk between APDs in the same SiPM. Therefore, the ratio of two plateaus in a plot of the discriminator's threshold scan should relate to the crosstalk fraction. Like other properties, the crosstalk varies with bias voltage and therefore temperature. At Hamamatsu's testing conditions, a crosstalk of $\sim 16\%$ was expected. I found the crosstalk to be on the order of 10%.

3.3.5   Gain
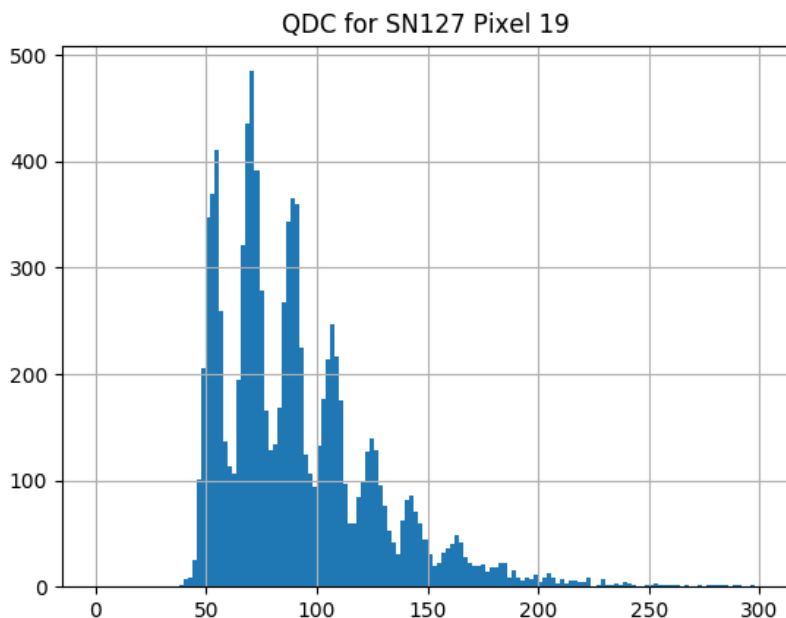
Figure 3.30: A histogram of charge integration measurements, in arbitrary units. The separation between PE count peaks is clearly visible and linearly spaced, as expected.

An LED flasher triggered from a function generator can be added to the same test environment described for the DCR measurements. This allows the pulse from the SiPM to be integrated by the QDC and used in verifying the SiPM's gain properties. This was used to show that light levels in the test stand could be well controlled, and that the charge spectrum was qualitatively performing as expected (Figure 3.30).

3.3.6   Timing Jitter Toy MC
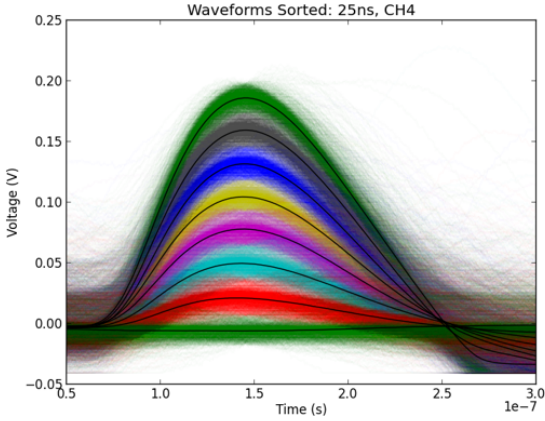
(a) Digitized oscilloscope traces of shaped SiPM outputs, sorted by quantized signal level. The black lines show the averaged trace of each PE level.
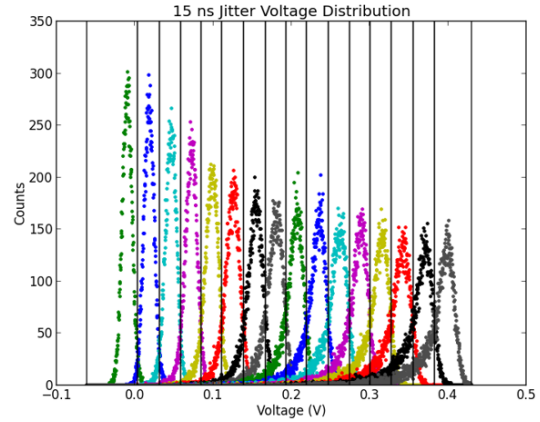
(b) An example spectrum generated from the SiPM toy MC, using the data from 3.31a. Each PE was sampled the same number of times, and colored differently. Crossing points between distributions are marked with horizontal black lines. Colors between the subfigures are not correlated.

Figure 3.31: The HELIX Darkbox

Prior to delivery of the finished front-end boards from Indiana University, I used an evaluation board for the CITIROC ASIC to measure the likely effects of our SiPM readout chain. This was done by flashing the SiPM array with LED light in the same method as outlined in the prior subsection, but rather than sending the SiPM signal through our own filtering and amplifier chain it was instead processed by the evaluation board and read out via an oscilloscope. The traces from this oscilloscope were digitized for use in analysis.

I next created a toy Monte Carlo of the SiPM readout using this data. First, I took a time slice of the traces at their peak time, around 145 ns in Figure 3.31a. The resulting histogram was smoothed and the local minimums were set as boundaries between the photoelectron (PE) levels. Each PE segment in that time slice was fit to a Gaussian to model the distribution of electronics noise. Each set of PE traces was then averaged at each time slice to create an average trace for each PE.

69
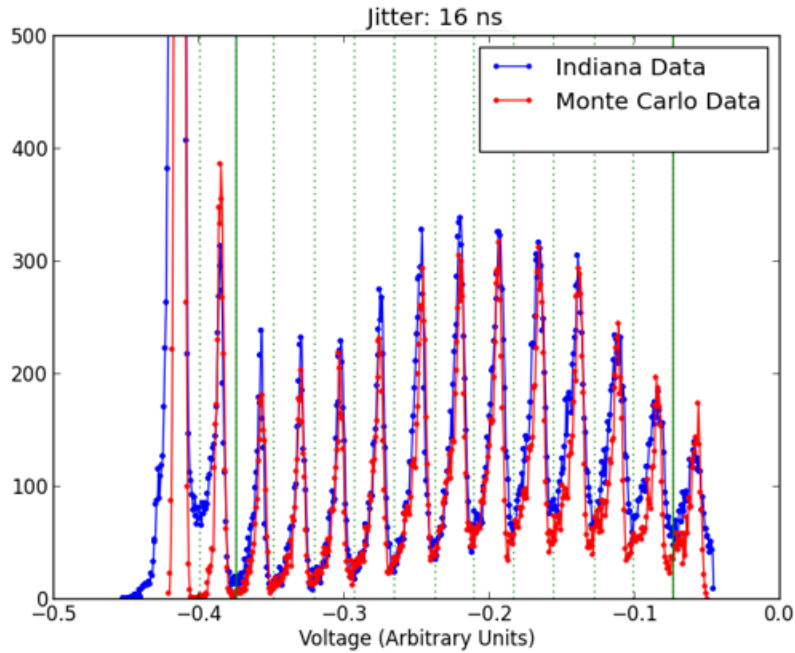
Figure 3.32: Toy MC data overlaid on data generated from the results of early electronics tests at Indiana University.

The inputs for the toy MC were the number of events at each PE level and the timing jitter of the run. For each event a timing offset from the peak position was selected from a Gaussian distribution with a width corresponding to the set timing jitter value. The value of average trace corresponding to the PE count of that event at the selected time was used as the mean value for a second Guassian distribution with width corresponding to the electronic noise. The final value was then selected from that distribution. This process was repeated for each event, an example of the resulting distributions for a jitter value of 15 ns is shown in Figure 3.31b.

This toy MC was then used to characterize the timing jitter present in tests of the prototype RICH data acquisition system. Distributions of SiPM signal voltages were fit to real data taken at Indiana University (IU), with the heights of each peak, the noise width, and the jitter allowed to vary. The best fitting timing jitter was found to be 16 ns, the results of the toy MC with this jitter value are shown overlaid on the IU data in Figure 3.32.

70

3.3.7   Channel Mapping
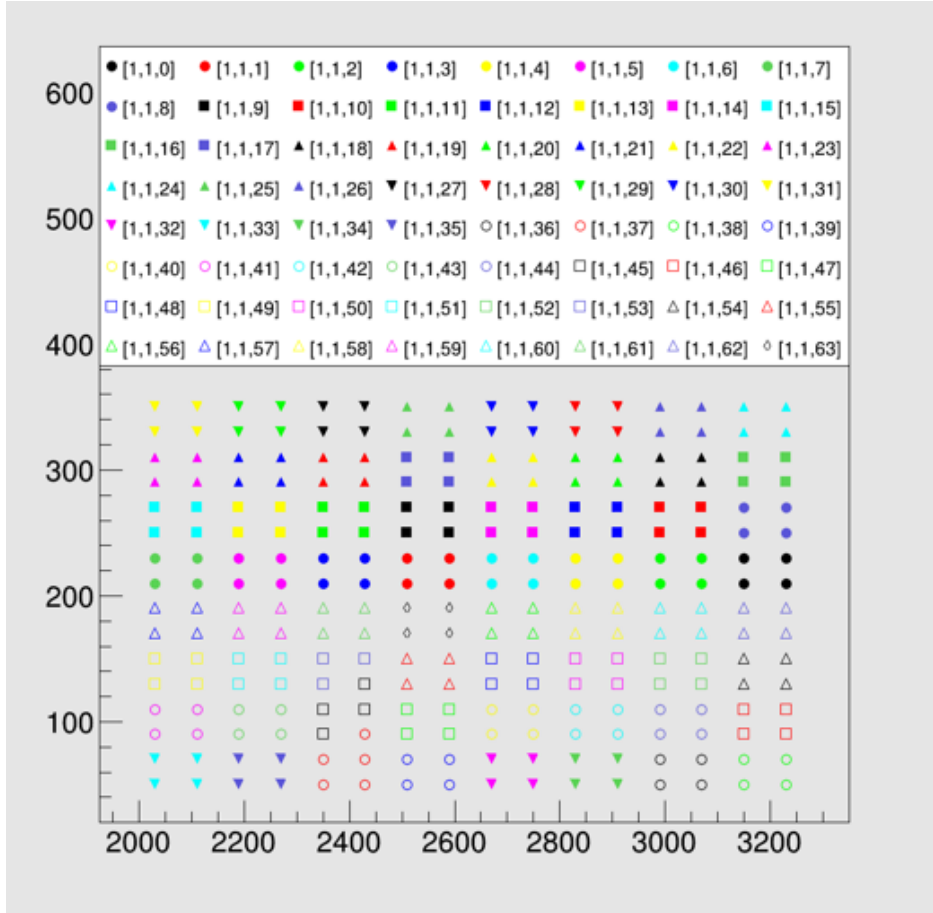
Figure 3.33: XY locations of the fiber positioner in units of stepper motor steps, and what channel reported the highest signal while the fiber was at each position.

After the arrival of the full RICH readout chain (discussed in section 3.5), it became necessary to map the software level channels of each SiPM serviced by each RICH front-end board to the SiPM's physical position. Although in theory this is possible by chaining maps of channels through multiple levels of hardware, software, and firmware, this "first principles" method is prone to human error and unable to detect unforseen bugs or mismappings. Instead, I used the 2D fiber positioner and test stand I constructed, as outlined in Figure 3.23, to scan light across known physical locations. I then searched the fully processed data to correlate what channels reported signal with what channels received light. An example of

71

a channel mapping built for a single array with this mapping can be seen in Figure 3.33. In addition to building accurate channel maps, this method was useful for detecting issues with disconnected or unresponsive channels, as shown in Figure 3.34. The diagnosing of these disconnected channels is covered in more detail in section 3.5.
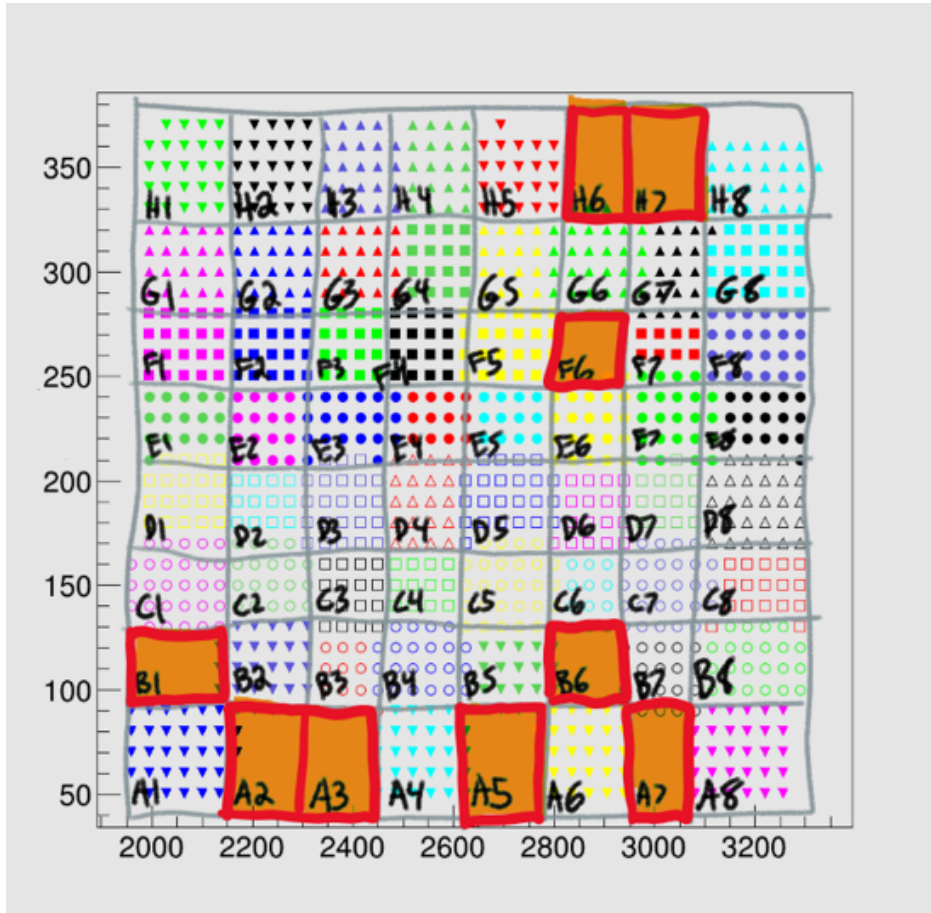
Figure 3.34: Channel mapping with the physical SiPM positions drawn on top. Nine channels, highlighted in orange, are missing signals.

3.4   Hodoscope Evaluation

3.4.1   Hodoscope and Test Stand Design

My work on HELIX's hodoscope concerned the testing and characterization of the first scintillating fiber ribbon delivered by the manufacturer, Saint-Gobain, for analysis. These ribbons are made of 150 1 mm × 1 mm cross section square scintillating fibers. The ribbon's glued section is 600 mm along the length of the fibers. The each fiber is then separated and individually woven and terminated into a Delrin cookie. A simplified diagram of a ribbon and cookie are shown in Figure 3.35. The weaving of the fibers into the cookie is shown in Figure 3.36a.

The purpose of this evaluation was to confirm the full functionality of the interface between the fiber ribbon's terminating cookie and a Hamamatsu 8x8 SiPM array, verify detectable scintillation, and to set a bound on the optical crosstalk between adjacent fibers.
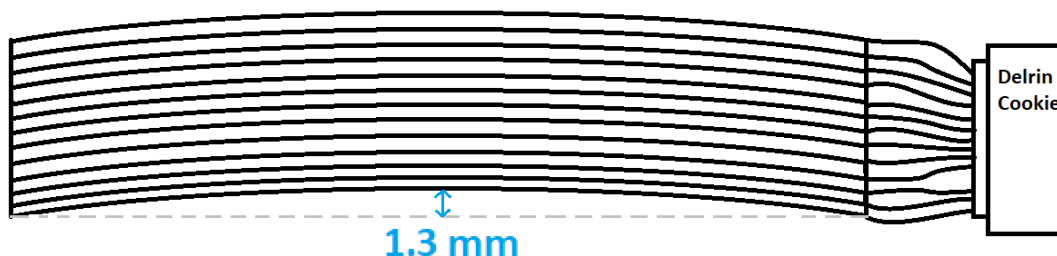
Figure 3.35: A simplified diagram of one 150 fiber hodoscope ribbon, as viewed from above. The glued ribbon section used in the detector is visible on the left, and the weaving of the ribbon into a Delrin cookie is visible on the right. In the evaluation ribbon, a 1.3 mm geometric deviation from the centerline was found.

Measurements of the scintillating fiber ribbon are taken using two similar experimental setups. In both setups, the cookie is mated to a Hamamatsu 8x8 SiPM array using Saint-Gobain BC-630 optical grease. This connection is held in place using a 3D printed mount
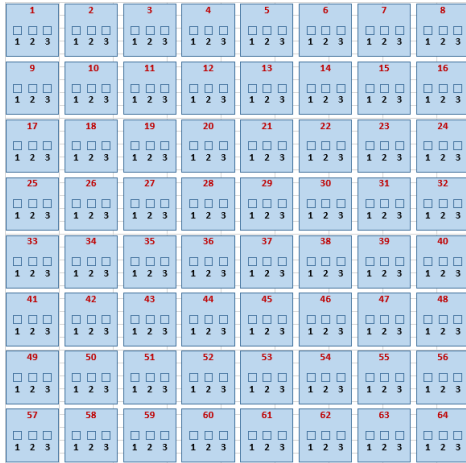
(a) A diagram of the mapping between the ribbon fibers and the holes in the Delrin cookie. Notice that each square supports three fibers - this is for multiplexing the 150 channels into the 64 channel SiPM array.
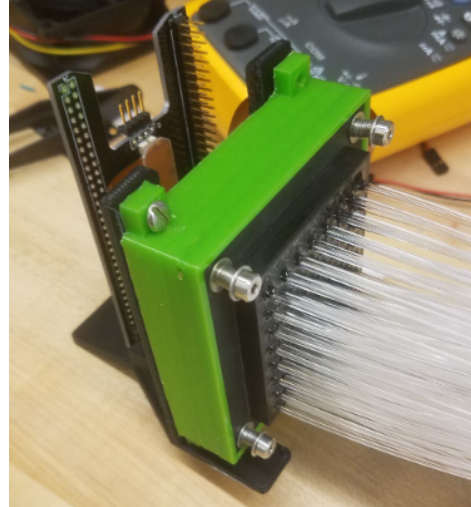
(b) A Delrin cookie terminating one of the hodoscope ribbons, in a 3D printed mount I custom designed. A breakout board is mounted on the back to allow individual SiPMs to be picked out of the 64 SiPM array for measurement.

Figure 3.36: Hodoscope Cookie Design

with dimensions matching the final mounting bracket. Constant, even pressure is applied to the cookie through the use of spring loaded screws located on all four corners of the cookie, shown in Figure 3.36b.

The SiPM array was attached to a 64 channel breakout board, which allows individual channels to have bias applied and signals read out independently. The Hamamatsu reported operating voltage of 42 volts is applied with a BK Precision 9174B DC power supply and two low pass filters with a cutoff frequency of 933.5 kHz. The output of each SiPM channel was amplified by two ZFL-500LN+ amplifiers in series, each powered at 9.50 V. The signals are then measured directly by an oscilloscope, with the signal corresponding to the fiber used as a trigger: this signal is split using a Model 428 Linear Fan-out to be read by both the oscilloscope and a VME discriminator. This discriminator is used to determine if there was a detection in the amplified SiPM channel of magnitude 186.1 mV, corresponding to ~24 photoelectron (PE) counts, or greater.

In all cases, all light sensitive components are covered in light blocking fabric and cardboard, and the lights in the lab were turned off.

3.4.2   LED Tests
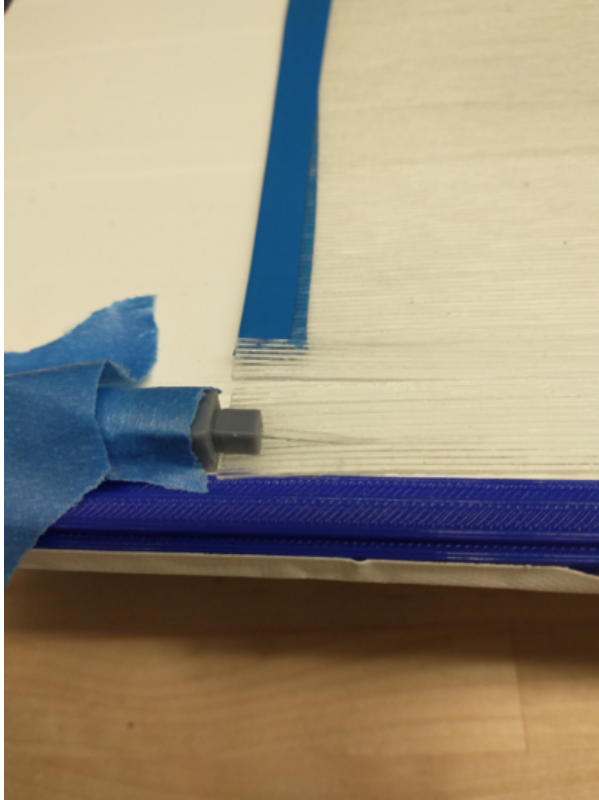
(a) The picked-off scintillating fiber entering the flasher's fiber optic adapter.

(b) The mask used to block light to all except one SiPM channel (used by 3 non-adjacent fibers).

Figure 3.37: The LED light test stand

For solely optical measurements, an LED flasher and fiber optic cable were used to provide the source light. One scintillating fiber was separated slightly from the glued (non-cookie) end of the ribbon and polished. I then placed this scintillating fiber into a custom 3D printed adapter that holds the fiber optic cable's light pulses perpendicular to the polished end of the slightly separated fiber, as shown in Figure 3.37a. Next, an opaque plastic mask was placed between the SiPM and the cookie, blocking all channels except the channel adjacent

to the one receiving the flash. This allowed large light pulses to be used without saturating the SiPM output from the channel corresponding to the flashed fiber. Removing the mask results in electrical crosstalk within the SiPM that was not of interest in this study. The flasher is set to its maximum output, ~60 PE counts.

The oscilloscope was provided the same external trigger as the LED flasher. By measuring the signal in the adjacent fiber, a bound can be placed on the optical crosstalk between the flashed fiber and the adjacent one. The benefit of this method is that the light is well controlled and manually timed, resulting in consistent and easy measurement. The disadvantage to this method is that the light traveling through the fiber was applied as an existing beam profile at the end of the ribbon, and so may not have the same geometry as light created within the fiber itself through scintillation.
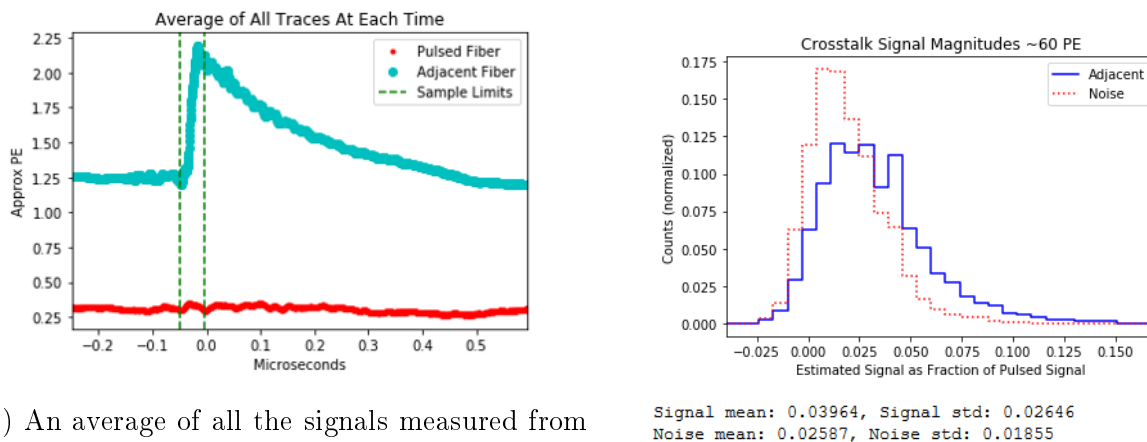
(a) An average of all the signals measured from the pulsed fiber and an adjacent fiber. The dashed lines show the bounds from where the maximum signal height was selected for each measurement. This measurement was taken with the pulsed fiber masked off from the detector.

Signal mean: 0.03964, Signal std: 0.02646
Noise mean: 0.02587, Noise std: 0.01855

(b) Histogram of the approximate PE counts in the fiber adjacent to the flashed fiber. Noise was measured in a different time window from the flash.

Figure 3.38: Hodoscope Cookie Design

A simultaneous measurement of the signals from the flashed fiber and an adjacent fiber is taken, and the maximum value of each of these signals within a half-microsecond window is recorded as the signal height. Since the fiber receiving the flashed light is masked off at the detector end, its signal should be low, removing any electrical crosstalk that occurs within

the SiPM array or further downstream. An average of these measurements can be seen in Figure 3.38a. The signal heights for each measurement are then divided by the expected ~60 PE signal height of the primary flash. This provides a measurement of the approximate crosstalk fraction. To produce a noise measurement, the same process is applied to the signal measurement two full microseconds before the flash. The results of this analysis can be seen in Figure 5. The mean of the adjacent fiber's distribution increases above noise by 0.014. This would correspond to a crosstalk of 1.5%. However, as previously, this could be an optimistic bound due to the nature of the incoming light profile.

3.4.3   Source Tests

The second measurement setup uses a 12 µCi Sr-90 beta source in a brass collimator which has a 1mm diameter round opening through 6.5 mm of brass. This collimator is used to direct beta particles through the scintillating fiber, producing light within the fiber. A scintillating paddle is placed underneath the fibers. A trigger signal is generated on the coincidence between a signal from this lower paddle and a signal from the fiber targeted by the beta source: this establishes that the measured signals are produced by betas that pass entirely through the fibers. A diagram of this setup is shown in Figure 3.39. Three signals are measured: the fiber used as part of the coincidence trigger, a fiber adjacent to the "triggered" fiber, and a fiber two fibers away from the triggered fiber. This means that three sequential fibers are measured.

The simplest analysis of the measurements using the beta source is to compare the signal height of the triggered fiber to the fiber directly adjacent to it. One method of doing so, illustrated in Figure 3.41, is to set a trigger threshold of 24 PEs, and then observe how many signals in the adjacent fiber cross this threshold as well. This "binary crosstalk" occurred in 4.3% of events. An alternate analysis for directly adjacent fiber is to analyze the fractional height of the adjacent signal in comparison to the triggering signal. This is done using the
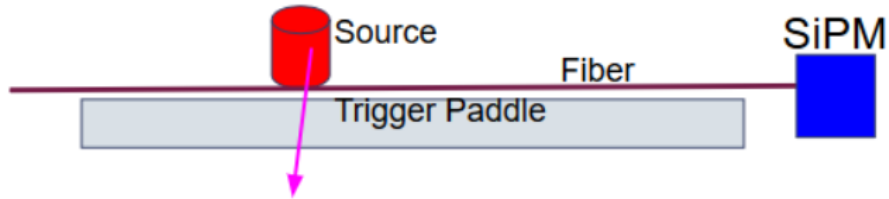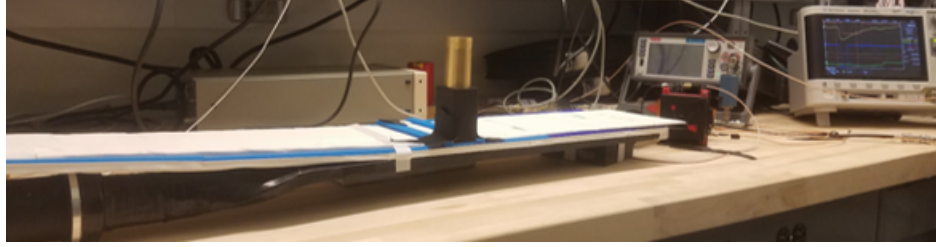
Figure 3.39: (Top) The test stand used in initial characterization of the hodoscope ribbon. The ribbon is resting in a custom 3D printed track I designed, including a 2D rail system to hold the collimated β source in place. The triggering scintillator paddle is visible in black cladding on the bottom. (Bottom) A simple schematic of the hodoscope test stand.

same method outlined for optical measurements, using the measured triggering signal height for each event rather than an assumed 60 PE pulse. The resulting distributions are shown in Figure 3.42. The median of the signal distribution is 0.056 above the median of the noise distribution, representing a crosstalk measurement of 5.6%.

As can be seen in Figure 3.41 and Figure 3.42, the signal distribution has a significant tail. This is partially due to particles passing through both fibers, and therefore registering significant signals in each. This is one reason medians are used for the beta distributions instead of means. To further combat this effect, a geometric cut can be applied to this analysis by requiring that both the triggered fiber (fiber 1) and its adjacent fiber (fiber 2) have signals above 20 PE, ensuring that a beta from the collimated source has passed through each. This way, the geometry of the setup assures that although the particle has passed through the adjacent fiber, if it originates from the collimated source it cannot pass through fiber 3. This is illustrated in Figure 3.40.

With this cut applied, the height of the signal in fiber 3 is compared against the signal in fiber 2 in the same way as before. This cut eliminates many cases where particles are
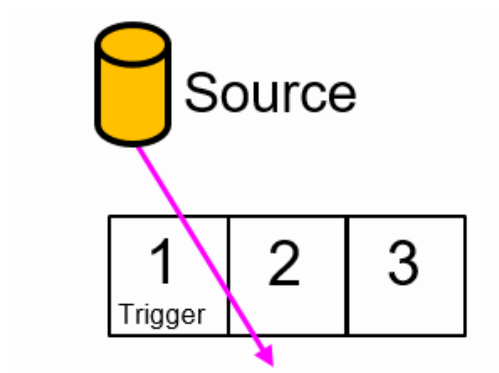
Figure 3.40: An example of how three fibers are used to form a geometric cut. The particle must primarily pass through fiber 1, which geometrically excludes the particle passing from the source through fiber 3. The signal in fiber 3 is compared to the signal in fiber 2.

passing through both fibers, and therefore reduces the tail of the distribution. The result is shown in Figure 3.43. The median of the signal distribution is 0.017 above the median of the noise distribution, representing a crosstalk measurement of 1.7%.
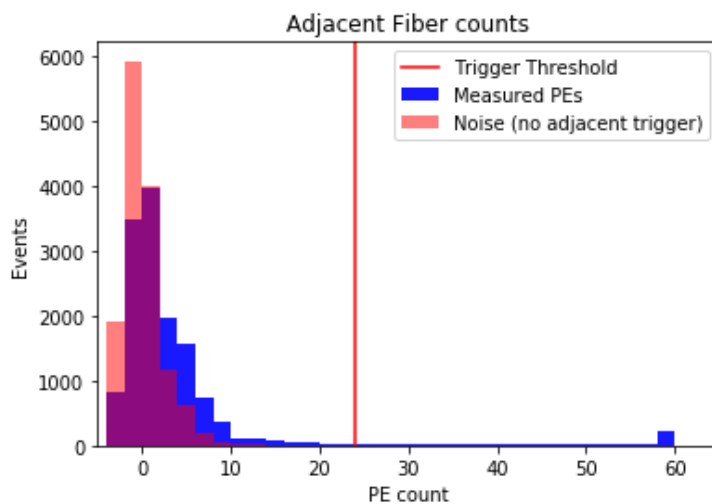
Figure 3.41: Histogram of PE counts resulting from particles passing through the fibers. The trigger threshold of 24 PEs used to define a detection is shown.

3.4.4   Hodoscope Ribbon Evaluation Conclusions

This evaluation showed that the interface between the terminating Delrin cookie and the readout SiPM is fully functional, meeting expectations. The crosstalk between fibers was

79
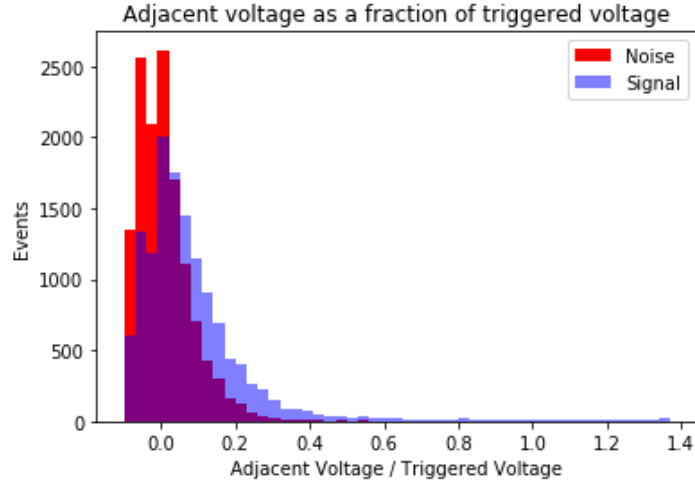
Figure 3.42: Histogram of the signal height in the adjacent fiber as a fraction of the signal height in the triggered fiber, per event.
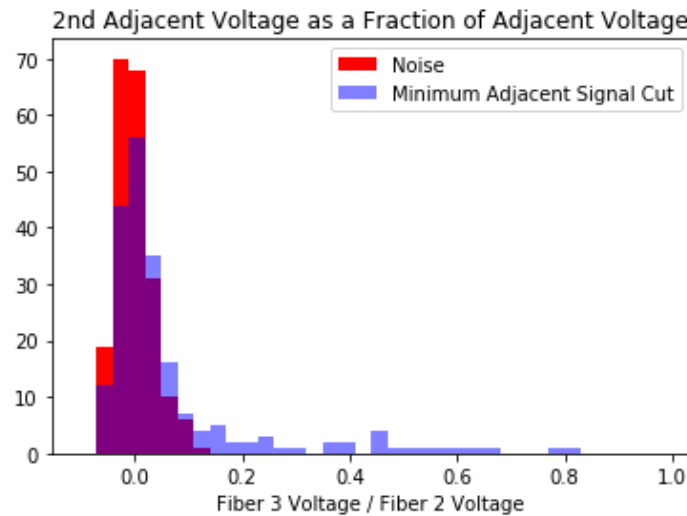
Figure 3.43: Histogram of the signal height in the third fiber as a fraction of the signal height in the second fiber, per event. The "Minimum Adjacent Signal Cut" requires that both the first and second fiber reach a minimum signal threshold of approximately 20 PEs.

measured using multiple methods, with the lowest upper bounds on the crosstalk found to be 1.5% in the purely optical measurements and 1.7% using scintillation as the light source. The most conservative (highest) upper bound was found to be 5.6%, which would include events where the particle causing the scintillation passed through both fibers. These values

either matched or beat the required 5% optical crosstalk shown to still allow the hodoscope to be fully effective in toy Monte Carlo simulations.

With these bounds on the crosstalk measurements, the most concerning outcome of this study was a physical deformity of the ribbon, illustrated in Figure 3.35. Deviations of this nature ultimately led to a hodoscope mapping project undertaken by other members of the UChicago team, led by Hyebin Jeon.

Additionally, the holes for the fibers in the Delrin cookies were found by the ribbon manufacturer, Saint-Gobain, to be smaller in diameter than was required to thread the fibers through. I fixed this issue by individually widening each hole on every cookie with a jeweler's file before returning them to Saint-Gobain for fiber weaving, gluing, and fly cutting.

3.5   RICH Data Acquisition Electronics

3.5.1   Overview
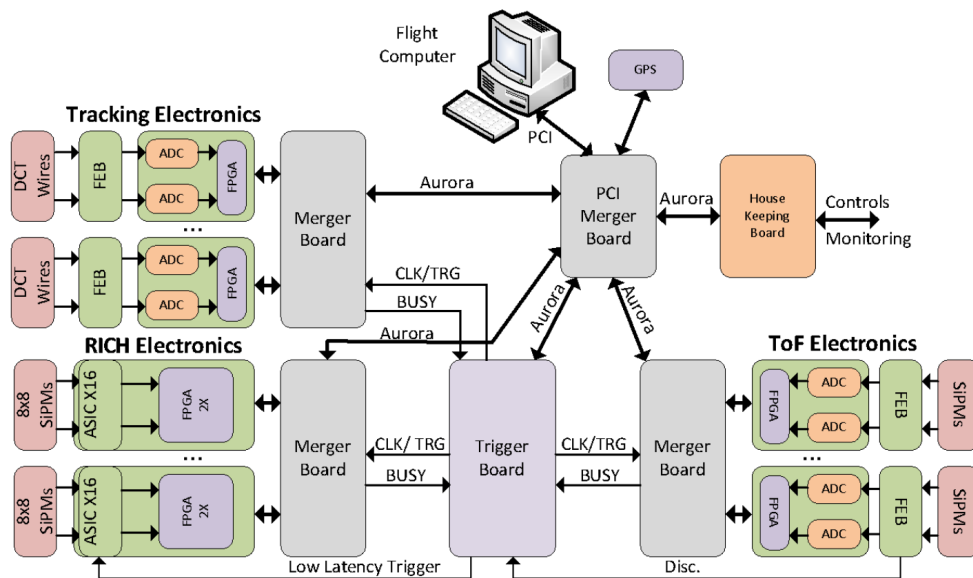
Figure 3.44: An overview of HELIX's data acquisition system, from Kunkler and Wisher [2019].

HELIX's data acquisition, outlined in Figure 3.44, is designed to provide stable support to all data taking subsystems in the difficult environment of the upper atmosphere. This means that once deployed, the system will not be reachable for any repairs and so must be both reliable and be able to deal with any faults that arise during a flight.
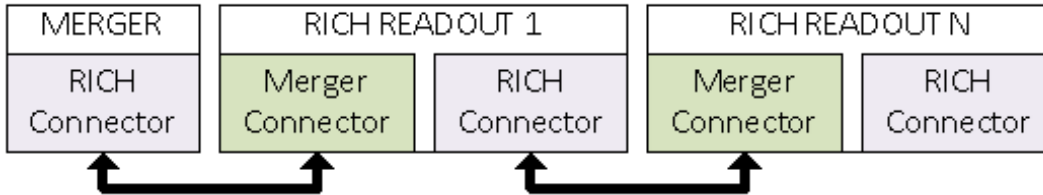
Figure 3.45: An overview of the RICH FEB's daisy-chain, from Kunkler [2022].

The center of HELIX's readout and control system is a single "flight" computer. The readout and control system uses a common interface architecture using Xilinx Artix-7 PG-GAs and communicates primarily over high-speed serial links. The flight computer connects to this system via a Dini Group FPGA board mounted in a PCI slot. This PCI merger board connects to the trigger board, the housekeeping board, and a set of merger boards which in turn connect to the front-end boards for each subsystem. Rather each RICH FEB connecting to a merger board via an individual link, they are instead daisy-chained (up to a maximum of 5 boards per chain) as shown in Figure 3.45.

3.5.2   SiPM Cables

HELIX's SiPM arrays are connected to the front end electronics with custom Flexible Printed Circuit (FPC) cables, shown in Figure 3.46. These cables have three planes of conductors, two sides for individual lines on either side and center plane pour on which the cathode bias voltage is carried. A FX11B-100P-SV connector is soldered to each end of the cable using surface mounts and a plastic backing is attached for mechanical durability. The connectors are mechanically symmetric about 180 degree flips other than a small indicator on the upper-right hand corner, so a white dot is added to the edge containing the temperature sensor
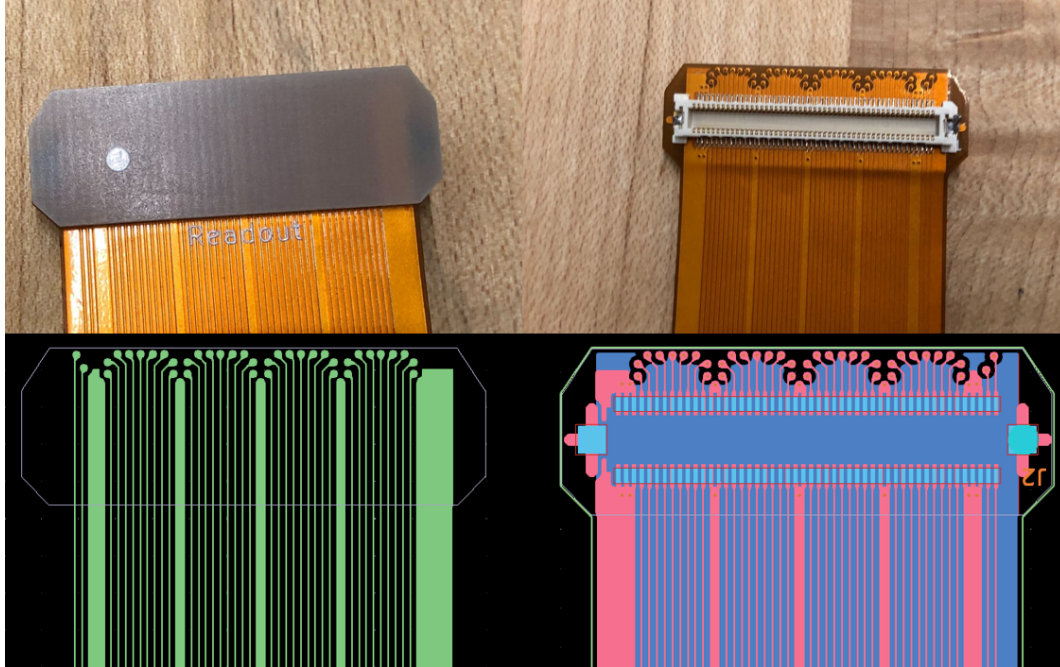
Figure 3.46: HELIX's Flexible Printed Circuit (FPC) cables used to connect the SiPM arrays to the front end electronics. Top: Photos of the two sides of the cable connector. Bottom: A view of the Gerber files for the cables, showing the traces on each side.

lines to indicate directionality. Labels for the "Readout" and "SiPM" ends were also added for consistency.

As mentioned in section 3.3, in some channel mapping tests a significant number of channels were found to be unresponsive. A very small fraction of these disconnected channels were traced to the front-end boards or the SiPM arrays themselves, but I localized a vast majority of the disconnects to the flex cables. When examined under a microscope, it became clear that poorly soldered connections between the flex cable and the surface-mount connectors were the source of these issues. I determined that the poor soldering was unique to a single batch of early cables, and upon inspection later cable deliveries were found to be of sufficiently high quality for use in flight.

Figure 3.47: A microscope view of the surface mount solder points on the SiPM cables. A disconnected pin is marked with a red arrow.
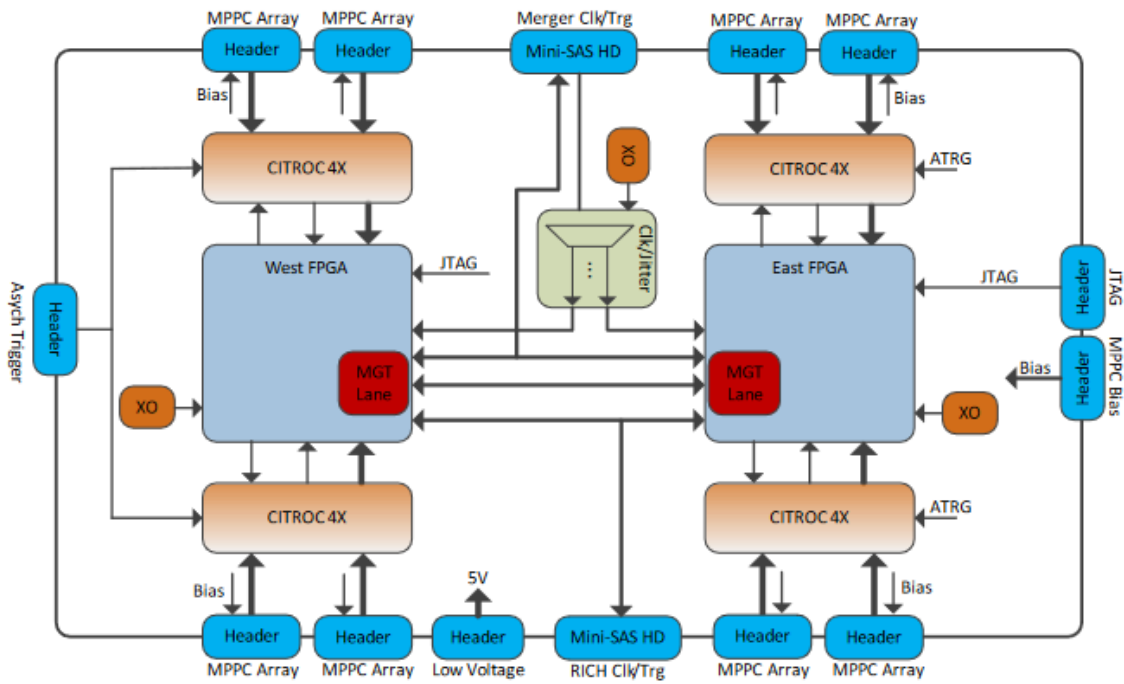
Figure 3.48: RICH FEB block diagram from [Kunkler, 2022].
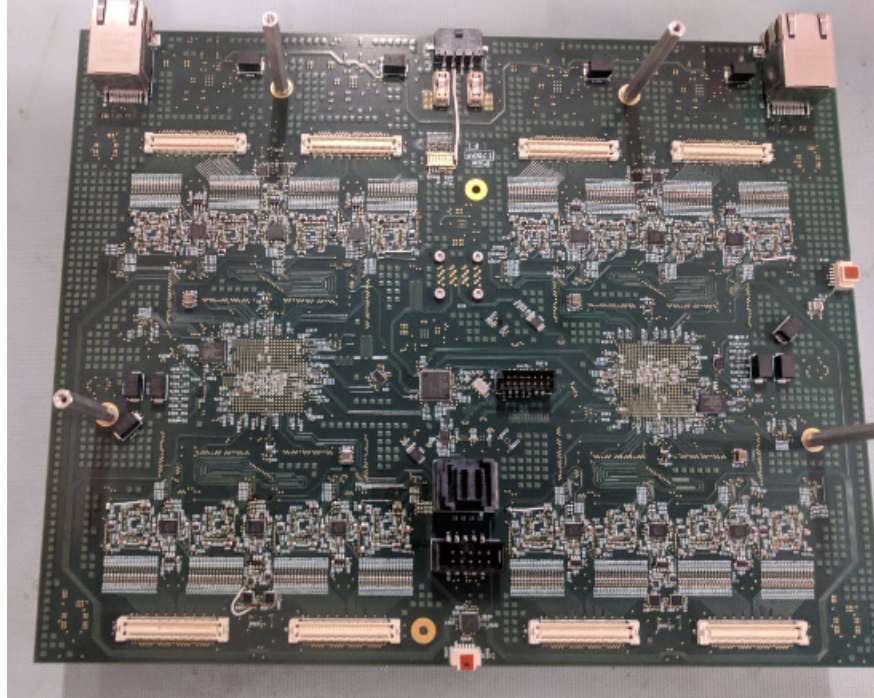
Figure 3.49: The topside of the prototype RICH FEB.

3.5.3   RICH Front End Boards

The RICH front-end boards (FEBs), often simply referred to as the "RICH boards", read out the SiPM arrays used in the RICH focal plane and the hodoscope. They were custom designed for HELIX by IU engineer Brandon Kunkler [Kunkler, 2022]. Each board is responsible for eight SiPM arrays. As shown in Figure 3.48, each RICH board is split into two "logical" boards, each serviced by a single Xilinx XC7A200T FPGA. The shared connections on each board between to the two logical boards are the asynchronous trigger, a JTAG connection for programming FPGAs, a SiPM bias voltage supply input, two SAS connectors for receiving and transmitting signals from the Merger board along a chain of RICH boards.

Four connector positions per logical board are present for SiPM cables. An independently controlled bias supply provides the cathode voltage for each attached array. Each SiPM array requires two 32-channel Citiroc ASICS for readout. These Citirocs are controlled by their board's FPGA, with the exception of the aforementioned asynchronous trigger signal sent

directly from the trigger board, which controls the sample-and-hold operation.

3.5.4 Citiroc ASIC
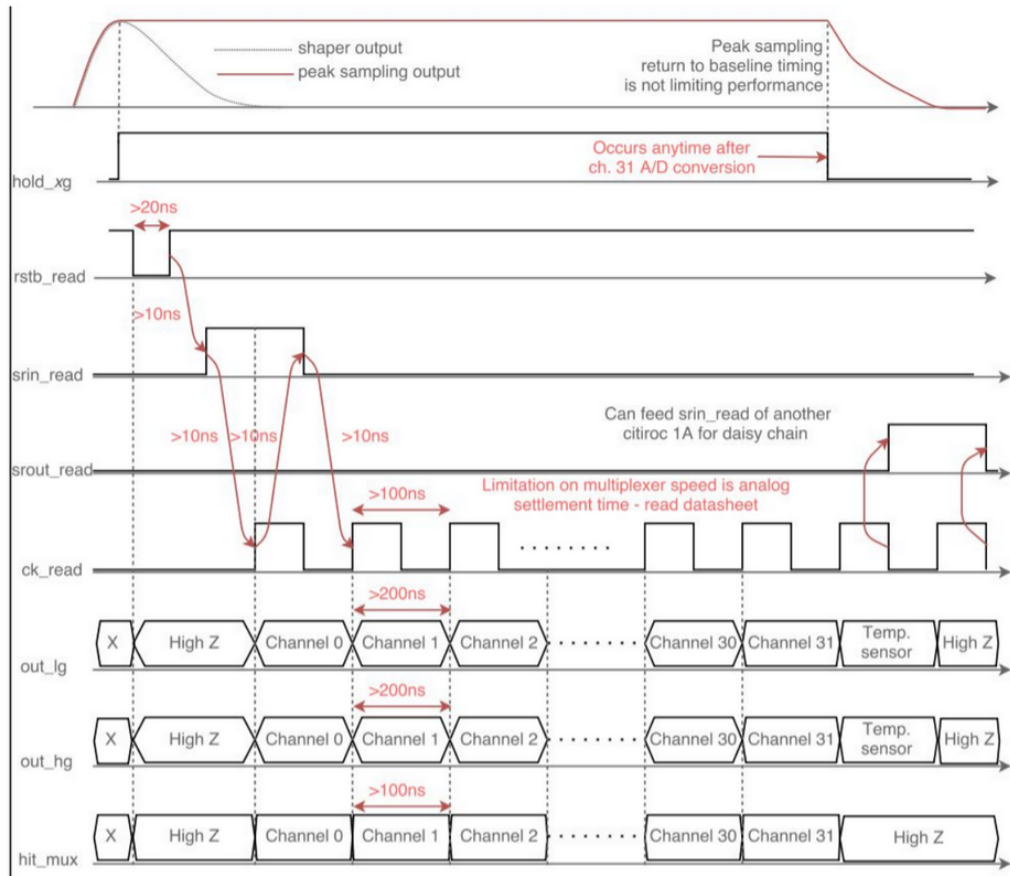
Figure 3.50: A Chronogram of the Citiroc 1A's readout process [WEE, 2019].

The RICH FEB uses 16 Citiroc 1A ASICs to read out the SiPMs. Each Citiroc ASIC provides pulse shaping and preamplification to 32 SiPM channels, as well as a "sample and hold" operation on the output in response to an asynchronous trigger (ATRG). The 32 results are then read out in serial and digitized by an external ADC. This sample and hold operation and readout multiplexing is outlined in Figure 3.50. I measured this readout process directly by soldering probes to the prototype RICH FEB and monitoring the output with an oscilloscope (Figure 3.51).
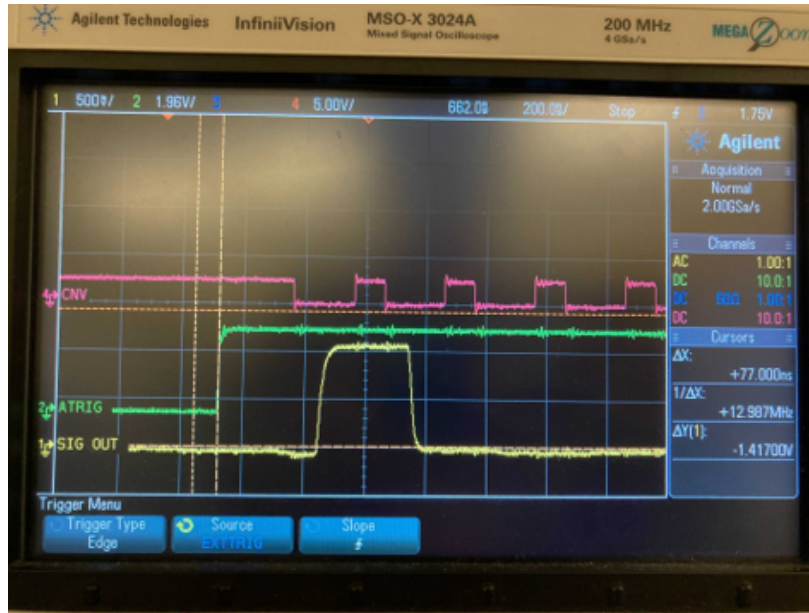
Figure 3.51: The process of reading out a single Citiroc, measured on an oscilloscope. CNV, ATRG, and SIG OUT are analogous to hold_xg, ck_read, and out_hg in Figure 3.50.

In addition to this primary readout method, the Citiroc also contains a second "fast" shaper and internal discriminator used to send parallel per-channel pulses when a signal above a set level is detected. Finally, the Citiroc is able to apply a separately controllable "virtual ground" to each of the 32 SiPM anodes. Since the cathode voltage can only be controlled at the array level, the virtual ground allows the bias voltage to be adjusted on a channel-by channel basis.

By changing the delay between a calibration light pulse and the time at which the ATRG signal is sent, the Citiroc shaped pulse can be mapped out without resorting to probing or modifying the readout system. This is demonstrated for a range of shaping values in Figure 3.52. Although ordered as expected, it was found that the peaking times differed significantly from those reported by the manufacturer. This "ATRG sweep"' method is used to calibrate the ATRG delay in the trigger board so that the arrival of the hold command corresponds with the peak of the shaped signal. An example of this process is shown in Figure 3.53.
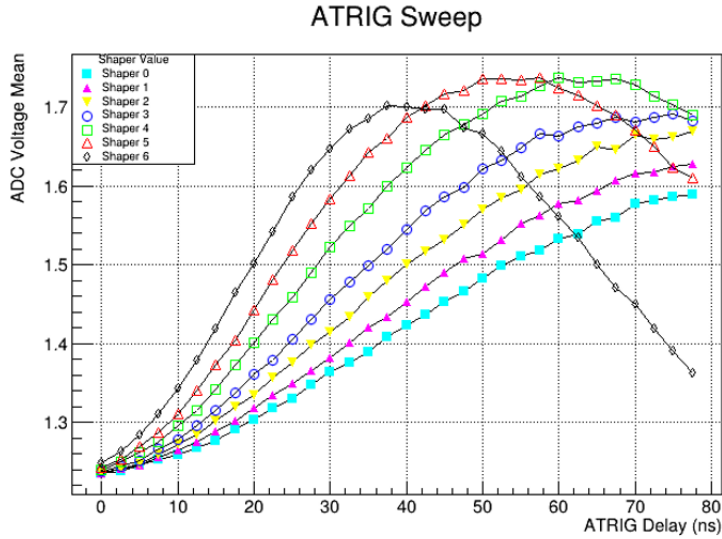
Figure 3.52: An ATRG scan with different shaper settings.
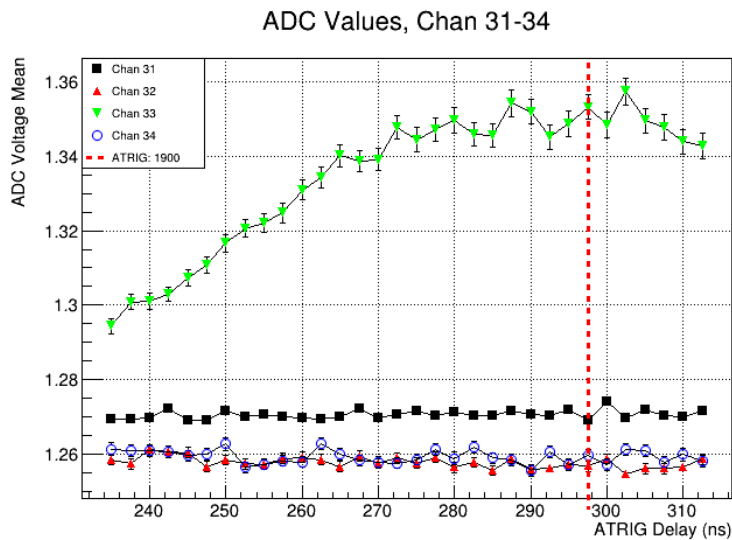
Figure 3.53: An ATRG scan with only one channel illuminated. The dashed vertical line is the delay selected to center the peak. A static delay of 232 ns was applied by the triggering pulse generator.

3.5.5   Firmware and Software Development

The readout and control boards were developed at Indiana University and the Ohio State University, and after preliminary testing they were sent to the University of Chicago for me to test, debug, and integrate. Much of my work involved many hours verifying the

functionality of all features, documenting the results, and iterating on designs and tests with the engineers and scientists who designed the boards. I also was responsible for testing and debugging the flight software responsible for the board control loops, data collection, and monitoring. My work was absolutely necessary to creating a working and reliable detector. Since enumerating all every one of the small debugging tasks this project involved would not be practical, I instead have listed below some examples of such work.

Temperature Sensors
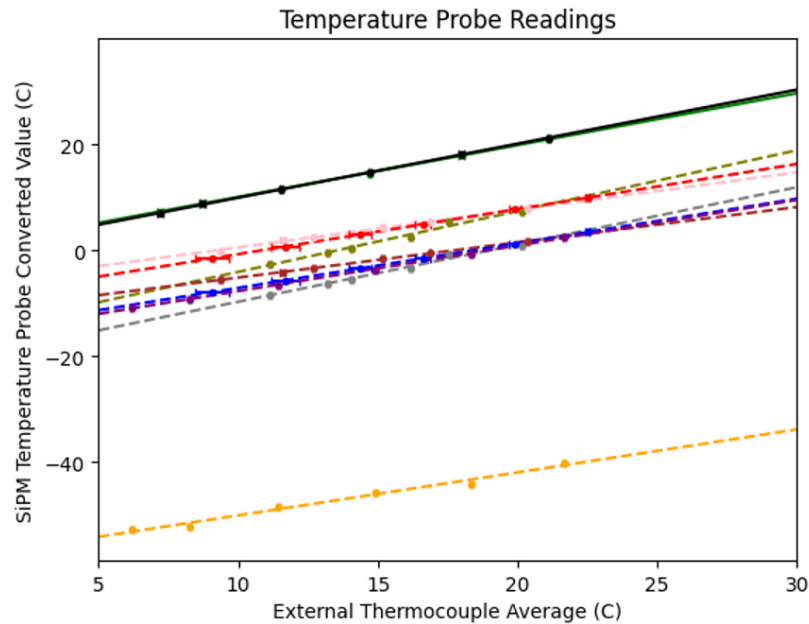
Figure 3.54: Results of calibrating the temperature sensor lines using temperature variations before the firmware update. Different channels are shown in various colors. The solid lines are measured with an external DMM and converted manually.

SiPMs exhibit a significant temperature dependence, both in terms of their noise properties and their breakdown voltages. To properly account and correct for this, the temperature of each SiPM array is measured by two temperature sensors attached to the back of the array. These sensors report the measured temperature through a single voltage line which is then converted to a temperature via a lookup table. When testing these temperature sen-
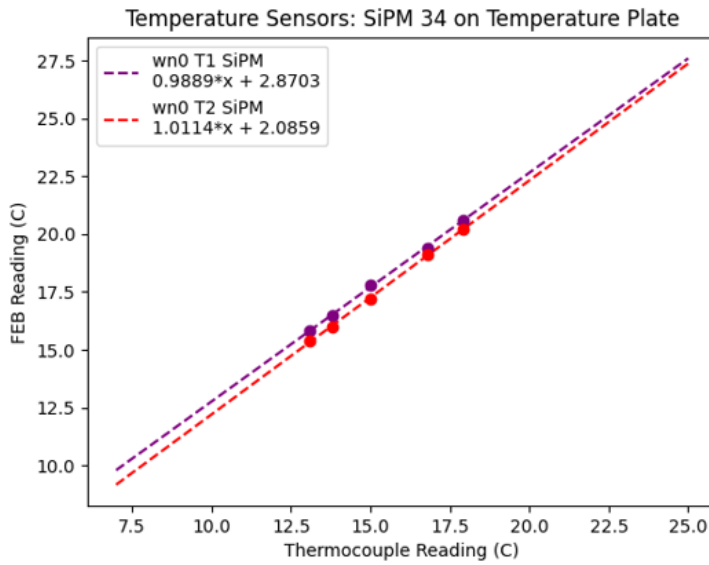
Figure 3.55: Results of calibrating the temperature sensor lines using temperature variations after the firmware update.

sors directly using a digital multimeter I found them to be in agreement with measurements made by an independent thermocouple taped near the sensor, across a range of temperatures expected within the focal plane (0-30 C). However, when performing the same test using the RICH FEB to measure the reported voltage, I found disagreements in both the slope and offset of the measured voltage's temperature dependence. When directly injecting voltages, a discrepancy remained. The issue was eventually found to be that the multiplexer responsible for switching which temperature reading was being digitized was switching between signals faster than the system could achieve equilibrium. By extending the delay between measurements, the temperature discrepancies were removed. A before and after is shown in Figures 3.54 and 3.55.

Zero Suppression

The RICH is relies on zero suppression as a method of reducing data size to manageable levels. For each event, every channel is checked in the firmware to see if the signal is
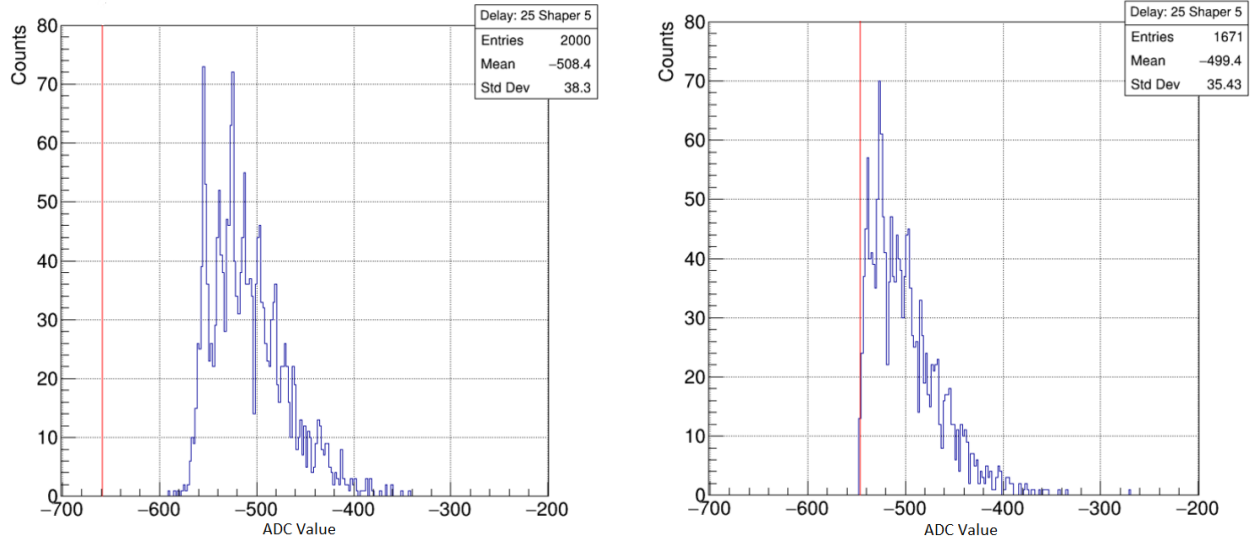
(a) Calibration light spectrum with zero suppression threshold (red line) set below the pedestal.

(b) Calibration light spectrum with zero suppression threshold (red line) set just above the pedestal.

Figure 3.56: Zero suppression testing.

above a set threshold. The data from channels that pass this cut are packaged and sent to the merger, other channels are not recorded to save on space. The threshold for this cut must be set carefully to avoid throwing out valuable data. The original design for the RICH's zero suppression used the fast shaper and internal discriminator output of the citirocs, only recording channels who had pulses from the discriminator coinciding with the event. Although a clean solution in theory, in testing this was found to be an unreliable method. Setting the discriminator threshold at single PE signal levels was impractically difficult to do in an automated way, and so would not be able to be applied to all 12800 channels.

These results prompted the IU and OSU teams to redesign the zero suppression, which I tested and debugged. This new method compares the digitized final values to a preset threshold that can be set for each Citiroc. Pedestal values were found to be grouped closely enough within a single ASIC that a threshold could be chosen at the single PE level of sensitivity. This is demonstrated in Figure 3.56.
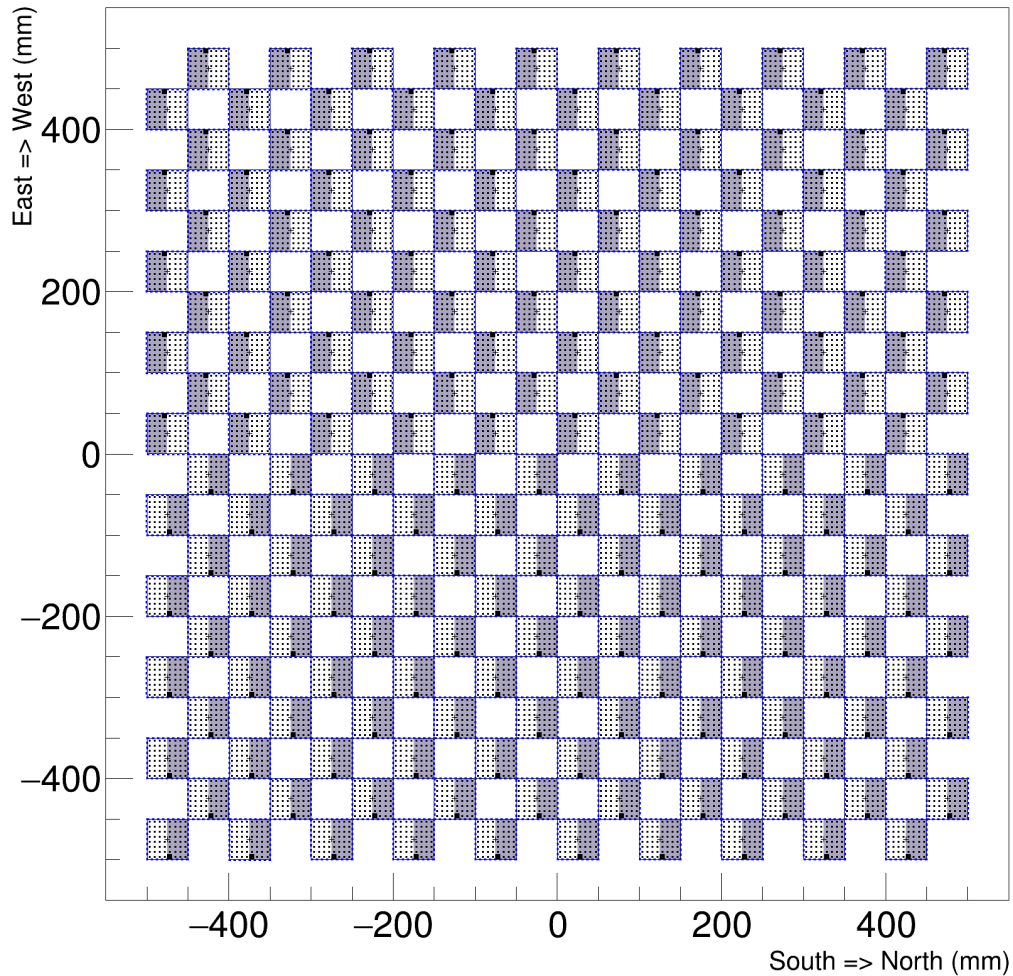
Figure 3.57: The current mapping of the focal plane. The grey and white highlighted section show the sections of each array serviced by each of its two Citirocs. The heavier black dot in each array shows the location of channel 0. Notice that there is a 180 degree rotation of the array between the East and West sides. Plot produced by Scott Wakely.

Focal Plane Mapping

Much like how SiPM channels needed to be mapped to their physical positions within arrays in section 3.3.7, each array needs to be mapped to its position in the RICH focal plane. I produced the initial mapping library, compatible with HELIX's flight software, in C++. The library loaded board information from a configuration file that allow for updates to reflect changes in the RICH's cabling that may occur. The library wrapped multiple layers

of mapping from pixels within the array to array positions on the focal plane to connector position to board ID. The current mapping is demonstrated in Figure 3.57.

3.5.6   Baseline Shift
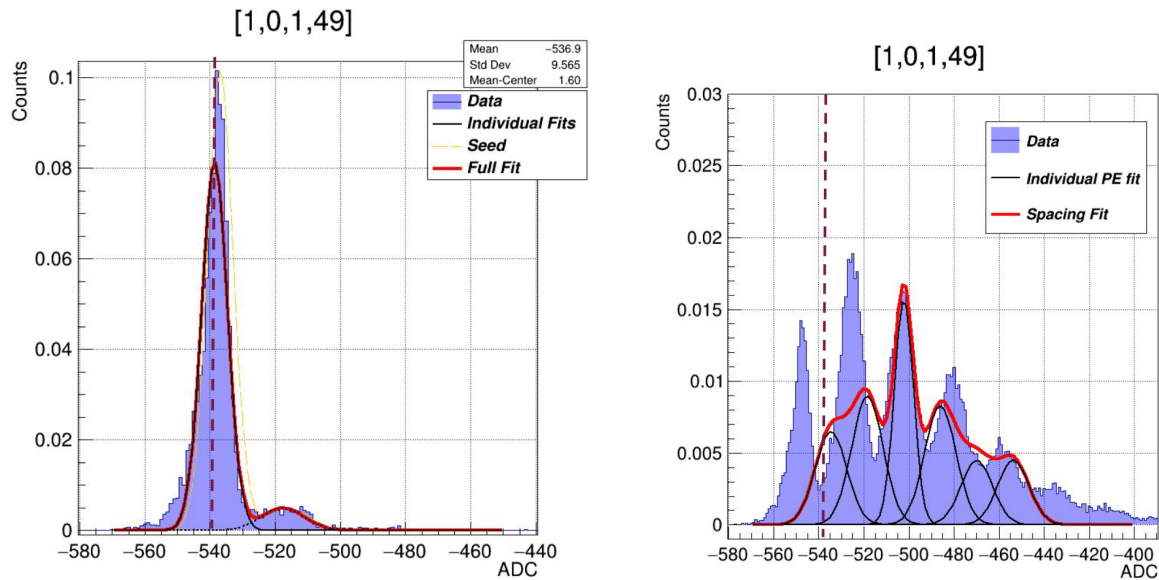
(a) SiPM spectrum with no calibration light.

(b) SiPM spectrum with calibration light

Figure 3.58: The SiPM pedestal shifting location. The vertical dotted line marks the initial pedestal location. The fits are for an early development peak fitting algorithm and not relevant here.

During early development of a peak finding algorithm (discussed in section 3.7.2), I discovered that the apparent location of the pedestal for the SiPM spectrum of a channel would change depending on whether calibration light was being applied to the array (Figure 3.58). Since the calibration flashes were pulsed with a period orders of magnitude longer than the recovery time of a SiPM, it was highly unlikely to be due to any hysteresis. Notably, this pedestal shift was not detected when using the LED flasher and fiber positioned. Together, this suggested that the issue was some form of noise between channels on the same array which was dubbed either "baseline shift" or "negative crosstalk" depending on nomenclature preferences for crosstalk.
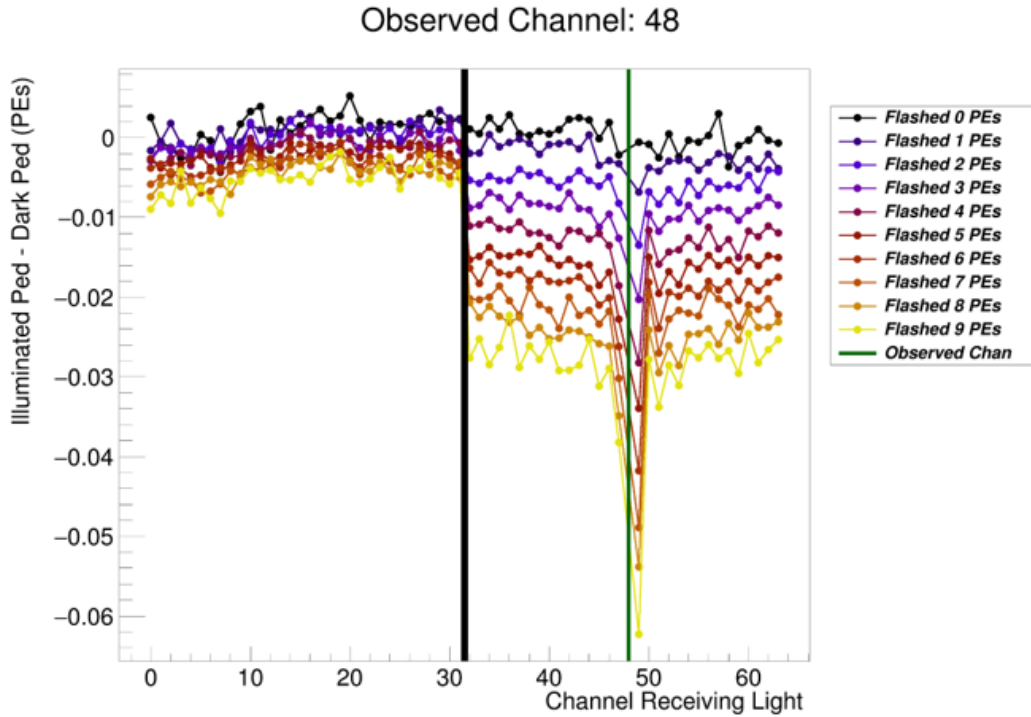
Figure 3.59: Each data point in this plot shows the amount by which the pedestal shifted in the observed channel in response to the indicated channel receiving light. The observed channel is indicated by the vertical green line. Channels 0-31 and channels 32-63 share a Citiroc.

Initial tests of the baseline shift used physical masks applied to the array to vary detected light levels. Once this physical method established that the baseline shift was real, I switched to lowering the voltage on selected channels below the breakdown voltage to "turn off" the SiPMs. This second method allowed for different "virtual masks" to be applied quickly for testing. This was the method used to produce Figures 3.59 and 3.60. These plots demonstrate that the baseline shift in a channel is proportional to the signal received in nearby channels, with the signal to shift ratio falling into three categories depending on the relationship between channels.

- Channels that shared an array and not a citiroc, experiencing a crosstalk of ∼-0.1%.

- Channels that shared an array and a citiroc but were not "paired", experiencing a crosstalk of ∼-0.1%.

94
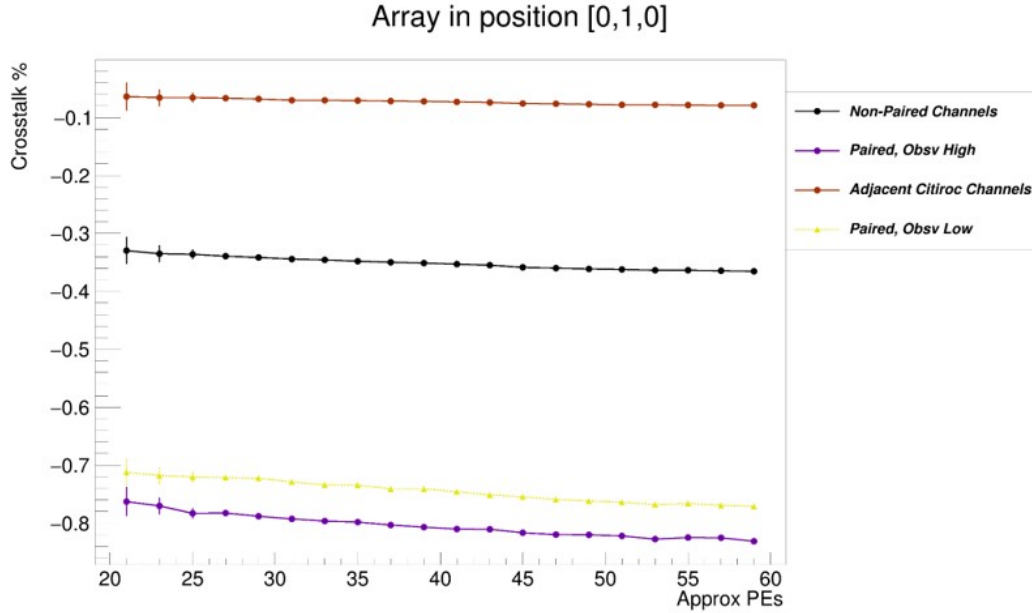
Figure 3.60: The average baseline shift crosstalk values, grouped by relationships between channels. "Observed high" and "observed low" are subgroups of paired channels, separated by whether or not the channel experiencing the crosstalk is the higher number of the pair.

- "Paired" channels, experiencing a crosstalk of ∼-0.1%. Paired channels were grouped by (n,n+1) for even values of n.

Making the same measurement again with a shorter SiPM cable results in a significant reduction in the crosstalk fraction in paired channels, shown in Figure 3.61. This reduction, along with the fact that paired channels run parallel to each other on opposite sides of the flex cable (Figure 3.62), suggest that at least some of the baseline shift occurs due to noise within the SiPM cables. However, since the cables are prohibitively difficult to replace a software-level mitigation is required.

With these results, I created a simple per-event linear algebra solution. By creating a 64 × 64 matrix of crosstalk ratios between channels in an array, the function *NormalEqn* from ROOT's *TDecompChol* library can be used to find the most likely true signal values from what was measured.
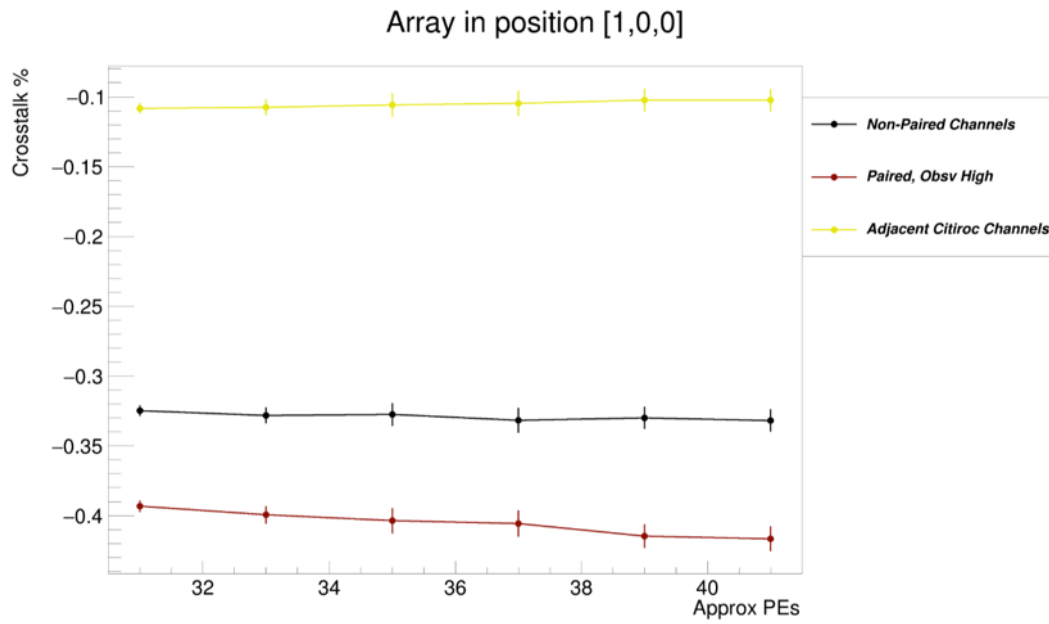
Figure 3.61: The average baseline shift crosstalk values, grouped by relationships between channels. A shorter SiPM cable was used.
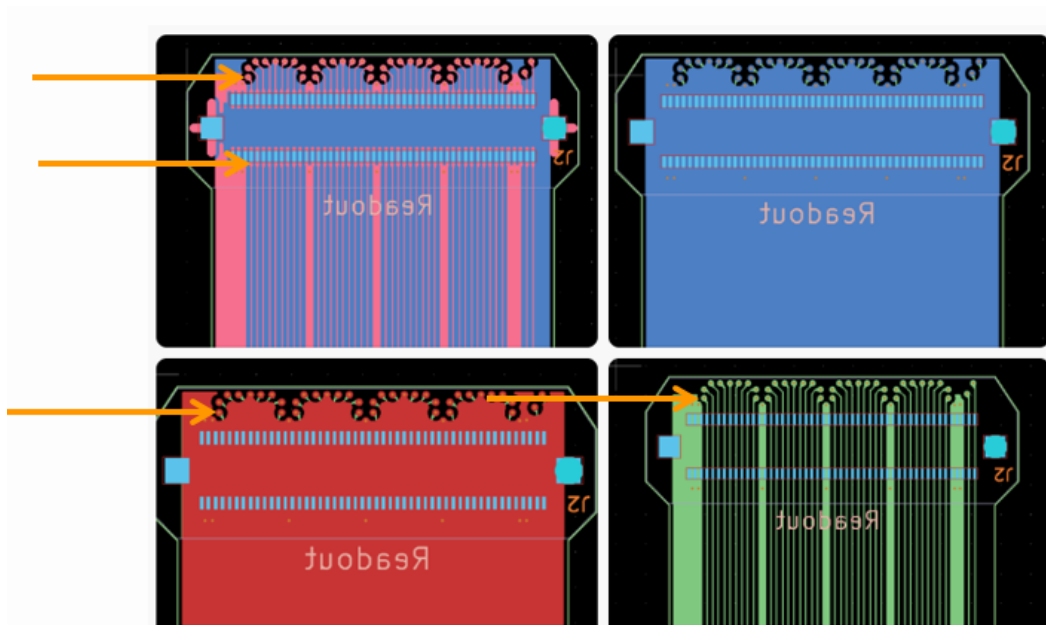
Figure 3.62: Gerber files for the SiPM cables, with a set of "paired" channels indicated.
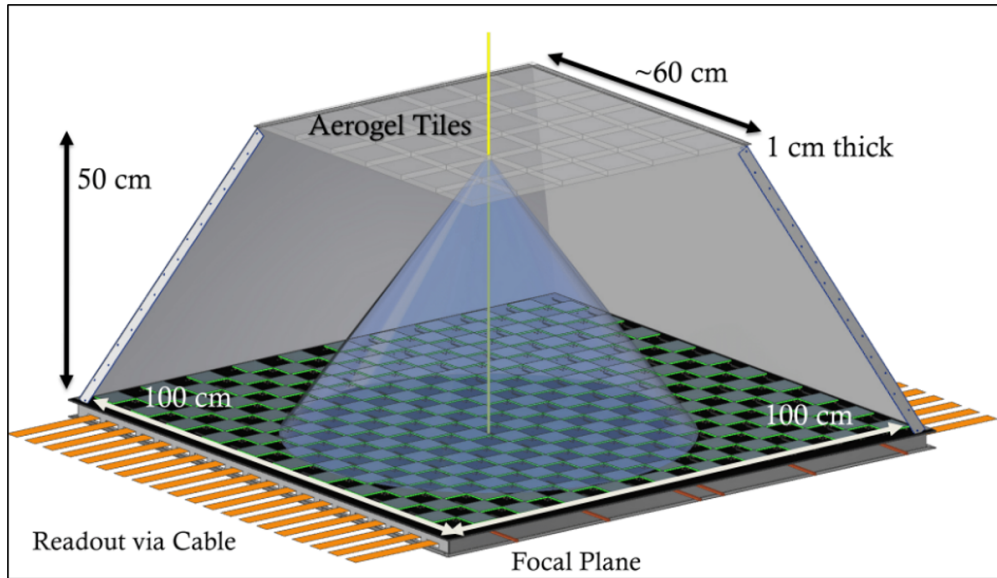
Figure 3.63: HELIX's RICH design.

3.6 RICH and Focal Plane Assembly

3.6.1 Construction

The RICH was assembled in the early winter of 2021. The body of the RICH is primarily made of aluminum, and as shown in Figure 3.63 it consists of three main sections: the aerogel radiator and tray, the light-tight cone, and the focal plane. The cone's four sides are riveted to struts along the four slanted edges and it attaches to the focal plane via screws around the bottom edge. The square opening at the top is rigid with slotted edges to allow the aerogel tray to slide in and out. The RICH's focal plane is hollow; SiPM arrays are attached to the top layer with screws and cables are routed through the interior and out the East and West sides. The thin top layer is held in place around the perimeter with screws and in the middle by an array of standoffs attached to the bottom layer with adhesive and to the top layer with removable bolts.

The construction of the focal plane was a delicate process, as 200 SiPM arrays needed to be aligned, mounted, and cabled while the focal plane was held vertical by a jig to allow

97

Figure 3.64: The focal plane immediately after populating it with SiPM arrays. The plane was held in place vertically by a custom mount, as the arrays are attached via screws placed through holes on the back side.

access to both sides. The person on the backside of the focal plane would weave the cable into place, then the person in the front would attach the SiPM array to the cable and align it while the person at the back would screw it into place. A third person would then record the array position and the serial numbers of the array and cable. The finished result of this focal plane population is shown in Figures 3.64 and 3.65. When all 200 arrays were in place, the bottom of the focal plane was reattached, and the standoffs were carefully reattached via bolts now underneath the arrays.

Once completed, the focal plane was returned to resting with it's bottom on the table. The cone and aerogel tray were attached by bolts around the edges. I light-tightened the SiPM cables by packing the edges of the focal plane where they emerged with opaque black foam, and securing the foam, cables, and four spooled air hoses with black foil tape (Figure

Figure 3.65: A view from the back of the focal plane immediately after population. SiPM cables were run on the opposite side of the focal plane and held in place during construction by a wire mesh and zip ties.

3.66). Later, I tested the light-tightness of the RICH by measuring the SiPM noise levels while moving a flashlight across the seams of the assembly. Any locations where the flashlight caused an increase in noise were covered in additional material until no effect was found. Figure 3.67 shows the inside of the RICH after assembly.

Once the RICH was assembled and the design finalized, the cone was temporarily removed to allow the focal plane to be 3D mapped with the use of a HandySCAN 3D laser scanner. This process produces a 3D map of the focal plane to sub-mm precision. The process of this scanning and its result are shown in Figure 3.68.

Figure 3.66: The SiPM cables emerging from the edge of the focal plane after light-tightening.

3.6.2 Calibration Flashers

I designed a calibration flasher system to install in the RICH for testing and calibrating the SiPM channels in their final configuration. Having the capacity to test the SiPMs and focal plane in situ allows for characterizing the system with both SiPM channels paired to the electronics that will be used in flight. Additionally, it is the only practical way of testing all channels simultaneously, as any test bench capable of supporting all 12800 channels would be equally as complex as the RICH itself.

Requirements for the calibration flashers included the ability to illuminate the whole focal plane, pulse durations around 10 ns or less, and a minimal profile to prevent any interference with the operation of the RICH. These requirements informed my choice of a Thorlabs NPL41BNanosecond Pulsed Laser Diode System as the light source. The light is delivered to the RICH via fiber optic cables, and diffused within the RICH cone using Thorlabs fiber optic cannulas with diffuser tips designed for medical imaging. These cannulas diffuse light

100
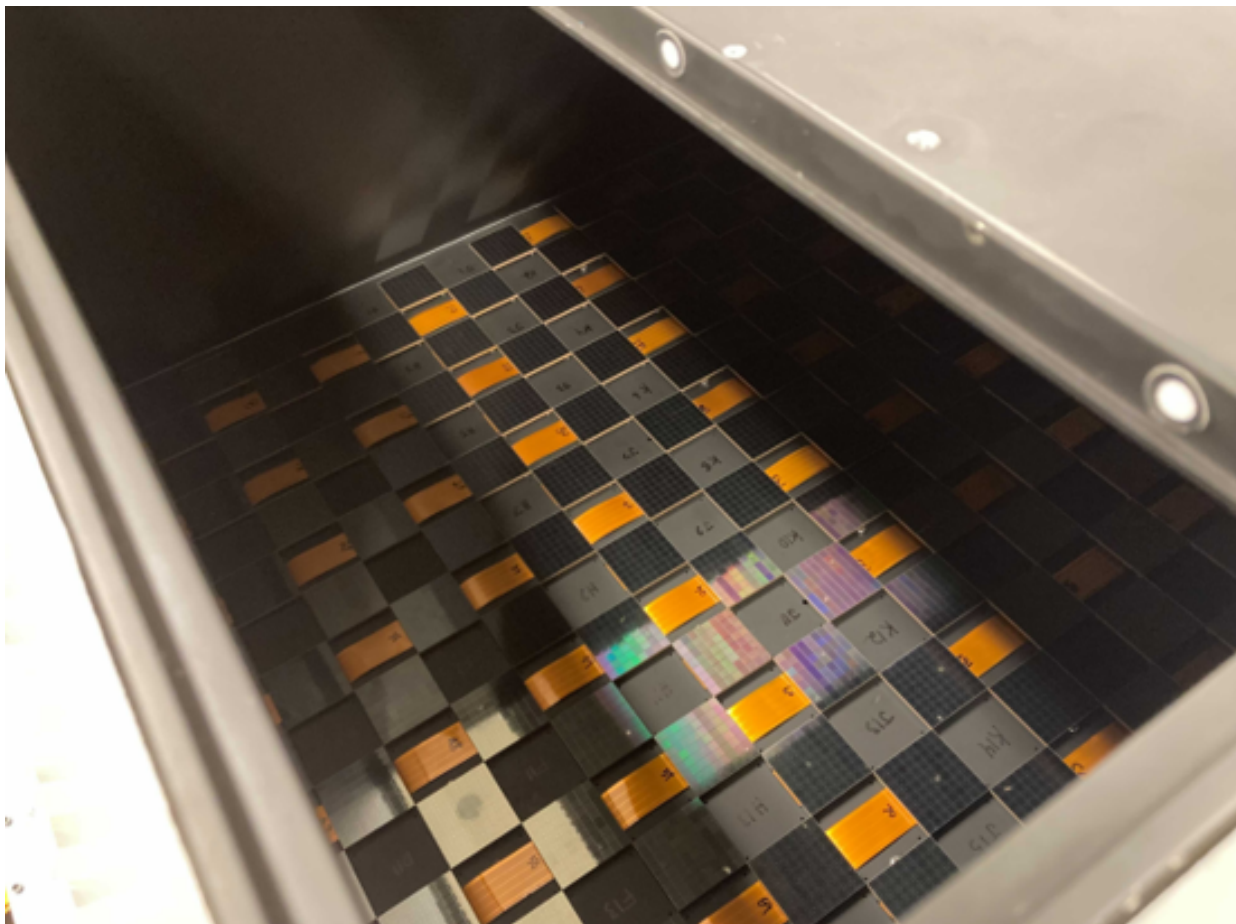
Figure 3.67: A view into the RICH with the aerogel tray partially pulled back.

in a nearly isotropic pattern up to 90 degrees from the direction of the fiber and are only about 0.2 mm in diameter, making them extraordinarily well suited for this purpose. I designed 3D printed mounts to hold the flasher assemblies in position perpendicular to the sides of the RICH cone, with only the fiber cannulas themselves entering the inside of the RICH through millimeter diameter holes. The assemblies and mounts are shown in Figure 3.69.

Each of four equally sized quadrants is assigned to a flasher position, to allow adequate light to be available at all locations. Prior to the installation of the RICH, I used a single spare RICH FEB to measure a sample of arrays in the focal plane to check the effectiveness of the calibration flasher system. The results of this early test are shown in Figure 3.70.

101
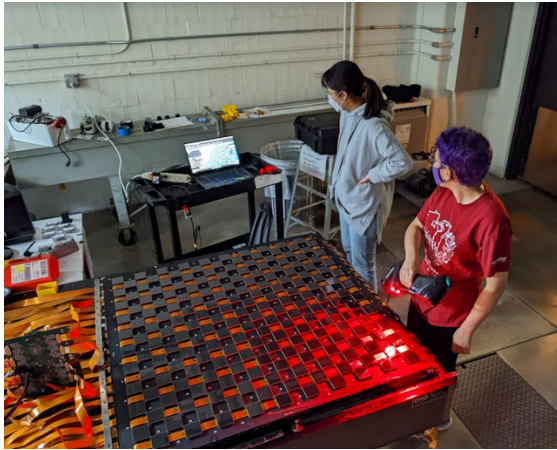
(a) Hyebin Jeon and Julia Tuttle in the processes of 3D scanning the focal plane.
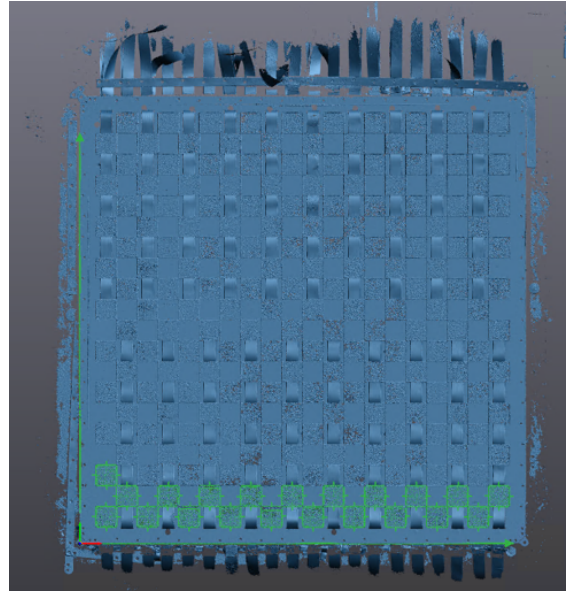
(b) The point cloud created by the 3D laser scanner.

Figure 3.68: 3D mapping of the HELIX focal plane.

When performing calibrations, the laser is connected to one quadrant at a time to maximize the amount of calibration light available to each channel. During analysis, "composite" focal planes are stitched together from data taken at the four different focal plane quadrants, as demonstrated in Figure 3.71.

3.6.3 Installation

After the calibration system was shown to work, the completed RICH was installed into HEILX's payload. Installation of the RICH detector requires care and patience, but is ultimately a straightforward process. The RICH itself is designed to be modular, and is held in position within the payload by four bolts attached to struts holding each corner of the focal plane. Once put in place, all 200 SiPM cables must be carefully routed to their designated connectors on the RICH FEBs. This process is shown in Figure 3.72.
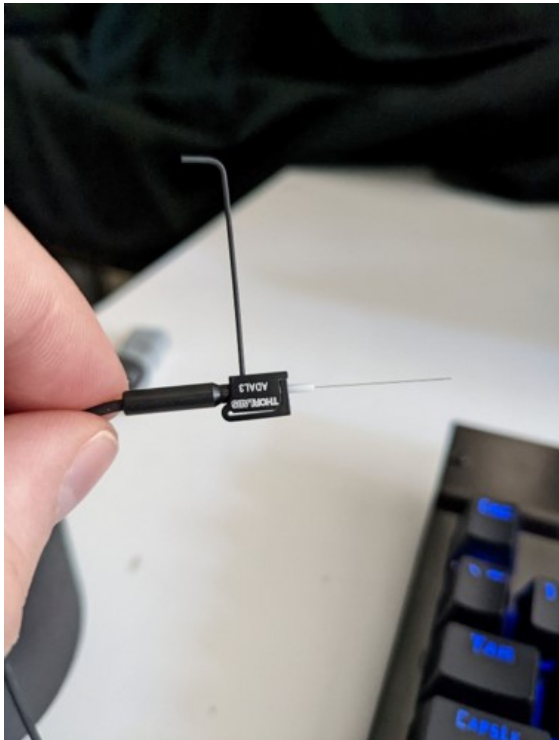
(a) A calibration flasher assembly. From left to right: Fiber optic cable, interconnect with a hex key indicating the set screw position, and fiber optic cannulae with diffuser tip.
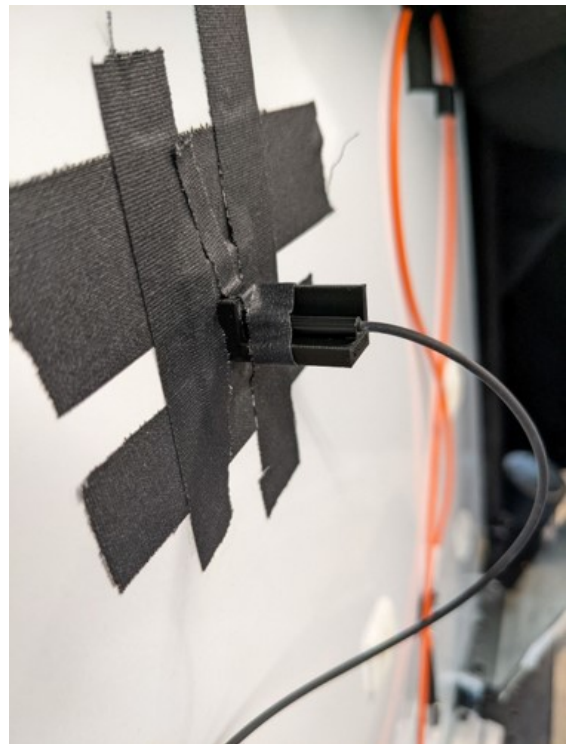
(b) The calibration flasher assembly installed into the side of the focal plane. The black bracket is my custom designed 3D print.

Figure 3.69: One calibration flasher.
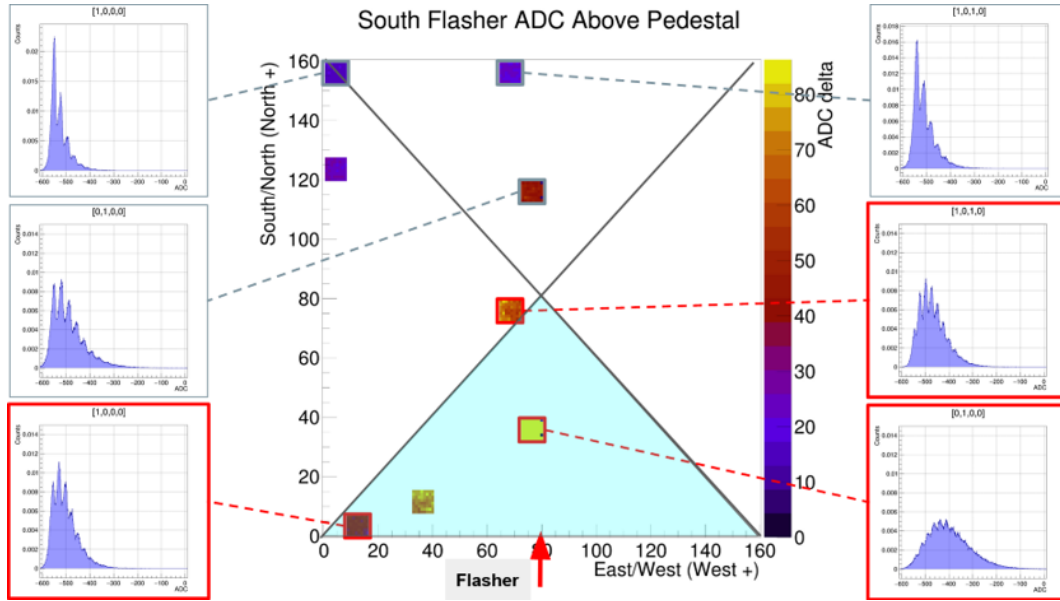
Figure 3.70: An early test of the calibration flasher before installing the RICH in the payload. The red arrow shows the approximate location of the calibration flasher. The 8 sampled arrays were attached to a spare RICH FEB. Each spectrum is for one channel in the indicated array, channels outlined in red are within the quadrant serviced by the installed flasher.
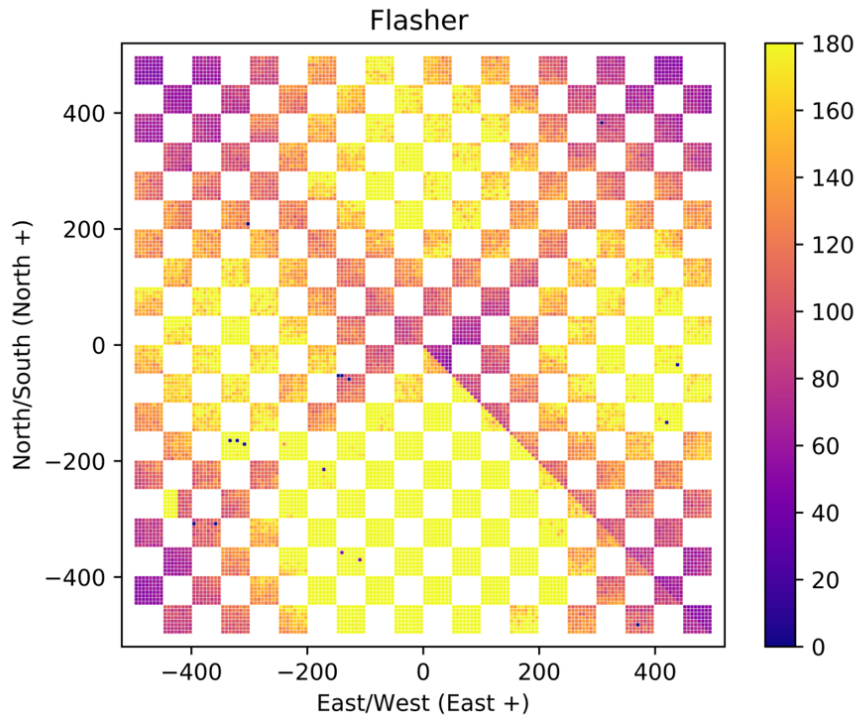
Figure 3.71: An example of a composite focal plane used in calibration.

(a) The RICH immediately after installation, before cabling.

(b) A view of the RICH boards, partially cabled.

Figure 3.72: HELIX's RICH installed in the payload.

3.7 Focal Plane Calibration

3.7.1 Calibration Toy Monte Carlo

HELIX's focal plane contains 12,800 channels: a quick calculation shows that even a 10 second process applied to every channel would take over 35 hours to complete. This means that any analysis tools I develop for the RICH needs to operate with significant automation, since human oversight for each and every channel would be extremely burdensome. Therefore, tools are needed to verify that any tool used to calibrate RICH channels both performs within tight tolerances and is able to flag any issues or outliers for further investigation.
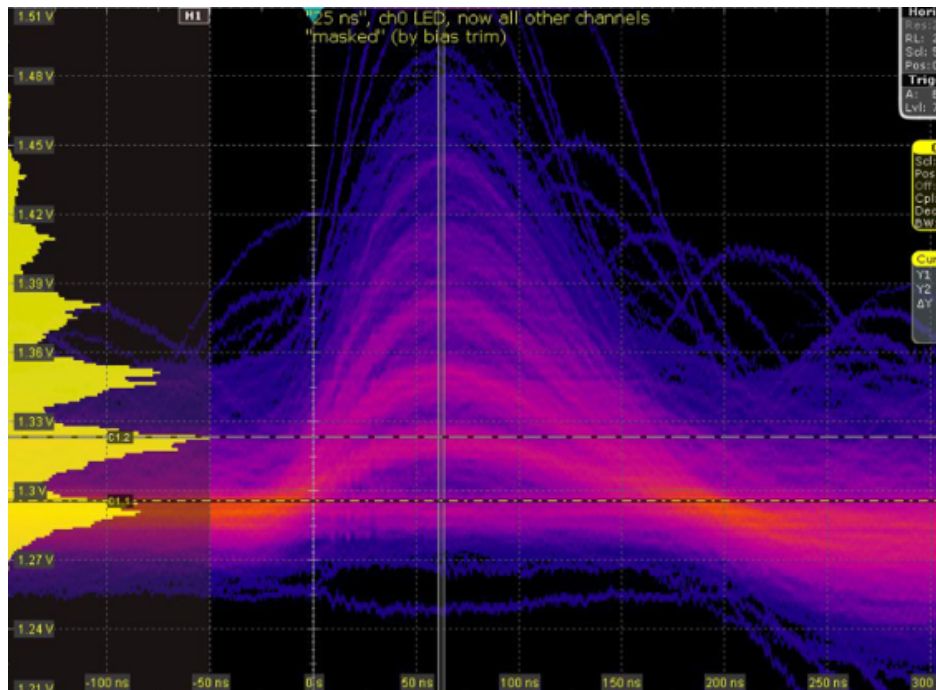
Figure 3.73: Shaped and amplified SiPM pulses, extracted from the RICH FEB via a soldered probe and oscilloscope.

Toy Monte Carlos (MCs) are ideal for testing analysis tools in a control environment to verify that they are behaving as expected. I developed a toy MC to simulate the full RICH readout chain from SiPM to final data storage for use in testing my analysis tools during development. The MC is informed by actual measurements of the SiPM and front
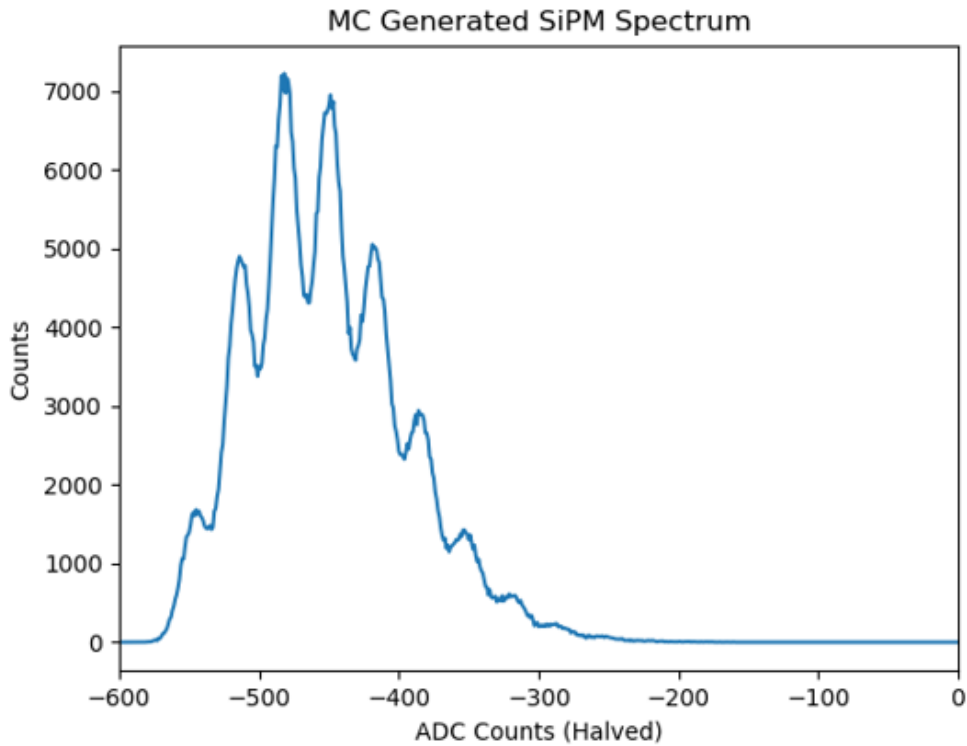
Figure 3.74: One channel's SiPM calibration spectrum, generated from my toy MC.

end electronics at each stage.

Channel properties such as gain as a function of bias voltage above breakdown, the breakdown voltage, the temperature dependence, pedestal value, and whether a channel is disconnected are selected from distributions fit to prior measurements and preserved per channel. For each channel in each event, a number of detected PEs is selected from a Poisson distribution. The PDE is already accounted for since the mean of Poisson distribution is informed by actual focal plane data. A quadratic function is used to approximate a shaped SiPM pulse using the number of detected PEs and channel gain to set the vertex and of the channel to set the zero crossings. The shaped pulse measurements used to inform the MC are shown in Figure 3.73.

Once the shaped pulse for the channel and event is selected, the sample and hold operation is simulated by selecting a timing jitter from a Gaussian distribution with a width chosen

107

from the study outlined in section 3.3.6. This selected jitter is then used with the quadratic approximation to find the signal value. Gaussian noise characteristic of the set temperature is then added to each signal value. Finally, this value is added to the channel's pedestal value.

The MC is run under a range of initial conditions such as bias voltages and light levels. The final measured spectrum for each channel is recorded along with the truth values of the underlying distributions. An example of a generated spectrum is shown in Figure 3.74. Comparison between the results of my analysis tools and the truth values from my MC were used to build trust in calibration procedures before using them for the payload.

3.7.2   Gain Matching Procedure

Peak Finding

I created, tested, and refined many iterations of the peak finding procedure for HELIX's SiPMs. I developed the first version of the gain matching program in ROOT, followed by a version using Python and scipy's *find_peaks_cwt* function. The version presented here, developed in Python, performed the most reliably on MC data and required the least number of assumptions about the peak properties. It uses a Savitzky-Golay filter to smooth the data and scipy's *find_peaks* function to produce the initial set of peaks (local maximums) under examination.

Once an initial set of peaks is found, the distribution is reversed vertically and the same process applied to find the valleys (local minimums). The program then begins a series of quality checks on the distribution, flagging the distribution as unreliable if not all the conditions are met. The requirement is that the distribution contain a minimum number of peak candidates. From these candidates, only peaks above a fraction of the maximum peak's height are kept. Next I check the "prominence" of the peaks by comparing their total height to the vertical distance of the neighboring valleys, the peak passes if that vertical
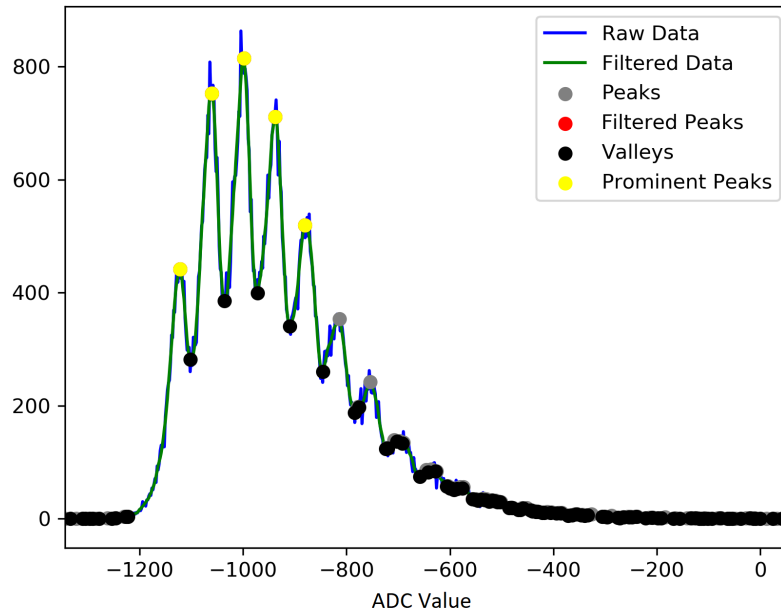
Figure 3.75: An example of real data processed by my gain matching procedure. The grey dots are peaks that didn't pass the height requirement, red dots would be peaks that passed the height requirement but not the prominence requirement (none present), and yellow dots are the final accepted peaks used to calculate the gain.

distance exceeds a set fraction of the peak's total height. With only the prominent peaks left, I take the mean spacing between neighboring peaks and require that no individual spacing deviates from the mean spacing by more than 20%. With all checks passed, the mean spacing is reported as the gain, in units of ADC/PE. An example of this procedure is shown in Figure 3.75. Examples of results flagged as unreliable are showin in Figures 3.76 and 3.77.

Gain Slope and Matching

With the peak finding procedure in place, the next step is to find the relationship between the applied voltage and the extracted gain per-channel. This is done by taking calibration data from the flashers across a range of voltages, extracting gain from each set of data using
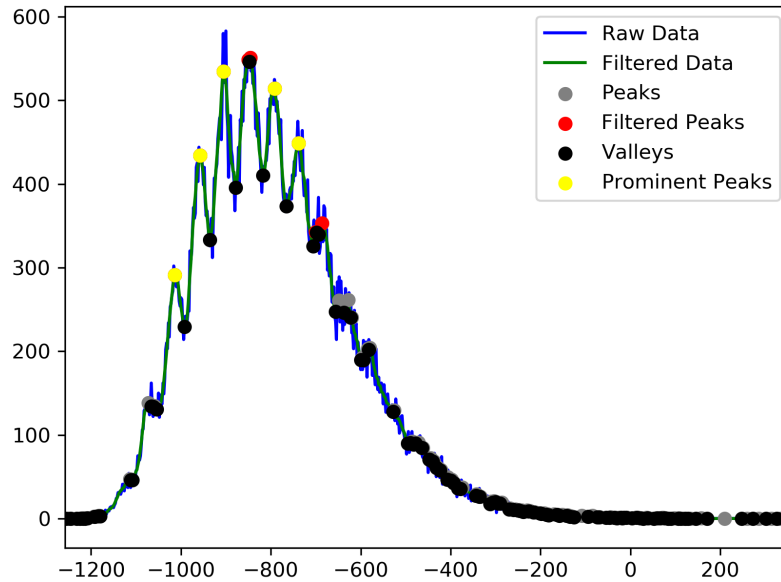
Figure 3.76: An example of real data flagged as unreliable by my gain matching procedure. Higher than desired noise in the data resulted in single peaks being flagged multiple times, which was detected by the peak prominence cut.

the peak finder, and fitting the results to a linear function. An example of this is show in in Figure 3.78. Quality checks at this stage sort the channels into three categories: working channels, unreliable channels who either have too few viable points or don't fit well to a linear function, and disconnected channels. With the linear fits in hand, gain matching can be achieved by selecting desired ADC/PE gain and reversing the functions to find the applied voltage required per-channel.

As discussed in section 3.5, the bias voltage across each channel is determined by two values: the cathode voltage shared by each array, and the anode "trim" voltage applied to each channel's anode. Therefore, there are two methods of scanning the bias voltage in the procedure above. Since each of the many thousands of DACs providing the voltages have their own individual response, it is wise to incorporate these responses into the gain matching procedure by performing it twice, and using the results of each the cathode and anode gain

110
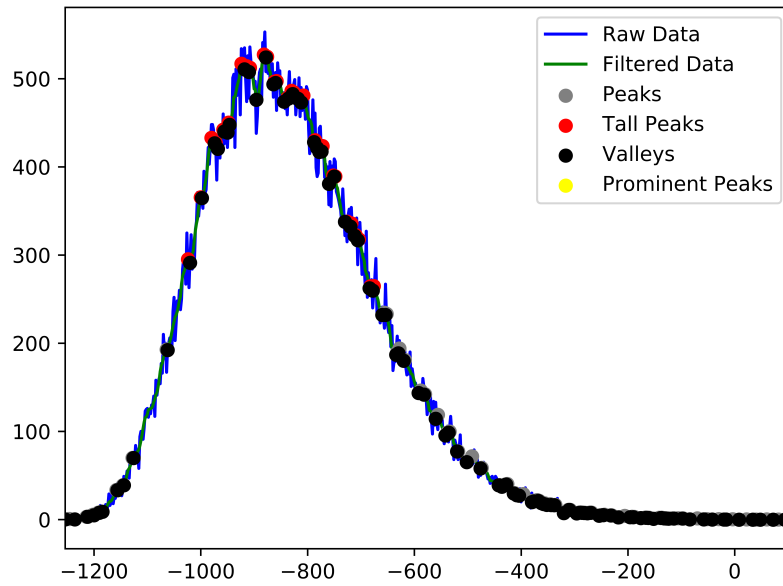
Figure 3.77: An example of real data flagged as unreliable by my gain matching procedure. Extreme noise led to no viable peaks being detected.
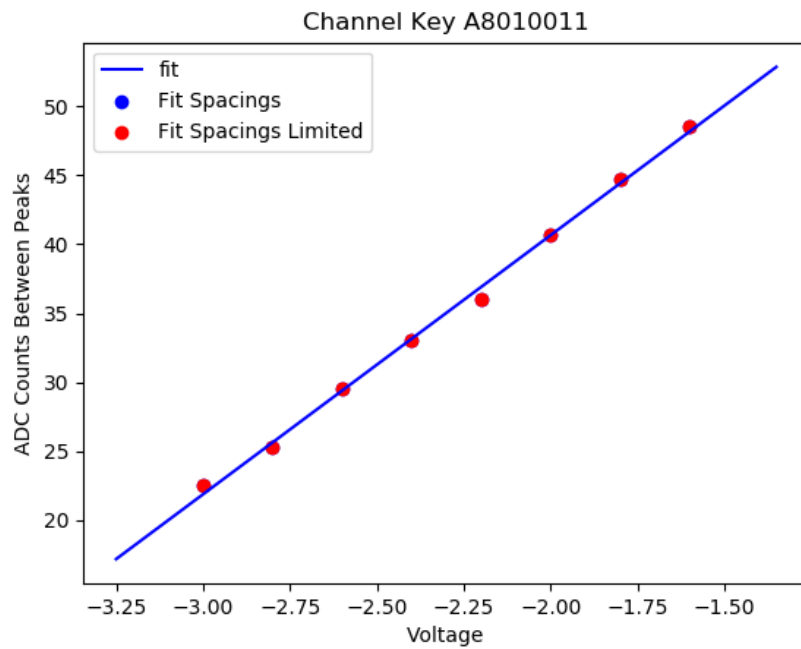
Figure 3.78: A linear fit to gain vs bias voltage using real calibration data.

111

slopes when adjusting their respective voltages. First, the cathodes are scanned and the results are used to determine the maximum required voltage per array. Each cathode is then set to that maximum value, and the anodes are similarly scanned. The anode results are used to match the gains of individual channels. Once matched, adjustments to account for temperature variations are done with the more reliable cathode DACs.

3.7.3 Gain Matching Results

Temperature Dependence

Figure 3.79: A SiPM array on a temperature controlled plate for testing. The black box above is placed over the array and a fiber optic cable is fed through the top to flash calibration light on the array.

As earlier discussed, the primary vector through which the SiPM temperature affects gain is via the breakdown voltage's linear temperature dependence. As the temperature rises the breakdown voltage rises as well, lowering the operating voltage's distance above the breakdown voltage and thereby the lowering the gain. This temperature dependence can be adjusted for live and in place by adjusting the operating voltage of each channel in

Channel [1,0,0,0]
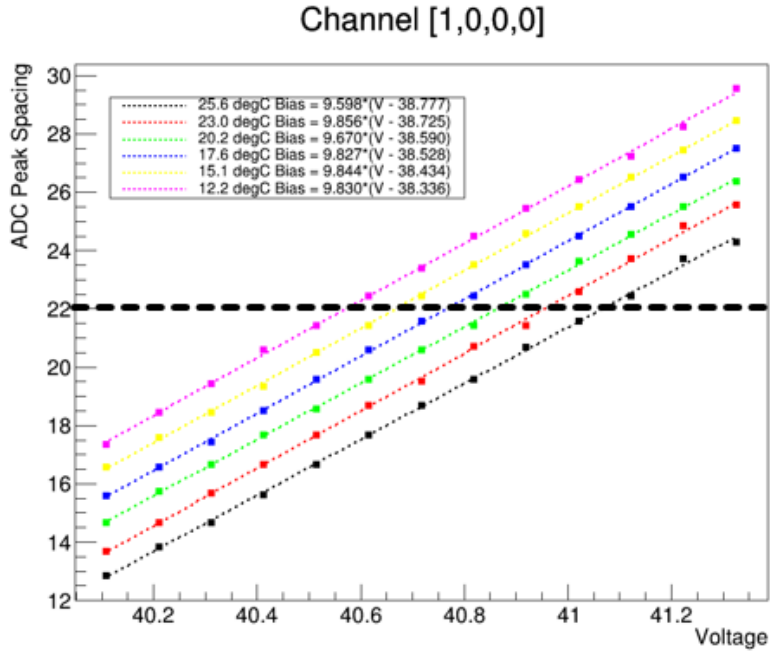
Figure 3.80: The gain slopes and their linear fits for six temperature environments. The dotted black line shows the gain the channels were to be matched to.

Channel [1,0,0,0]
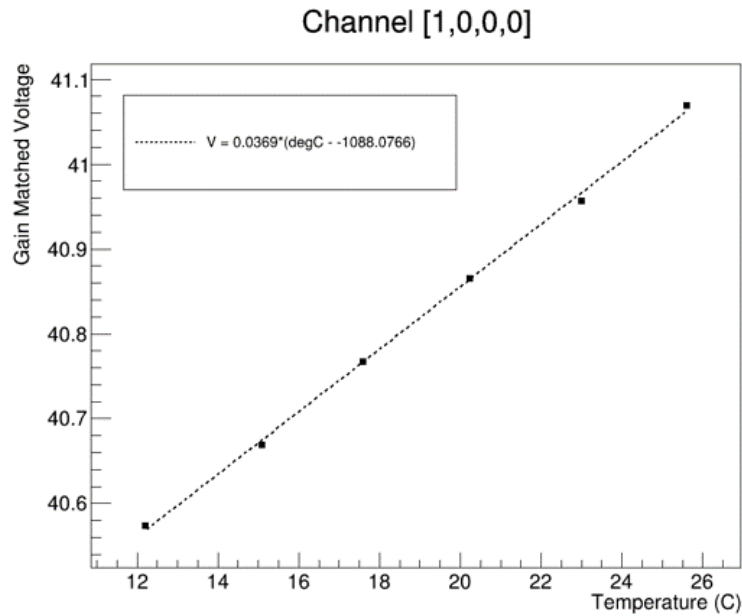
Figure 3.81: The voltages required to gain match the SiPM as a function of temperature.

response to temperature changes. Since each SiPM array has two temperature sensors built in, the difficulty arises only in knowing the conversion from temperature change to voltage

113
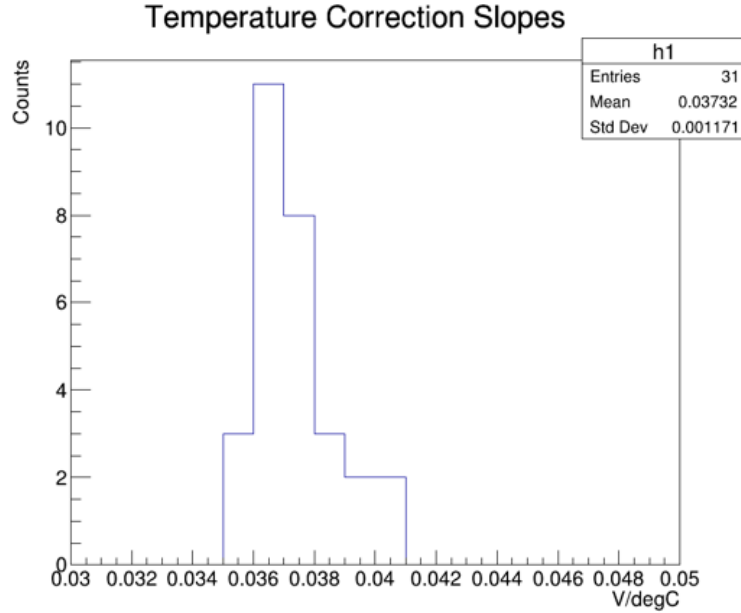
Figure 3.82: The distribution of slopes relating the gain matched operating voltage to the SiPM temperature.

change. An average value for the SiPMs was reported by the manufacturer, but to maximize performance it is desirable to make an independent measurement of each channel's individual temperature dependence.

Early versions of the gain matching procedure were used to test a procedure for determining each channel's temperature dependence. This was done by placing SiPM arrays on a temperature controlled plate and applying the gain matching procedure at a range of temperatures, shown in Figure 3.79. An example of gain slopes from this test are show in Figure 3.80, and a linear fit between the temperature and the required voltage for the same channel is show in Figure 3.81. A distribution of measured gain matched voltage vs temperature slopes is shown in Figure 3.82. Although near the manufacturer reported value of 34 mV/C, the mean was found to be 37 mV/C with a non-negligible standard deviation of 1 mV/C.

By varying the temperature of the focal plane during calibration, this procedure can be repeated for every SiPM channel thereby determining the per-channel temperature correction function for each bias voltage.

Noise Detection
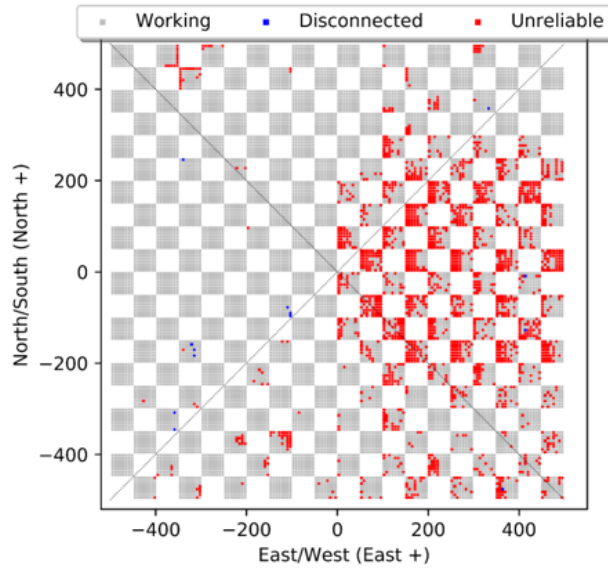
Figure 3.83: A map of the focal plane. Channel in red are showing channels experiencing too much noise to properly gain match.

(a) The unshielded merger placed in the middle of the RICH boards.
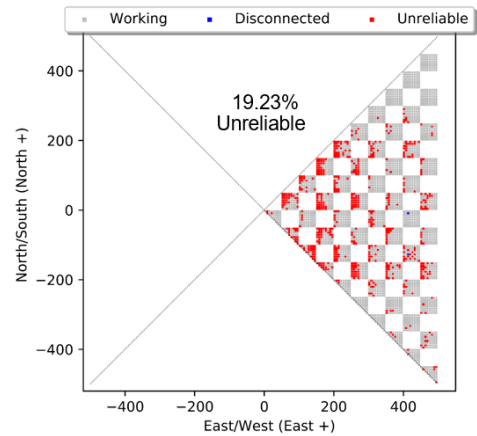
(b) A map of unreliable channels in the focal plane. Only the East quadrant was measured.

Figure 3.84: Normal merger configuration.

In addition to the unreliable channel detection feature role in preventing hidden mis-biasing of SiPMs, it also serves as an excellent tool for detecting sources of noise. For

(a) The shielded merger placed in the middle of the RICH boards.
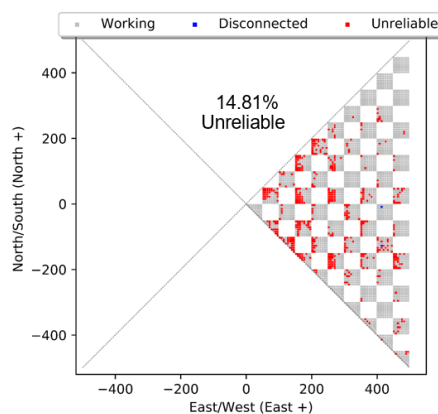
(b) A map of unreliable channels in the focal plane. Only the East quadrant was measured.

Figure 3.85: Shielded merger configuration.
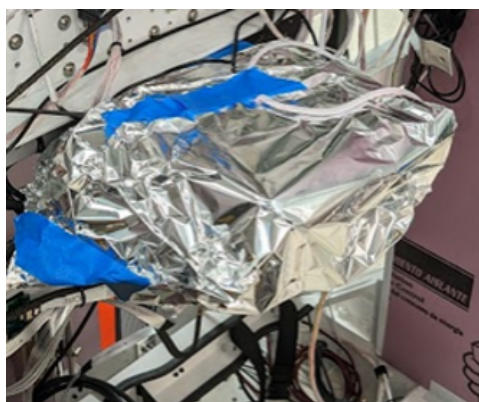
(a) The shielded merger placed approximately a meter away from the middle of the RICH boards.
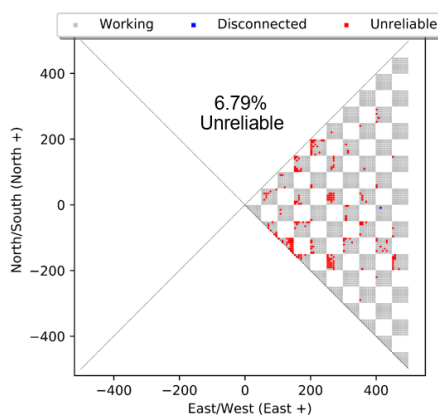
(b) A map of unreliable channels in the focal plane. Only the East quadrant was measured.

Figure 3.86: Shielded and moved to a distance merger configuration.

example, in one instance a change in $\sim$5 degrees C in the lab was detected by in an increase in the percentage of channels tagged as unreliable from 3.8% to 32.3%.

This feature was used most recently in locating a source of electronics noise detected on one side of the payload (see Figure 3.83). The location of the noise within the focal plane correlated with channels serviced by RICH boards that were in proximity to the RICH

merger board. A series of further calibration runs with different mitigation measures in place served as further evidence that the presence of the merger board was a cause of increased noise. Figures 3.84, 3.85, and 3.86 show the improvement in the fraction of reliable channels as more mitigation measures were added.

First Full Gain Matching Results

A design consideration of my SiPM analysis tools was for them to be operable by scientists other than myself. As I am reaching the end of my time in graduate school, it is critical that others be able to perform these calibrations.

Fortunately, the first full focal plane gain matching calibration using my program was successfully completed by Dr. Kenichi Sakai, with minimal input from myself beyond initial demonstrations and instructions. Figure 3.87 shows the result of the gain matching.
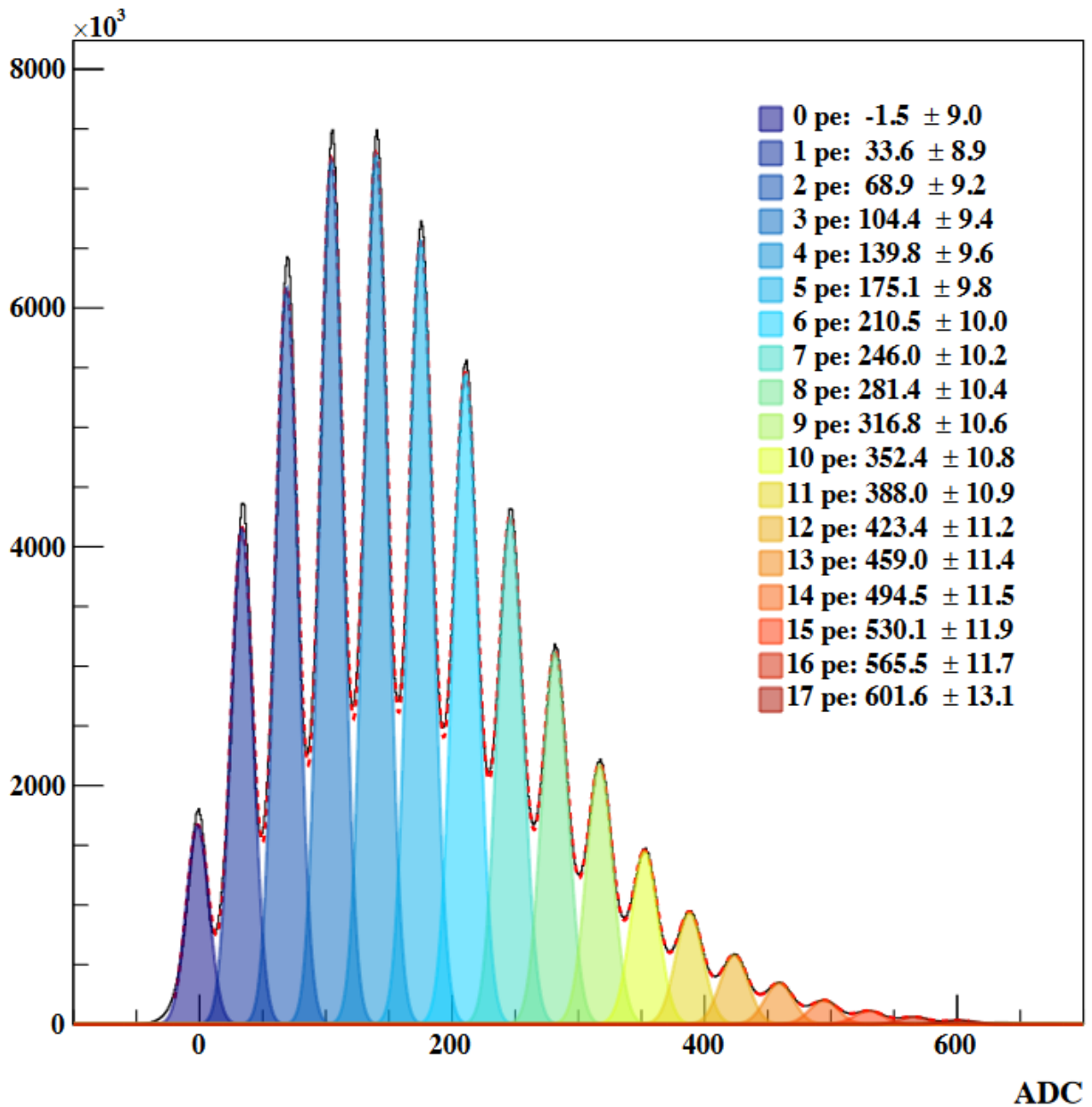
Figure 3.87: All ~ 12,800 SiPM channels spectra histograms summed together after gain matching. Each channel has had its pedestal adjusted to align with an ADC value of 0. Plot made by Kenichi Sakai.

CHAPTER 4

CONCLUSIONS

My work, outlined in this thesis, took the RICH detector from its early design stages through to full operability and integration into HELIX's payload. My work began with initial characterizations of Silicon Photomultipliers for use in the RICH's focal plane, demonstrating their suitability for HELIX's needs. I then characterized the performance of scintillating fiber ribbons for use in constructing HEILX's hodoscope. I next tested, debugged, and implemented the control and data acquisition electronics used in HELIX's RICH and hodoscope.

With all these components developed, I then led the assembly of the RICH detector's mechanical and electrical components. Next, I characterized the performance of the detector separately from the payload, including the designing an unobtrusive in-situ calibration system. Along with the rest of the University of Chicago HELIX group and some assistance from external collaborators, I installed the RICH into the payload. Finally, using the final configuration of the RICH and supporting electronics I led the testing and calibration of the detector, showing that the focal plane would perform as required to achieve HELIX's scientific goals.

In this thesis I have also outlined the scientific value of developing this detector, demonstrating through simulation and analysis how its design is optimized for achieving the velocity resolution needed for high energy measurements of cosmic-ray isotope ratios in the challenging environment of a balloon experiment. This analysis also showed the value of a HELIX's RICH detector in respect to its support of upgrades for future flights.

At time of writing, HELIX is on track to launch in Spring of 2024 from Kiruna, Sweden in a northern-hemisphere flight. During this flight, HELIX will measure the isotopic composition of light cosmic rays up to ~ 3 GeV/n, at a resolution capable of 4σ mass separation between adjacent peaks. After HELIX completes this initial flight, planned upgrades will begin on the payload to increase the sensitivity range of future flights up to ~ 10 GeV/n.

REFERENCES

M. G. Aartsen, M. Ackermann, J. Adams, J. A. Aguilar, M. Ahlers, M. Ahrens, C. Alispach, K. Andeen, T. Anderson, I. Ansseau, G. Anton, C. Argüelles, J. Auffenberg, S. Axani, P. Backes, H. Bagherpour, X. Bai, A. Barbano, S. W. Barwick, V. Baum, S. Baur, R. Bay, J. J. Beatty, K.-H. Becker, J. Becker Tjus, S. BenZvi, D. Berley, E. Bernardini, D. Z. Besson, G. Binder, D. Bindig, E. Blaufuss, S. Blot, C. Bohm, M. Börner, S. Böser, O. Botner, J. Böttcher, E. Bourbeau, J. Bourbeau, F. Bradascio, J. Braun, H.-P. Bretz, S. Bron, J. Brostean-Kaiser, A. Burgman, J. Buscher, R. S. Busse, T. Carver, C. Chen, E. Cheung, D. Chirkin, K. Clark, L. Classen, G. H. Collin, J. M. Conrad, P. Coppin, P. Correa, D. F. Cowen, R. Cross, P. Dave, J. P. A. M. de André, C. De Clercq, J. J. DeLaunay, H. Dembinski, K. Deoskar, S. De Ridder, P. Desiati, K. D. de Vries, G. de Wasseige, M. de With, T. DeYoung, A. Diaz, J. C. Díaz-Vélez, H. Dujmovic, M. Dunkman, E. Dvorak, B. Eberhardt, T. Ehrhardt, P. Eller, P. A. Evenson, S. Fahey, A. R. Fazely, J. Felde, T. Feusels, K. Filimonov, C. Finley, A. Franckowiak, E. Friedman, A. Fritz, T. K. Gaisser, J. Gallagher, E. Ganster, S. Garrappa, L. Gerhardt, K. Ghorbani, T. Glauch, T. Glüsenkamp, A. Goldschmidt, J. G. Gonzalez, D. Grant, Z. Griffith, M. Günder, M. Gündüz, C. Haack, A. Hallgren, L. Halve, F. Halzen, K. Hanson, D. Hebecker, D. Heereman, P. Heix, K. Helbing, R. Hellauer, F. Henningsen, S. Hickford, J. Hignight, G. C. Hill, K. D. Hoffman, R. Hoffmann, T. Hoinka, B. Hokanson-Fasig, K. Hoshina, F. Huang, M. Huber, K. Hultqvist, M. Hünnefeld, R. Hussain, S. In, N. Iovine, A. Ishihara, E. Jacobi, G. S. Japaridze, M. Jeong, K. Jero, B. J. P. Jones, F. Jonske, R. Joppe, W. Kang, A. Kappes, D. Kappesser, T. Karg, M. Karl, A. Karle, U. Katz, M. Kauer, J. L. Kelley, A. Kheirandish, J. Kim, T. Kintscher, J. Kiryluk, T. Kittler, S. R. Klein, R. Koirala, H. Kolanoski, L. Köpke, C. Kopper, S. Kopper, D. J. Koskinen, M. Kowalski, K. Krings, G. Krückl, N. Kulacz, S. Kunwar, N. Kurahashi, A. Kyriacou, M. Labare, J. L. Lanfranchi, M. J. Larson, F. Lauber, J. P. Lazar, K. Leonard, M. Leuermann, Q. R. Liu, E. Lohfink, C. J. Lozano Mariscal, L. Lu, F. Lucarelli, J. Lünemann, W. Luszczak, J. Madsen, G. Maggi, K. B. M. Mahn, Y. Makino, P. Mallik, K. Mallot, S. Mancina, I. C. Mariş, R. Maruyama, K. Mase, R. Maunu, K. Meagher, M. Medici, A. Medina, M. Meier, S. Meighen-Berger, T. Menne, G. Merino, T. Meures, S. Miarecki, J. Micallef, G. Momenté, T. Montaruli, R. W. Moore, R. Morse, M. Moulai, P. Muth, R. Nagai, R. Nahnhauer, P. Nakarmi, U. Naumann, G. Neer, H. Niederhausen, S. C. Nowicki, D. R. Nygren, A. Obertacke Pollmann, A. Olivas, A. O'Murchadha, E. O'Sullivan, T. Palczewski, H. Pandya, D. V. Pankova, N. Park, P. Peiffer, C. Pérez de los Heros, S. Philippen, D. Pieloth, E. Pinat, A. Pizzuto, M. Plum, A. Porcelli, P. B. Price, G. T. Przybylski, C. Raab, A. Raissi, M. Rameez, L. Rauch, K. Rawlins, I. C. Rea, R. Reimann, B. Relethford, G. Renzi, E. Resconi, W. Rhode, M. Richman, S. Robertson, M. Rongen, C. Rott, T. Ruhe, D. Ryckbosch, D. Rysewyk, I. Safa, S. E. Sanchez Herrera, A. Sandrock, J. Sandroos, M. Santander, S. Sarkar, S. Sarkar, K. Satalecka, M. Schaufel, P. Schlunder, T. Schmidt, A. Schneider, J. Schneider, L. Schumacher, S. Sclafani, D. Seckel, S. Seunarine, S. Shefali, M. Silva, R. Snihur, J. Soedingrekso, D. Soldin, M. Song, G. M. Spiczak, C. Spiering, J. Stachurska, M. Stamatikos, T. Stanev, A. Stasik, R. Stein, J. Stettner, A. Steuer, T. Stezelberger, R. G. Stokstad, A. Stößl, N. L. Strotjohann, T. Stürwald,

T. Stuttard, G. W. Sullivan, M. Sutherland, I. Taboada, F. Tenholt, S. Ter-Antonyan, A. Terliuk, S. Tilav, L. Tomankova, C. Tönnis, S. Toscano, D. Tosi, M. Tselengidou, C. F. Tung, A. Turcati, R. Turcotte, C. F. Turley, B. Ty, E. Unger, M. A. Unland Elorrieta, M. Usner, J. Vandenbroucke, W. Van Driessche, D. van Eijk, N. van Eijndhoven, S. Vanheule, J. van Santen, M. Vraeghe, C. Walck, A. Wallace, M. Wallraff, N. Wandkowsky, T. B. Watson, C. Weaver, M. J. Weiss, J. Weldert, C. Wendt, J. Werthebach, S. Westerhoff, B. J. Whelan, N. Whitehorn, K. Wiebe, C. H. Wiebusch, L. Wille, D. R. Williams, L. Wills, M. Wolf, J. Wood, T. R. Wood, K. Woschnagg, G. Wrede, D. L. Xu, X. W. Xu, Y. Xu, J. P. Yanez, G. Yodh, S. Yoshida, T. Yuan, and M. Zöcklein and. Cosmic ray spectrum and composition from PeV to EeV using 3 years of data from IceTop and Ice-Cube. *Physical Review D*, 100(8), October 2019. doi:10.1103/physrevd.100.082002. URL `https://doi.org/10.1103%2Fphysrevd.100.082002`.

M Aguilar, J Alcaraz, J Allaby, B Alpat, G Ambrosi, H Anderhub, L Ao, A Arefiev, L Arruda, P Azzarello, et al. Isotopic composition of light nuclei in cosmic rays: results from ams-01. *The Astrophysical Journal*, 736(2):105, 2011.

M Aguilar, L Ali Cavasonza, G Ambrosi, L Arruda, N Attig, S Aupetit, P Azzarello, A Bachlechner, F Barao, A Barrau, et al. Precision measurement of the boron to carbon flux ratio in cosmic rays from 1.9 gv to 2.6 tv with the alpha magnetic spectrometer on the international space station. *Physical review letters*, 117(23):231102, 2016.

P Allison, JJ Beatty, L Beaufore, Y Chen, S Coutu, E Ellingwood, M Gebhard, N Green, D Hanna, B Kunkler, et al. Cosmic-ray isotope measurements with helix. *Proceedings of Science*, 358, 2019.

Elena Amato. The origin of galactic cosmic rays. *International Journal of Modern Physics D*, 23(07):1430013, 2014. doi:10.1142/S0218271814300134. URL `https://doi.org/10.1142/S0218271814300134`.

W. D. Apel, J. C. Arteaga-Velà zquez, K. Bekk, M. Bertaina, J. Blümer, H. Bozdog, I. M. Brancus, E. Cantoni, A. Chiavassa, F. Cossavella, K. Daumiller, V. de Souza, F. Di Pierro, P. Doll, R. Engel, J. Engler, M. Finger, B. Fuchs, D. Fuhrmann, H. J. Gils, R. Glasstetter, C. Grupen, A. Haungs, D. Heck, J. R. Hörandel, D. Huber, T. Huege, K.-H. Kampert, D. Kang, H. O. Klages, K. Link, P. Łuczak, M. Ludwig, H. J. Mathes, H. J. Mayer, M. Melissas, J. Milke, B. Mitrica, C. Morello, J. Oehlschläger, S. Ostapchenko, N. Palmieri, M. Petcu, T. Pierog, H. Rebel, M. Roth, H. Schieler, S. Schoo, F. G. Schröder, O. Sima, G. Toma, G. C. Trinchero, H. Ulrich, A. Weindl, J. Wochele, M. Wommer, and J. Zabierowski. Ankle-like feature in the energy spectrum of light elements of cosmic rays observed with KASCADE-grande. *Physical Review D*, 87(8), April 2013. doi:10.1103/physrevd.87.081101. URL `https://doi.org/10.1103%2Fphysrevd.87.081101`.

Brian F Aull, Andrew H Loomis, Douglas J Young, Richard M Heinrichs, Bradley J Felton, Peter J Daniels, and Deborah J Landers. Geiger-mode avalanche photodiodes for three-dimensional imaging. *Lincoln laboratory journal*, 13(2):335–349, 2002.

M Ave, PJ Boyle, E Brannon, F Gahbauer, G Hermann, C Höppner, JR Hörandel, M Ichimura, D Müller, A Obermeier, et al. The tracer instrument: A balloon-borne cosmic-ray detector. *Nuclear Instruments and Methods in Physics Research Section A: Accelerators, Spectrometers, Detectors and Associated Equipment*, 654(1):140–156, 2011.

W. Baade and F. Zwicky. Remarks on super-novae and cosmic rays. *Phys. Rev.*, 46:76–77, Jul 1934. doi:10.1103/PhysRev.46.76.2. URL `https://link.aps.org/doi/10.1103/Phy sRev.46.76.2`.

SW Barwick, JJ Beatty, CR Bower, C Chaput, S Coutu, G De Nolfo, D Ellithorpe, D Ficenec, J Knapp, DM Lowder, et al. The high-energy antimatter telescope (heat): An instrument for the study of cosmic-ray positrons. *Nuclear Instruments and Methods in Physics Research Section A: Accelerators, Spectrometers, Detectors and Associated Equipment*, 400 (1):34–52, 1997.

R. Battiston. High precision cosmic ray physics with ams-02 on the international space station. *La Rivista del Nuovo Cimento*, 43(7):319–384, Jul 2020. ISSN 1826-9850. doi:10.1007/s40766-020-00007-2. URL `https://doi.org/10.1007/s40766-020-000 07-2`.

A. R. Bell. The acceleration of cosmic rays in shock fronts – I. *Monthly Notices of the Royal Astronomical Society*, 182(2):147–156, 02 1978. ISSN 0035-8711. doi:10.1093/mnras/182.2.147. URL `https://doi.org/10.1093/mnras/182.2.147`.

E. G. Berezhko. Cosmic rays from active galactic nuclei. *The Astrophysical Journal*, 684(2): L69–L71, aug 2008. doi:10.1086/592233. URL `https://doi.org/10.1086%2F592233`.

Veniamin Berezinsky, Askhat Gazizov, and Svetlana Grigorieva. On astrophysical solution to ultrahigh energy cosmic rays. *Physical Review D*, 74(4), aug 2006. doi:10.1103/physrevd.74.043005. URL `https://doi.org/10.1103%2Fphysrevd.74. 043005`.

D. J. Bird, S. C. Corbato, H. Y. Dai, J. W. Elbert, K. D. Green, M. A. Huang, D. B. Kieda, S. Ko, C. G. Larsen, E. C. Loh, M. Z. Luo, M. H. Salamon, J. D. Smith, P. Sokolsky, P. Sommers, J. K. K. Tang, and S. B. Thomas. Detection of a cosmic ray with measured energy well beyond the expected spectral cutoff due to cosmic microwave radiation. *The Astrophysical Journal*, 441:144, mar 1995. doi:10.1086/175344. URL `https://doi.org/ 10.1086%2F175344`.

DJa Bird, SC Corbato, HY Dai, BR Dawson, JW Elbert, BL Emerson, KD Green, MA Huang, DB Kieda, M Luo, et al. The cosmic-ray energy spectrum observed by the fly's eye. *The Astrophysical Journal*, 424:491–502, 1994.

Roger Blandford, Paul Simeon, and Yajie Yuan. Cosmic ray origins: An introduction. *Nuclear Physics B - Proceedings Supplements*, 256-257:9–22, 2014. ISSN 0920-5632. doi:https://doi.org/10.1016/j.nuclphysbps.2014.10.002. URL `https://www.scienced`

irect.com/science/article/pii/S0920563214001960. Cosmic Ray Origin – Beyond the Standard Models.

Pasquale Blasi. The origin of galactic cosmic rays. *The Astronomy and Astrophysics Review*, 21(1), nov 2013. doi:10.1007/s00159-013-0070-7. URL `https://doi.org/10.1007%2Fs00159-013-0070-7`.

J. Buckley, J. Dwyer, D. Mueller, S. Swordy, and K. K. Tang. A new measurement of the flux of the light cosmic-ray nuclei at high energies. *The Astrophysical Journal*, 429:736–747, July 1994. doi:10.1086/174357.

M Bustamante, G Carrillo Montoya, W de Paula, J A Duarte Chavez, A M Gago, H Hakobyan, P Jez, J A Monroy Montañez, A Ortiz Velasquez, F Padilla Cabal, M Pino Rozas, D J Rodriguez Patarroyo, G L Romeo, U J Saldaña-Salazar, M Velasquez, and M von Steinkirch. High-energy cosmic-ray acceleration, 2010. URL `https://cds.cern.ch/record/1249755`.

Pavel Alekseevič Čerenkov. Visible radiation produced by electrons moving in a medium with velocities exceeding that of light. *Physical Review*, 52(4):378, 1937.

Jin Chang, G Ambrosi, Qi An, R Asfandiyarov, P Azzarello, P Bernardini, B Bertucci, MS Cai, M Caragiulo, DY Chen, et al. The dark matter particle explorer mission. *Astroparticle Physics*, 95:6–24, 2017.

Jérôme Chmeleff, Friedhelm von Blanckenburg, Karsten Kossert, and Dieter Jakob. Determination of the 10be half-life by multicollector icp-ms and liquid scintillation counting. *Nuclear Instruments and Methods in Physics Research Section B: Beam Interactions with Materials and Atoms*, 268(2):192–199, 2010.

OPERATING INSTRUCTION MANUAL FOR THE 4G MAGNET POWER SUPPLY. Cryomagnetics, Incorporated.

Laurent Derome. Cosmic-ray isotopes with the alpha magnetic spectrometer. International Cosmic Ray Conference (Berlin, 2021. URL `https://video.desy.de/video/Cosmic-Ray-Isotopes-with-the-Alpha-Magnetic-Spectrometer/c1e42f1de4cdb29069278dffd612add1`.

J. J. Engelmann, P. Ferrando, A. Soutoul, P. Goret, and E. Juliusson. Charge composition and energy spectra of cosmic-ray nuclei for elements from Be to NI - Results from HEAO-3-C2. *Astronomy and Astrophysics*, 233:96–111, July 1990.

JJ Engelmann, P Ferrando, A Soutoul, Ph Goret, E Juliusson, L Koch-Miramond, N Lund, P Masse, B Peters, N Petrou, et al. Charge composition and energy spectra of cosmic-ray nuclei for elements from be to ni-results from heao-3-c2. *Astronomy and Astrophysics*, 233:96–111, 1990.

AD Erlykin and AW Wolfendale. The role of the galactic halo and the single source in the formation of the cosmic ray anisotropy. *Astroparticle Physics*, 60:86–91, 2015.

123

Ke Fang, Kumiko Kotera, and Angela V. Olinto. NEWLY BORN PULSARS AS SOURCES OF ULTRAHIGH ENERGY COSMIC RAYS. *The Astrophysical Journal*, 750(2):118, apr 2012. doi:10.1088/0004-637x/750/2/118. URL `https://doi.org/10.1088%2F0004-637x%2F750%2F2%2F118`.

ENRICO Fermi. On the origin of the cosmic radiation. *Phys. Rev.*, 75:1169–1174, Apr 1949. doi:10.1103/PhysRev.75.1169. URL `https://link.aps.org/doi/10.1103/PhysRev.75.1169`.

IM Frank and Ig Tamm. Cr ac. *Sci., USSR*, 14:109, 1937.

A. Ghassemi, K. Sato, K. Kobayashi, Y. Ohashi, Y. Enomoto, and Y. Adachi. Mppc technical note. Technical report, Hamamatsu Photonics, March 2017.

Kenneth Greisen. End to the cosmic-ray spectrum? *Phys. Rev. Lett.*, 16:748–750, Apr 1966. doi:10.1103/PhysRevLett.16.748. URL `https://link.aps.org/doi/10.1103/PhysRevLett.16.748`.

Isabelle A. Grenier, John H. Black, and Andrew W. Strong. The nine lives of cosmic rays in galaxies. *Annual Review of Astronomy and Astrophysics*, 53(1):199–246, 2015. doi:10.1146/annurev-astro-082214-122457. URL `https://doi.org/10.1146/annurev-astro-082214-122457`.

Hamamatsu. Mppc ® (multi-pixel photon counter) s13360-2050ve/-3050ve/-6050ve datasheet, 2016. URL `https://www.hamamatsu.com/content/dam/hamamatsu-photonics/sites/documents/99_SALES_LIBRARY/ssd/s13360-2050ve_etc_kapd1053e.pdf`.

MPPC ARRAY: S14498 (resin type) SPECIFICATION SHEET. Hamamatsu Photonics, 2018. Rev. 1st.

T Hams, LM Barbier, M Bremerich, ER Christian, GA de Nolfo, S Geier, H Göbel, SK Gupta, M Hof, W Menn, et al. Measurement of the abundance of radioactive 10be and other light isotopes in cosmic radiation up to 2 gev nucleon–1 with the balloon-borne instrument isomax. *The Astrophysical Journal*, 611(2):892, 2004a.

T Hams, LM Barbier, M Bremerich, ER Christian, GA de Nolfo, S Geier, H Göbel, SK Gupta, M Hof, W Menn, et al. Measurement of the abundance of radioactive 10be and other light isotopes in cosmic radiation up to 2 gev nucleon–1 with the balloon-borne instrument isomax. *The Astrophysical Journal*, 611(2):892, 2004b.

William D. Harkins. The evolution of the elements and the stability of complex atoms. i. a new periodic system which shows a relation between the abundance of the elements and the structure of the nuclei of atoms. *Journal of the American Chemical Society*, 39(5):856–879, 1917. doi:10.1021/ja02250a002. URL `https://doi.org/10.1021/ja02250a002`.

HELIX Collaboration. APRA Proposal, 2021.

Jörg R. Hörandel. Models of the knee in the energy spectrum of cosmic rays. *Astroparticle Physics*, 21(3):241–265, jun 2004. doi:10.1016/j.astropartphys.2004.01.004. URL `https://doi.org/10.1016%2Fj.astropartphys.2004.01.004`.

Hyebin Jeon. Hodoscope. Internal Presentation, 2022.

Karl-Heinz Kampert and Michael Unger. Measurements of the cosmic ray composition with air shower experiments. *Astroparticle Physics*, 35(10):660–678, may 2012. doi:10.1016/j.astropartphys.2012.02.004. URL `https://doi.org/10.1016%2Fj.astropartphys.2012.02.004`.

Patrick Koehn. Optimization of a lhe-cooled superconducting magnet. Bachelor's thesis, University of Michigan, 1995.

Gunther Korschinek, A Bergmaier, T Faestermann, UC Gerstmann, K Knie, G Rugel, Anton Wallner, I Dillmann, G Dollinger, Ch Lierse Von Gostomski, et al. A new value for the half-life of 10be by heavy-ion elastic recoil detection and liquid scintillation counting. *Nuclear Instruments and Methods in Physics Research Section B: Beam Interactions with Materials and Atoms*, 268(2):187–191, 2010.

Kumiko Kotera and Angela V. Olinto. The astrophysics of ultrahigh-energy cosmic rays. *Annual Review of Astronomy and Astrophysics*, 49(1):119–153, sep 2011. doi:10.1146/annurev-astro-081710-102620. URL `https://doi.org/10.1146%2Fannurev-astro-081710-102620`.

Brandon Kunkler. *HELIX RICH Front-End Board User Manual*. Indiana University CEEM, 2022.

Brandon Kunkler and Ian Wisher. Rich electronics. Internal Presentation, 2019.

Antoine Letessier-Selvon and Todor Stanev. Ultrahigh energy cosmic rays. *Rev. Mod. Phys.*, 83:907–942, Sep 2011. doi:10.1103/RevModPhys.83.907. URL `https://link.aps.org/doi/10.1103/RevModPhys.83.907`.

J. A. Lezniak and W. R. Webber. The charge composition and energy spectra of cosmic-ray nuclei from 3000 MeV per nucleon to 50 GeV per nucleon. *The Astrophysical Journal*, 223:676–696, July 1978. doi:10.1086/156301.

John Litt and R Meunier. Cerenkov counter technique in high-energy physics. *Annual Review of Nuclear Science*, 23(1):1–44, 1973.

S. A. Mao, N. M. McClure-Griffiths, B. M. Gaensler, J. C. Brown, C. L. van Eck, M. Haverkorn, P. P. Kronberg, J. M. Stil, A. Shukurov, and A. R. Taylor. New constraints on the galactic halo magnetic field using rotation measures of extragalactic sources toward the outer galaxy. *The Astrophysical Journal*, 755(1):21, jul 2012. doi:10.1088/0004-637X/755/1/21. URL `https://dx.doi.org/10.1088/0004-637X/755/1/21`.

D Maurin, F Melot, and Richard Taillet. A database of charged cosmic rays. *Astronomy & Astrophysics*, 569:A32, 2014.

Rostom Mbarek. *Particle Acceleration, Propagation, and Detection: A Journey from the Kinetic Structure of Plasma Physics to Particle Transport on Cosmic Scales*. PhD thesis, University of Chicago, 2022.

Keith McBride. *Cosmic Ray Instrumentation and Simulations*. PhD thesis, 2021. URL `http://proxy.uchicago.edu/login?url=https://www.proquest.com/dissertations-theses/cosmic-ray-instrumentation-simulations/docview/2607686996/se-2`. Copyright - Database copyright ProQuest LLC; ProQuest does not claim copyright in the individual underlying works; Last updated - 2023-03-08.

Keith McBride. Isotopic composition of cosmic rays with the helix balloon project. TeVPA, 2022. URL `https://indico.cern.ch/event/1082486/contributions/4878734/`.

W Menn, EA Bogomolov, SY Krut'Kov, NN Nikonov, GI Vasilyev, on behalf ofthe PAMELA Collaboration, et al. H, he, li and be isotopes in the pamela-experiment. In *Journal of Physics: Conference Series*, volume 409, page 012030. IOP Publishing, 2013.

W Menn, EA Bogomolov, M Simon, G Vasilyev, O Adriani, GC Barbarino, GA Bazilevskaya, R Bellotti, M Boezio, M Bongi, et al. Lithium and beryllium isotopes with the pamela experiment. *The Astrophysical Journal*, 862(2):141, 2018.

RA Mewaldt, Nathan Eugene Yanasak, ME Wiedenbeck, AJ Davis, WR Binns, ER Christian, AC Cummings, PL Hink, RA Leske, SM Niebur, et al. Radioactive clocks and cosmic-ray transport in the galaxy. In *The Astrophysics of Galactic Cosmic Rays: Proceedings of two ISSI Workshops, 18–22 October 1999 and 15–19 May 2000, Bern, Switzerland*, pages 27–39. Springer, 2001.

Miguel Molero Gonzalez. *Measurement of the Cosmic Ray Anisotropy with AMS-02 on the International Space Station*. PhD thesis, Universidad Autónoma de Madrid, 2021. URL `https://cds.cern.ch/record/2776613`. Presented 14 Jul 2021.

Dietrich Mueller, Simon P Swordy, Peter Meyer, Jacques L'Heureux, and John M Grunsfeld. Energy spectra and composition of primary cosmic rays. *Astrophysical Journal, Part 1 (ISSN 0004-637X), vol. 374, June 10, 1991, p. 356-365.*, 374:356–365, 1991.

Stephan O'Brien. Calibration of Aerogel Tiles for the HELIX-RICH Detector. In *Proceedings of 37th International Cosmic Ray Conference — PoS(ICRC2021)*, volume 395, page 090, 2021. doi:10.22323/1.395.0090.

Giuseppe Oddo. Die molekularstruktur der radioaktiven atome. *Zeitschrift für anorganische Chemie*, 87(1):253–268, 1914. doi:https://doi.org/10.1002/zaac.19140870118. URL `https://onlinelibrary.wiley.com/doi/abs/10.1002/zaac.19140870118`.

C. D. Orth, A. Buffington, G. F. Smoot, and T. S. Mast. Abundances and spectra for cosmic-ray nuclei from lithium to iron for 2 to 150 GeV per nucleon. *The Astrophysical Journal*, 226:1147–1161, December 1978. doi:10.1086/156692.

A Nepomuk Otte. Sipm's a very brief review. In *International Conference on New Photo-detectors*, volume 252, page 001. SISSA Medialab, 2016.

B. Peters. Review of Particle Physics. *Nuovo Cimento*, XXII:800, 1961. doi:10.1093/ptep/ptac097.

Slawomir Piatek. How does temperature affect the performance of an sipm?, Jan 2017. URL https://hub.hamamatsu.com/us/en/technical-notes/mppc-sipms/how-does-tempe rature-affect-the-performance-of-an-SiPM.html.

Claudio Piemonte, Roberto Battiston, Maurizio Boscardin, Gian-Franco Dalla Betta, Alberto Del Guerra, Nicoleta Dinu, Alberto Pozza, and Nicola Zorzi. Characterization of the first prototypes of silicon photomultiplier fabricated at itc-irst. *IEEE Transactions on Nuclear Science*, 54(1):236–244, 2007.

V. S. Ptuskin, S. I. Rogovaya, V. N. Zirakashvili, L. G. Chuvilgin, G. B. Khristiansen, E. G. Klepach, and G. V. Kulikov. Diffusion and drift of very high energy cosmic rays in galactic magnetic fields. *Astronomy and Astrophysics*, 268(2):726–735, February 1993.

GM Raisbeck and F Yiou. Cross section for b 11 (p, 2 p) be 10 at 150 and 600 mev: Implications for cosmic-ray studies. *Physical Review Letters*, 27(13):875, 1971.

O Reimer, W Menn, M Hof, M Simon, AJ Davis, AW Labrador, RA Mewaldt, SM Schindler, LM Barbier, ER Christian, et al. The cosmic-ray 3he/4he ratio from 200 mev per nucleon-1 to 3.7 gev per nucleon- 1. *The Astrophysical Journal*, 496(1):490, 1998.

Eun-Suk Seo. Cream balloon flights and beyond. *39th COSPAR Scientific Assembly*, 39:1753, 2012.

JA Simpson and M Garcia-Munoz. Cosmic-ray lifetime in the galaxy: Experimental results and models. *Space Science Reviews*, 46:205–224, 1988.

Ben Stillwell. Preliminary mechanical design of helix gondola. Technical report, The University Of Chicago, October 2018. Internal Report.

Andrew W Strong, Igor V Moskalenko, and Vladimir S Ptuskin. Cosmic-ray propagation and interactions in the galaxy. *Annu. Rev. Nucl. Part. Sci.*, 57:285–327, 2007.

Simon P Swordy, Dietrich Mueller, Peter Meyer, Jacques L'Heureux, and John M Grunsfeld. Relative abundances of secondary and primary cosmic rays at high energies. *The Astrophysical Journal*, 349:625–633, 1990.

Makoto Tabata, Patrick Allison, James J. Beatty, Stephane Coutu, Mark Gebhard, Noah Green, David Hanna, Brandon Kunkler, Mike Lang, Keith McBride, Samuel I. Mognet, Dietrich Müller, James Musser, Scott Nutter, Nahee Park, Michael Schubnell, Gregory Tarlé, Andrew Tomasch, Gerard Visser, Scott P. Wakely, and Ian Wisher. Developing a silica aerogel radiator for the helix ring-imaging cherenkov system. *Nuclear Instruments and Methods in Physics Research Section A: Accelerators, Spectrometers, Detectors and Associated Equipment*, 952:161879, 2020. ISSN 0168-9002. doi:https://doi.org/10.1016/j.nima.2019.02.006. URL `https://www.sciencedirect.com/science/article/pii/S0168900219301767`. 10th International Workshop on Ring Imaging Cherenkov Detectors (RICH 2018).

Samuel Ting. The alpha magnetic spectrometer on the international space station. *Nuclear Physics B-Proceedings Supplements*, 243:12–24, 2013.

R Trotta, G Jóhannesson, IV Moskalenko, TA Porter, R Ruiz De Austri, and AW Strong. Constraints on cosmic-ray propagation models from a global bayesian analysis. *The Astrophysical Journal*, 729(2):106, 2011.

Michael Unger, Glennys R. Farrar, and Luis A. Anchordoqui. Origin of the ankle in the ultrahigh energy cosmic ray spectrum, and of the extragalactic protons below it. *Physical Review D*, 92(12), dec 2015. doi:10.1103/physrevd.92.123001. URL `https://doi.org/10.1103%2Fphysrevd.92.123001`.

Mario Vietri. The acceleration of ultra–high-energy cosmic rays in gamma-ray bursts. *The Astrophysical Journal*, 453:883, nov 1995. doi:10.1086/176448. URL `https://doi.org/10.1086%2F176448`.

T. T. von Rosenvinge, J. F. Ormes, and W. R. Webber. Measurements of Cosmic-Ray Li, Be and B Nuclei in the Energy Range 100 MeV/NUC to >22 BeV/NUC. *Astrophysics and Space Science*, 3:80–101, January 1969. doi:10.1007/BF00649595.

Eli Waxman. Cosmological gamma-ray bursts and the highest energy cosmic rays. *Phys. Rev. Lett.*, 75:386–389, Jul 1995. doi:10.1103/PhysRevLett.75.386. URL `https://link.aps.org/doi/10.1103/PhysRevLett.75.386`.

W. R. Webber and S. M. Yushak. Comparative Energy Spectra of Z=3-8 Nuclei in the Energy Range 200 Mev/nuc to 3 Gev/nuc. *International Cosmic Ray Conference*, 12:51, 1979.

WR Webber, JC Kish, and DA Schrier. Total charge and mass changing cross sections of relativistic nuclei in hydrogen, helium, and carbon targets. *Physical Review C*, 41(2):520, 1990.

Datasheet Citiroc1A. WEEROC, May 2019. Rev. 1st.

M. E. Wiedenbeck, W. R. Binns, Alan C. Cummings, Andrew M. Davis, G. A. de Nolfo, M. H. Israel, R. A. Leske, Richard A. Mewaldt, Edward C. Stone, and T. T. von Rosenvinge.

An overview of the origin of galactic cosmic rays as inferred from observations of heavy ion composition and spectra. *Space Science Reviews*, 130:415–429, 2007.

ME Wiedenbeck and DE Greiner. A cosmic-ray age based on the abundance of be-10. *Astrophysical Journal, Part 2-Letters to the Editor, vol. 239, Aug. 1, 1980, p. L139-L142.*, 239:L139–L142, 1980.

R. L. Workman and Others. Review of Particle Physics. *PTEP*, 2022:083C01, 2022. doi:10.1093/ptep/ptac097.

Nathan Eugene Yanasak, ME Wiedenbeck, RA Mewaldt, AJ Davis, AC Cummings, JS George, RA Leske, EC Stone, ER Christian, TT Von Rosenvinge, et al. Measurement of the secondary radionuclides 10be, 26al, 36cl, 54mn, and 14c and implications for the galactic cosmic-ray age. *The Astrophysical Journal*, 563(2):768, 2001.

Kenji Yoshida et al. The calet mission of high energy astroparticle physics on the international space station. *39th COSPAR Scientific Assembly*, 2012.

Thomas Ypsilantis and Jacques Séguinot. Theory of ring imaging cherenkov counters. *Nuclear Instruments and Methods in Physics Research Section A: Accelerators, Spectrometers, Detectors and Associated Equipment*, 343(1):30–51, 1994.

Monong Yu. *COSMIC-RAY IRON SPECTRUM MEASURED BY THE ISS-CREAM EXPERIMENT*. PhD thesis, The Pennsylvania State University, 2022.

G. T. Zatsepin and V. A. Kuz'min. Upper Limit of the Spectrum of Cosmic Rays. *Soviet Journal of Experimental and Theoretical Physics Letters*, 4:78, August 1966.